TEMPERATURE-COMPENSATED SILICON-BASED BULK ACOUSTIC RESONATORS

A Dissertation
Presented to
The Academic Faculty

by

Roozbeh Tabrizian

In Partial Fulfillment
of the Requirements for the Degree
of Doctor of Philosophy in the
School of Electrical and Computer Engineering

Georgia Institute of Technology
August 2013

TEMPERATURE-COMPENSATED SILICON-BASED BULK ACOUSTIC RESONATORS

Approved by:

Professor Farrokh Ayazi, Chair, Advisor
School of Electrical and Computer Engineering
Georgia Institute of Technology

Professor Mark G. Allen
School of Electrical and Computer Engineering
Georgia Institute of Technology

Professor John D. Cressler
School of Electrical and Computer Engineering
Georgia Institute of Technology

Professor Laurence J. Jacobs
Schools of Mechanical Engineering
Georgia Institute of Technology

Professor John Papapolymerou
School of Electrical and Computer Engineering
Georgia Institute of Technology

Date Approved: August 6, 2013

To my parents,

Vida Malek-Sanie and Sasan Tabrizian,

and my mentor,

Farrokh Ayazi

ACKNOWLEDGMENTS

I have had the unique privilege of being mentored by an incredible advisor, and in the finest manner. Therefore, I would like to express my foremost gratitude to Professor Farrokh Ayazi, who patiently fostered my passion for science, engineering and education, through his thoughtful, resourceful, supportive, encouraging, responsible, and innovative ways of leadership. His contribution to my growth and success extends far beyond my Ph.D. journey and has resulted in a paradigm shift in my life and its philosophy.

I would also like to thank my dissertation committee members, Professor Mark Allen, Professor John Cressler, Professor Laurence Jacobs and Professor John Papapolymerou for their guidance and support.

I would like to acknowledge Drs. Giorgio Casinovi, Mina Rais-zadeh and Wanling Pan for their invaluable guidance and support during the initial development of required research infrastructures and skills. I would also like to thank my colleagues, Drs. Ashwin Samarao and Logan Sorenson for their intellectual contribution in my research through fascinating scientific discussions which helped me in development and articulation of my qualitative understanding about different physical phenomena. I would also like to acknowledge all of my other colleagues in the Integrated MEMS group for their assistance and friendship. My especial thanks go to Drs. Jenna Fu, Logan Sorenson, Houri Johari and Wang-Kyung Sung, and also Xin Gao, Arashk Norouzpour-Shirazi, Mojtaba Hodjat-Shamami, Yaesuk Jeong and Diego Serrano for being much more than just colleagues.

I would like to thank Georgia Tech IEN cleanroom staff for all of their non-stop efforts and collaborations to keep the equipment up and running all the time. None of this

research could have materialized without their dedicated helps and technical supports over the past few years.

I would like to especially thank my grandmother Homayoontaj Beizaie for being the sun of my life and the unique role model of perseverance and dedication; and also my sister Tahmineh Tabrizian and brother in-law Danial Rahmani, who loved me unconditionally, stood with me shoulder to shoulder during life's ups and downs, thousands of miles away from our hometown.

Finally, I would like to thank my parents, Vida Malek-Sanie and Sasan Tabrizian; while any words absolutely fail to do the justice for this purpose. They have been my whole life; the realization of the finest and most delicate, yet very deep and firm, humanistic attributes in two very different, but complementary, souls. All my current and future contributions and success in academic and social life is nothing else than the realization of their eternal life philosophy, which I hope to be a good ambassador for its distribution and evolution.

TABLE OF CONTENTS

LIST OF TABLES

LIST OF FIGURES

SUMMARY

Microelectromechanical resonators have found widespread applications in timing, sensing and spectral processing. One of the important performance metrics of MEMS resonators is the temperature sensitivity of their frequency. The main objective of this dissertation is the compensation and control of the temperature sensitivity of silicon resonators through engineering of device geometry and structural composition. This has been accomplished through formation of composite platforms or novel geometries based on dispersion characteristics of guided acoustic waves in single crystalline silicon (SCS) microstructures. Furthermore, another objective of this dissertation is to develop efficient longitudinal piezoelectric transduction for in-plane resonance modes of SCS resonators that have lithographically-defined frequencies, to reduce their motional resistance (R_m).

A uniformly distributed matrix of silicon dioxide pillars is embedded inside the silicon substrate to form a homogenous composite silicon-oxide platform (SilOx) with nearly perfect temperature-compensated stiffness moduli. Temperature-stable micro-resonators implemented in SilOx platform operating in any desired in- and out-of-plane resonance modes show full compensation of linear temperature coefficient of frequency (TCF). Overall frequency drifts as small as 80 ppm has been achieved over the industrial temperature range (-40°C to 80°C) showing a 40x improvement compared to uncompensated native silicon resonators. A 27 MHz temperature-compensated MEMS oscillator implemented using SilOx resonator demonstrated sub-ppm instability over the industrial temperature range. Besides this, a new formulation of different resonance modes of SCS resonators based on their constituent acoustic waves is presented in this

dissertation. This enables engineering of the acoustic resonator to provide several resonance modes with mechanical energy trapped in central part of the resonator, thus obviating narrow tethers traditionally used for anchoring the cavity to the substrate. This facilitates simultaneous piezoelectric-transduction of multiple modes with different TCFs through independent electrical ports, which can realize highly accurate self-temperature sensing of the device using a beat frequency (f_b) generated from linear combination of different modes. Piezoelectrically-transduced multi-port silicon resonators implemented using this technique provide highly temperature-sensitive f_b with a large TCF of ~8500 ppm/°C showing 100x improvement compared to other Quartz/MEMS counterparts, suggesting these devices as highly sensitive temperature sensors for environmental sensing and temperature-compensated/oven-controlled crystal oscillator (TCXO/OCXO) applications.

Another part of this dissertation introduces a novel longitudinal piezoelectric transduction technique developed for implementation of low R_m silicon resonators operating in lithographically defined in-plane modes. Aluminum nitride films deposited on the sidewalls of thick silicon microstructures provides efficient electromechanical transduction required to achieve low R_m. 100 MHz SCS bulk acoustic resonators implemented using this transduction technique demonstrates R_m of 33Ω showing a 100x improvement compared to electrostatically transduced counterparts. Low-loss narrow-band filters with tunable bandwidth and frequency have been implemented by electrical coupling of these devices, showing their potential for realization of truly reconfigurable and programmable filter arrays required for software-defined radios.

1 INTRODUCTION

The increasing ubiquity of mobile devices in today's society has increased the demand and potential for miniaturized, integrated sensors. Each generation of smartphone has provided users with enhanced experiences via gaming, navigation, and various location-based services, many of which utilize microelectromechanical systems (MEMS) devices. The versatility of micromachining technology has opened the door to additional functionalities that have yet to be fully explored. For a long time, the demand for mechanical/acoustic frequency references have been limited to and fulfilled by quartz crystal resonators. Superior temperature characteristic of quartz crystal resonators has made these devices preferred choices for implementation of timing and frequency references [1]. Quartz crystal oscillators with different instability levels ranging from few parts per million (ppm) down to few parts per billion (ppb) have been dominating timing market for more than seven decades. These resonators have also been used for implementation of electrically and acoustically coupled band-pass filters where resonators with very low motional resistances (R_m) are desired to achieve low pass-band insertion-losses. However, the applicability of quartz resonators in signal processors has been limited to low frequencies. This was mainly due to the fabrication challenges for implementation of ultra-thin structures in quartz crystal, resulting in frequency limitation of quartz resonators to few hundred megahertz. Also specific packaging requirements of quartz resonators, which were incompatible with CMOS electronic interface, introduced system integration barriers. The demand for high-frequency and high quality factor (Q) electromechanical resonators operating in ultra-high-frequency (UHF) regime resulted in development of high quality piezoelectric films. Therefore, following the first

demonstration of bulk acoustic wave resonators implemented in zinc oxide thin films in 1981 [2], the mainstream of focus for implementation of low-R_m and high-frequency electromechanical resonators focused on development of thin piezoelectric film bulk acoustic resonators (FBAR). FBARs operating in UHF with very low R_m have been realized in thin films of materials with superior piezoelectric properties such as zinc oxide (ZnO), aluminum nitride (AlN) and lead zirconate titanate (PZT). Band-pass filters implemented by electrical and acoustic coupling of FBARs have been increasingly used in signal-processing units of telecommunication systems [3]. Although unique benefits provided by FBARs make them the most popular BAW devices for signal processing, their application remained limited due to their substantial frequency inflexibility resulting in universal frequency of devices implemented in the same batch. The resonance frequency of the FBAR is defined by piezoelectric and electrode films thicknesses and hence is a constant independent of their lateral dimensions. This is undesirable since the fast growth of multiband and multifunction wireless telecommunication systems has resulted in an increasing demand for a single-chip signal processing unit operational for different telecommunication standards, each of which operating at a specific frequency.

On the other hand, the demand for higher levels of integration has resulted in fast-growing interest in silicon-based MEMS resonators. These devices can provide integrated alternatives to off-chip and discrete frequency-selective components and enable a cost-effective integrated platform for timing, sensing and spectral processing applications. The unique advantages of silicon MEMS resonators including their small form factor, potential for on-chip integration with CMOS circuitry, superior acoustic properties of low-cost single crystal silicon substrates, lithographical definition of their resonance frequency and

ease of manufacturing make these devices interesting options to replace quartz crystal and thin-film piezoelectric resonators in timing, sensing and spectral processing applications. However, the main drawbacks of these devices which are their large temperature coefficient of frequency (TCF) and high motional resistances (R_m) have challenged their evolution from research laboratories towards commercial products. Therefore, the mainstream of research on silicon micromechanical resonators have been focused on development of TCF-compensation techniques as well as efficient electromechanical transduction schemes to realize temperature-stable silicon MEMS resonators with low R_m.

This dissertation introduces novel solutions for the main drawbacks and limiting factors of MEMS resonators by focusing separately on both acoustic cavity and integrated transducer. Novel temperature compensated silicon-based composite acoustic platforms has been introduced for implementation of temperature-stable resonators operating in any desired in- and out-of-plane resonance modes. Furthermore, a new formulation of different resonance modes of MEMS resonators will be presented based on their constituent acoustic waves. This facilitates waveguide-level design (in contrary with vibration-level design) of the MEMS acoustic resonators, thus providing very powerful design tool for performance engineering of multiple modes in a single device. Such a formulation contrasts the superiority of piezo-on-silicon platforms for realization of MEMS resonators with high design flexibility and customized performance metrics for different sensing and frequency reference applications. Besides this contribution in the development of high performance acoustic platforms, a novel piezoelectric transduction technology will be introduced to serve as highly efficient integrated transducer for in-plane MEMS resonators, thus overcoming the high motional resistance barrier

embedding the application of silicon-based resonators in versatile signal processing applications.

This dissertation is prepared in 5 chapters. The first chapter briefly introduces the challenges, and then highlights the focus point and contribution of this research in development of high-performance MEMS resonators. The second chapter describes the prior art in temperature compensation and integrated transducers. Chapter three introduces a novel temperature-compensated silicon-based acoustic platform engineered for implementation of temperature-insensitive resonators operating in arbitrary modes and for highly stable frequency reference applications. Chapter four provides a novel explanation of MEMS resonators as acoustic waveguides. The developed formulation has been used to design novel microresonators operating in synthesized resonance modes with low TCF, high Qs and efficient spurious suppression. Chapter five introduces a novel piezoelectric transduction technology, which mixes the advantages of high efficiency longitudinal piezoelectric effect with lithographical definition of in-plane resonance modes for realization of low R_m resonators with versatile frequencies suitable for implementation of reconfigurable filters. Finally chapter six provides a conclusion as well as future potentials for further improvement and application of developed technologies.

2 BACKGROUND

In the majority of MEMS resonator applications, these devices are providing an accurate frequency (or a range of frequencies) reference either as an absolute and independent (timing, frequency reference and spectral applications), or relative and dependent (sensor applications) value. Depending on the specific application, these devices are desired to be either insensitive or have a controlled, and often high, sensitivity to an external, physical and/or chemical, signal. Over the past decade, evolving micromachining technologies have been realized micro- and nano-scale mechanical resonators integrated with efficient electromechanical transducers. Having ultra-small mass and large stiffness owing to their miniaturized size, MEMS resonators can provide ultra-high resonance frequencies with inherently large sensitivities to external ambient variations which impose fluctuations in their mass and/or stiffness. While this makes MEMS resonators potentially desirable devices for environmental sensing, it also raises doubts in their functionality and reliability as an accurate frequency reference unit. Furthermore, although micromachining processes have provided accurate control over the size and material properties of the MEMS resonators to some extent, achieving higher levels of precision and control, required for devices with stable and repeatable, yet competitive, performances imposes technological and costly challenges/barriers on the current manufacturing technologies. Finally, being limited to the fundamental physical and chemical properties of current materials used for implementation of these devices, inherent environmental instabilities in the performance of MEMS resonators remain inevitable regardless of the manufacturing control. As a result of this, a recent wave of research and development on MEMS resonators has been exclusively concentrating on

techniques regarding reduction of the uncertainties and instabilities in MEMS resonator performance through novel designs and development of more complicated composites. Different resonator figures of merit depend on various intrinsic material properties as well as structural geometry of the resonators, and are hence prone to manufacturing uncertainties. The environmental instabilities such as ambient temperature, pressure and humidity directly or indirectly translate into the fluctuations of the fundamental characteristics of MEMS resonators including their elastic moduli, acoustic velocity and energy dissipation; and hence must be carefully controlled (i.e. compensated) with an accuracy defined by required degree of stability and precision of different applications.

2.1 PERFORMANCE CONTROL OF MEMS RESONATORS

After a long nourishment period including development and conceptual proof of performance over the past decade, micromechanical resonators are now evolving from the research labs towards commercial products. The successfulness of such an evolution is mainly depending on demonstration of the capability of maintaining high precision and repeatability across many performance parameters. The major performance metrics of MEMS resonators include their center frequency (f_0), temperature coefficient of frequency (TCF), quality factor (Q), and motional resistance (R_m). Additional aspects such as power handling and linearity may be considered as appropriate to the application.

Depending on the specific application of the MEMS resonator, one or more of its metrics may require accurate compensation [4]. While stringent control and device-to-device repeatability of f_0 is required for nearly all of the applications of MEMS resonators to varying degrees of accuracy, the temperature sensitivity of f_0 (and hence the TCF) is of

major importance for resonators serving as analog signal processors and timing references, as well as environmental sensors, and must be kept within acceptable limits. Furthermore, cost restrictions place limitations on the precision of control over material properties and fabrication processes used to implement these devices, imposing additional uncertainties on their performance.

The large amount of research invested in precise control of MEMS resonator metrics can be categorized into three groups: compensation, tuning, and trimming. Techniques developed under each of these categories may address resonator control at the device or system level and are applied in the design stage and/or post-fabrication. The most preferred techniques can be applied in batch across an entire wafer at once or in one step and are referred to as wafer-level techniques.

2.2 TEMPERTURE COMPENSATION OF MEMS RESONATORS

Both f_0 and Q of the MEMS resonators typically show large temperature sensitivities. While thermal behavior of the Q varies depending on the geometrical design, operation mode and frequency of the resonator and is still under further investigation, the temperature dependency of the majority of mechanical resonators has been well characterized, and can be precisely formulated using high order polynomials. Furthermore, while resonators implemented in different crystal cuts of quartz are showing relatively small temperature dependency, which can be well-characterized by third order polynomials, uncompensated MEMS resonators are showing a large linear temperature dependency. The first order (i.e. linear) temperature sensitivity of f_0 can be defined and related to the temperature sensitivity of the resonator's material properties by its TCF:

$$\mathrm{TCF} = \frac{1}{f_0} \cdot \frac{\partial f_0}{\partial T} \approx \frac{1}{2}(\mathrm{TCE} + \mathrm{CTE}), \qquad (1.1)$$

where TCE, the temperature coefficient of Young's modulus, and CTE, the coefficient of thermal expansion, are intrinsic material properties. Although such a simple expression can be easily derived for MEMS resonators operating in their extensional bulk acoustic or flexural modes, temperature behavior of resonators operating in any arbitrary mode is more complicated and may not be formulated in closed form.

The large TCF of the MEMS resonators is mainly a result of high TCEs of the materials commonly used to implement these devices. For native silicon resonators, the large native TCF of −30 ppm/°C results in a frequency drift as large as 3750 ppm across the industrial temperature range (i.e. uncertainty window) of −40°C to 85°C. Major applications of MEMS resonators, such as temperature compensated crystal oscillators (TCXO) and thermally-stable sensors, often require sub-ppm instability levels, mandating a radical decrease in the TCF of these devices to facilitate full compensation through dynamic mechanisms such as active electronic methods. Therefore, passive TCF compensation techniques are of great interest. Some examples of passive techniques are the compensation of material TCE through engineering of doping profile; engineering device geometry to operate in resonance modes defined by elastic coefficients with lower temperature sensitivity; addition of a compensating material with a TCE of opposite sign to form a composite structure with reduced TCF. Figure 2.1 shows the SEM image of a TCF-compensated concave silicon bulk acoustic resonator (CBAR) in comparison with a rectangular geometry silicon bulk acoustic resonator (SiBAR).

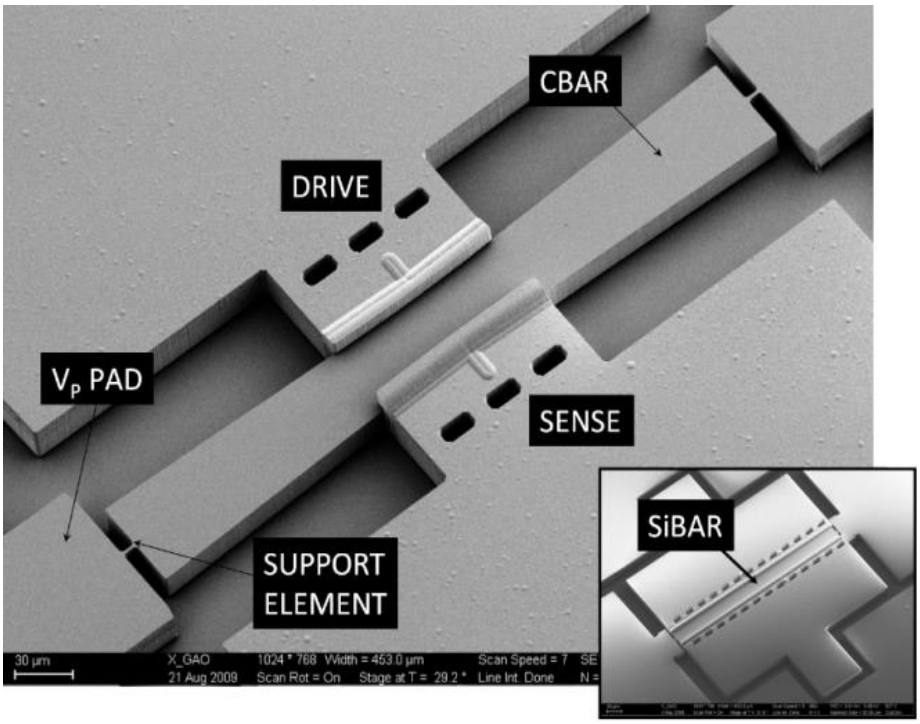

Figure 2.1: Geometry-engineered TCF-compensated concave SiBAR (CBAR). Device shows a TCF of –6 ppm/°C at 105MHz with a Q of 100,000 [5].

The concave resonator geometry has resulted in the excitation of a resonance mode with large energy concentration in shear acoustic fields and thus considerable reduction in the *TCF*. Furthermore, such geometry has resulted in significant improvement in device *Q* due to efficient compensation of energy leakage from the resonator towards surrounding substrate [5]. This device demonstrates the geometry engineering approach to compensation.

Another group of *TCF* compensation techniques which can be used for resonators implemented in semiconductors are based on selective introduction of dopants into the substrate to reduce its large *TCE* by modifying the electronic energy levels. These techniques can be broadly termed doping profile engineering. Different works falling under this category include utilization of heavily P-doped [6], [7] and N-doped silicon substrates [8], [9], thermo-migration of aluminum atoms into the silicon substrate [10],

and carrier depletion of the device using multiple PN junctions [11]. It has been recently demonstrated that the efficiency of doping-profile engineering technique is considerably depending on the resonance mode as well as device relative crystallographic orientation.

Several designs have been proposed to employ this dependency to implement devices with maximum compensation of linear temperature dependency; thus resulting in a second order parabolic temperature characteristic. Such a characteristic, beside showing considerable improvement in overall frequency drift in desired temperature range, possess a turn-over point with zero local TCF. Such a turn-over point, if designed to be higher than device temperature range of operation, can facilitate implementation of an oven-controlled crystal oscillator (OCXO) operating at the turn-over point; hence reducing the sensitivity of the oscillator frequency to ambient thermal fluctuations. Figure 2.2 shows the temperature characteristic of a silicon bulk acoustic resonator with thin film aluminum nitride (AlN) transduction, oriented in <100> crystal direction of a heavily doped silicon substrate, to achieve the maximum compensation of linear TCF.

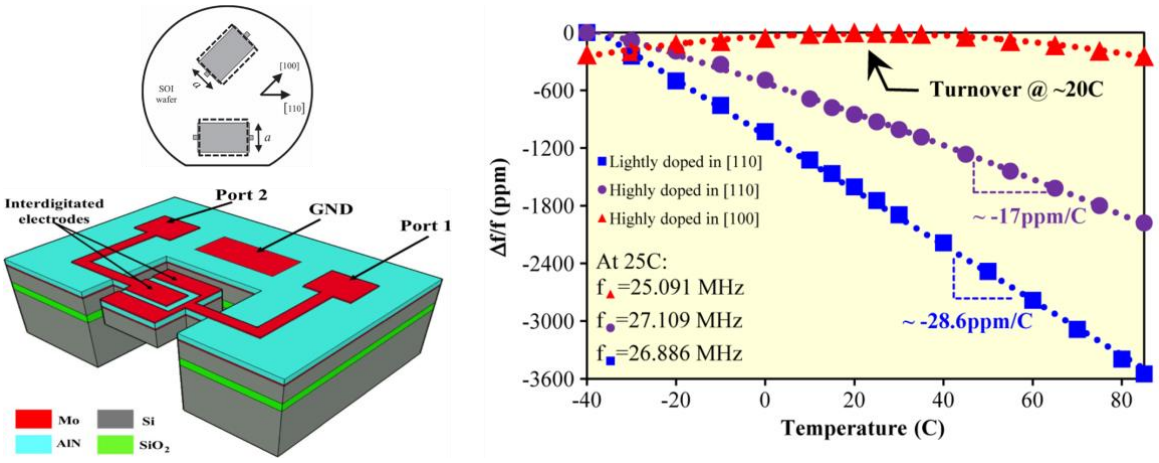

Figure 2.2: Temperature characteristics of extensional mode resonators aligned in different crystallographic direction of silicon and for different doping concentration [9].

Although doping-profile engineering has demonstrated considerable advancement in temperature desensitization of resonance frequency, since the accurate control of impurity concentration across the wafer can be very costly in manufacturing process, the repeatability of the temperature characteristic in these devices is challenging.

More traditional TCF compensation techniques rely on addition of a compensating material. In these approaches, the large negative TCE of native silicon is compensated by addition of a material with positive TCE (usually silicon dioxide). Adding the correct amount of silicon dioxide to the silicon resonator forms a composite Si/SiO_2 structure with temperature-compensated TCE. Figure 2.3 illustrates this concept schematically.

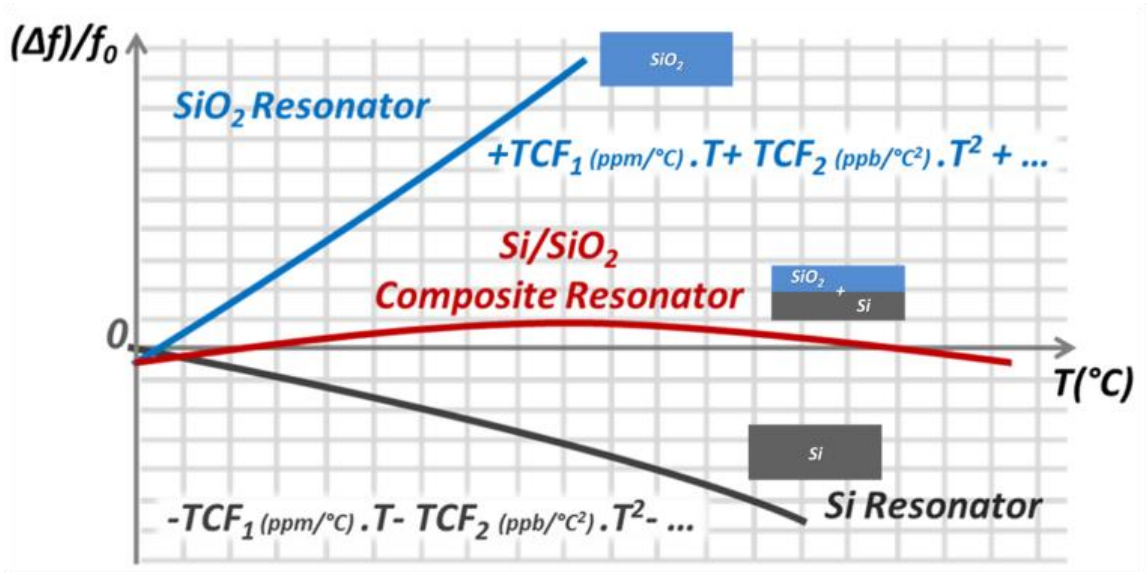

Figure 2.3: Schematic representation of compensating a silicon resonator with silicon dioxide. When first order compensation has been achieved, a residual quadratic characteristic remains due to higher order residuals.

The compensating silicon dioxide can be added in layers parallel to the resonator stack and is called surface SiO_2 compensation [12], [13]. In this technique, the compensating SiO_2 provides a parallel stiffness loading on the surface of silicon which is inherently in-efficient considering the smaller stiffness of SiO_2 compared to Si. Although

attempts in increasing the interface area between Si and SiO_2 has resulted in higher efficiencies [14], thick layers of SiO_2, comparable to that of silicon, is required to provide full compensate of linear TCF. Hence this technique is mostly applicable to thin substrates and low frequency flexural or extensional mode resonators, but more difficult to use for full TCF compensation of bulk acoustic wave (BAW) or high frequency flexural devices with thick substrates that offer high Q and superior power handling and linearity [6].

Alternatively, efficient TCF compensation of thick and high frequency silicon resonators has been achieved by embedding compensating SiO_2 in the bulk (Figure 2.4) of the resonant structure (Bulk SiO_2 compensation). This has been first demonstrated by the author for temperature compensation of 27 MHz BAW resonators with piezoelectric transduction. In this technique, which will be explained in detail in chapter 2, less amount of SiO_2 is required since it places in series with acoustic wave propagation direction and provides substantially more effective stiffness load on the silicon body. In these techniques, bulk SiO_2 is embedded inside the resonator body by carefully filling trenches with thermal of LPCVD SiO_2 to provide a solid void-less platform.

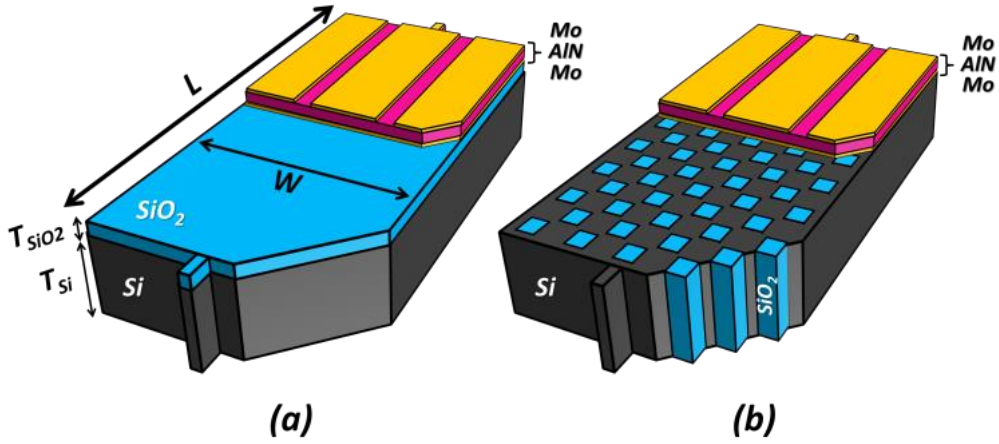

Figure 2.4: Silicon resonators with piezoelectric transduction: (a) with surface oxide compensation and (b) with bulk oxide compensation.

Although first demonstration of bulk SiO_2 compensation provided a general solution for full temperature compensation of any arbitrary mode in silicon resonators, this technique has been also used for selective compensation for specific resonance modes [15]. Figure 2.5 shows the selective bulk compensation, where regions with high acoustic energy concentration of an in-plane high frequency flexural resonator has been used to aggrandize the stiffness loading of silicon dioxide on the resonator and hence require least amount of compensating material to achieve full linear TCF cancelation.

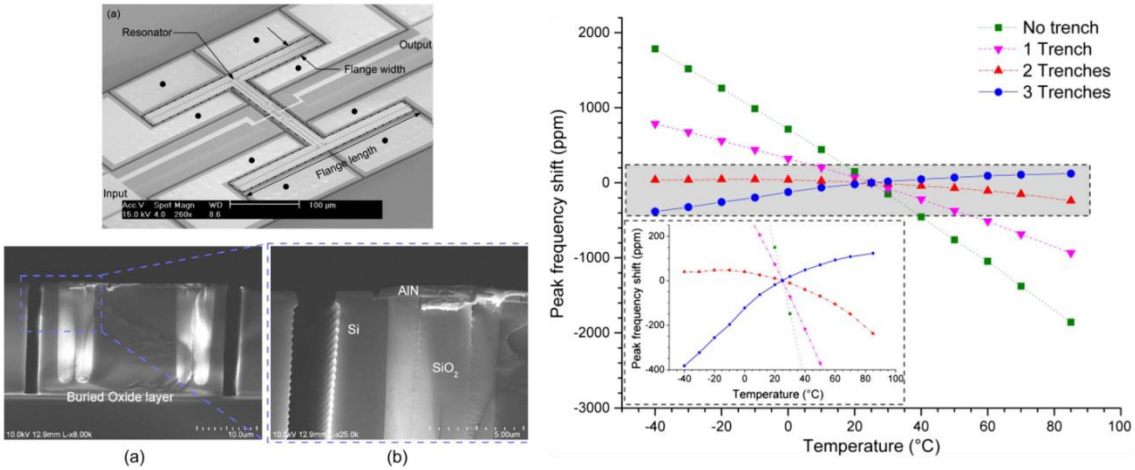

Figure 2.5: Flexural resonators with bulk SiO_2 temperature compensation and their temperature characteristic of resonance frequency [15].

Although bulk SiO_2 compensation facilitates full TCF compensation with the least amount of compensating material, since the relative volumetric ratio of SiO_2 to Si is defined lithographically by the trenches etched in the body of the resonator, the repeatability of temperature characteristic of these devices is defined by fabrication process uncertainties.

2.3 TUNING METHODS IN MEMS RESONATORS

Although TCF and process compensation techniques considerably reduce the amount of temperature and process-induced frequency drifts and uncertainties, full compensation of residual f_0 deviations as well as drifts caused by aging effects requires dynamic adjustment which is provided by tuning mechanisms. Frequency tuning can be addressed in both device and system levels.

2.3.1 DEVICE-LEVEL TUNING

These tuning mechanisms provide electronic f_0 tuning for individual resonators through electromechanical transducers and by changing the effective equivalent stiffness of the micromechanical resonator.

Electrostatic tuning has traditionally been the most commonly employed device-level tuning mechanism. In this technique, an electrical spring whose stiffness is tunable via DC voltage is added in series with the mechanical stiffness of the resonator and provides continuous f_0 tuning with a quadratic characteristic. While small stiffness of the electrical spring, resulting from low-efficiency electrostatic transduction, makes this tuning technique more appropriate for low frequency flexural mode resonators [16], large tuning ranges have also been reported for high frequency bulk acoustic devices with efficient sub-μm capacitive gaps [17]. Figure 2.6 shows a high frequency (20 MHz) I-shaped bulk acoustic resonator (IBAR) designed for maximum tunability. Temperature-compensated oscillators have been built using this tuning mechanism in IBARs [18].

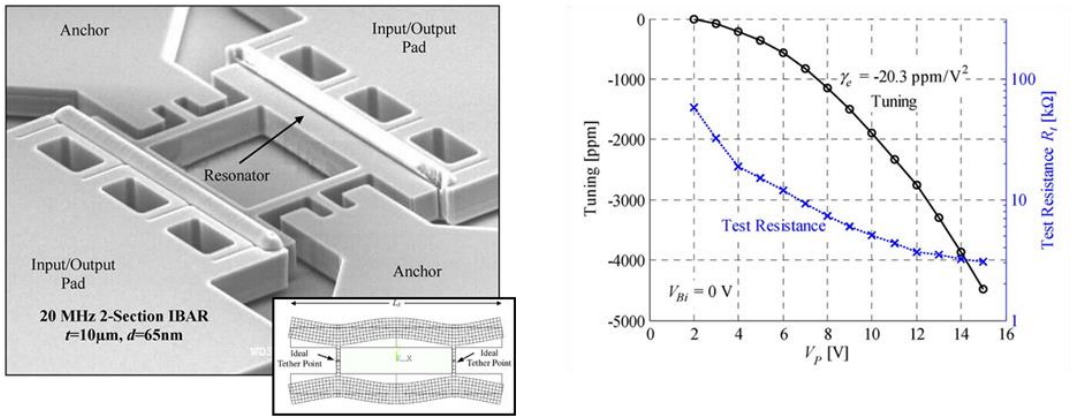

Figure 2.6: A 20 MHz IBAR with large frequency tuning range.

Although application of electrostatic tuning is convenient in capacitive resonators, since the motional resistance of these devices is highly sensitive to their V_P, electronic tuning of f_0 results in fluctuations of the resonator's IL, which is usually not desirable. This problem has been solved by separation of the capacitive tuning electrodes from the AC electromechanical transducer [19]. Figure 2.7 shows a 32 kHz flexural resonator with AlN piezoelectric transduction and electrostatic tuning. Having a large tuning pad which jointly serves as a frequency-loading mass enables large f_0 tuning capable of covering the temperature-induced frequency drift across the entire oscillator industrial temperature range.

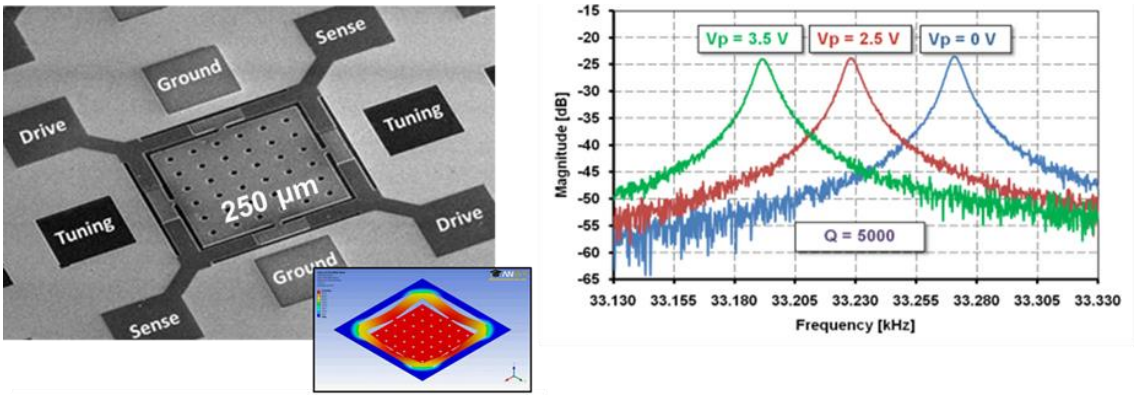

Figure 2.7: A 32 kHz flexural-mode resonator with AlN piezoelectric transduction and electrostatic tuning.

Another electronic device-level tuning mechanism which is capable of providing large tuning ranges is based on ovenization of the microresonator via Joule heating. In this technique, a tunable DC current passing through a heater element results in increased resonator temperature and hence controllable frequency changes due to the large TCF of uncompensated resonators [20], [21], [22]. The highest efficiency and agility of thermal tuning has been achieved by self-ovenization of silicon resonators. In this technique, the heating current passes through the device and the resonator serves as the micro-oven simultaneously [21], [22].

In addition to electrostatic and thermal tuning techniques, a tuning mechanism which is applicable to piezoelectrically-transduced MEMS resonator is the piezoelectric stiffening effect. In this technique (figure 2.8) the stiffness of the piezoelectric film is controlled by tuning its electric termination at the tuning port [23], [24].

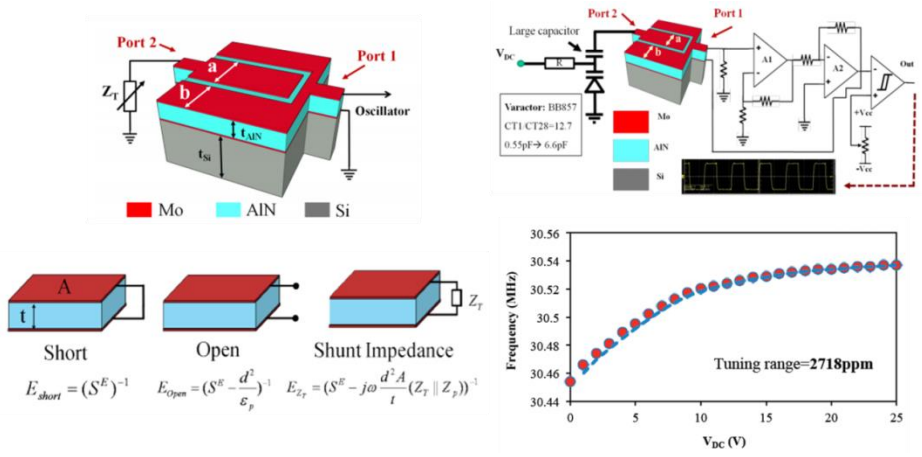

Figure 2.8: Piezoelectric tuning concept and tunable oscillator implemented based on TPOS tunable device [23].

2.3.2 SYSTEM-LEVEL TUNING

System-level tuning and frequency control mechanisms are applied to the systems where MEMS resonator serves as the frequency reference. These techniques include the

use of phase-locked loops [25] or addition of tunable electrical impedances and phase-shifters in series and/or in parallel with the resonator [26], [27]. Systems employing these techniques can tune out the residual frequency drifts and uncertainties of TCF and process compensated resonators, to form highly-stable frequency references. Figure 8 shows the schematic design of a 27 MHz oscillator implemented from the TCF-compensated SilOx resonator of figure 2.9 in addition to tunable capacitors and phase-shifters embedded in series with the resonator in the oscillator loop.

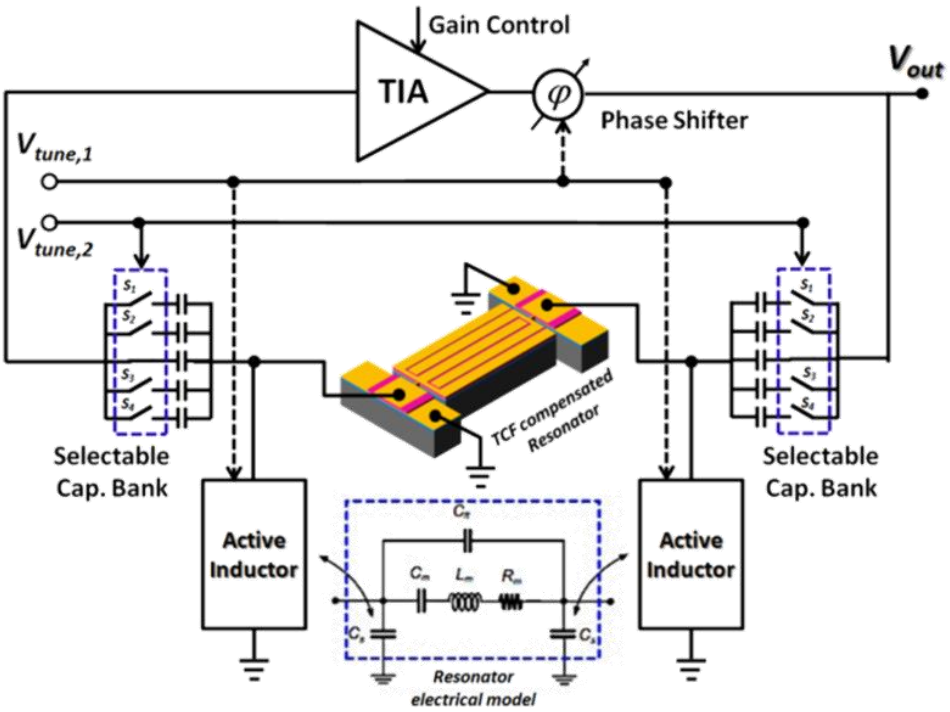

Figure 2.9: System diagram of a 27 MHz temperature-stable MEMS oscillator with sub-ppm instability using SilOx resonator and system-level tuning [26].

2.4 ELECTROMECHANICAL TRANSDUCTION IN MEMS RESONATORS

Probably the most important milestones of MEMS resonator technology establishment are the invention of Bosch-DRIE process for etching deep narrow trenches in silicon and also realization of high quality piezoelectric thin films. Considering any

electromechanical resonator as an acoustic platform with integrated transducer, development of efficient electromechanical transduction schemes have made a major portion of MEMS resonator technology evolution.

Several performance metrics of a resonator may be directly or indirectly affected by the transduction mechanism used for drive/sense the acoustic resonance mode. Among them, R_m is mainly defined by electromechanical transduction efficiency provided by transducer. Also Q of the resonator may be indirectly, yet considerably, affected by the employed transducer.

2.4.1 ELECTROSTATIC TRANSDUCTION

This transduction technique is based on implementation of narrow trenches electrically isolating acoustic cavity from surrounding pads. The electrical signal applied across this gap, which may be filled by a dielectric material, provides a normal force on the sidewall of the cavity resulting in excitation of the resonance mode. A polarization DC voltage is also required to be applied to device to provide a mechanical force directly proportional to the applied electric signal. The main advantages of this transduction is physical isolation from acoustic cavity (in the case of air gap), which eliminates any destructive effect on the Q of resonator. Besides this, in-plane forces provided by this technique facilitate excitation of in-plane resonance modes with lithographically defined frequencies. The efficiency of this transduction technique is highly depending on the narrow gap width as well as DC polarization voltage (Vp). Figure 2.10 shows a silicon bulk acoustic resonator electrostatically transduced through air gaps. Although sub-50 nm gaps have been realized thanks to innovative processing techniques [28], the motional resistances of the devices using this transduction are usually high, making them

undesirable for implementation of low-loss filters. Furthermore, large polarization voltages required for operation of these devices are challenging to be generated on-chip. Finally, although the frequency of capacitive resonators can be tuned by changing their polarization voltage, undesired fluctuations of Vp may result in random frequency drifts which is undesirable in highly stable frequency reference applications.

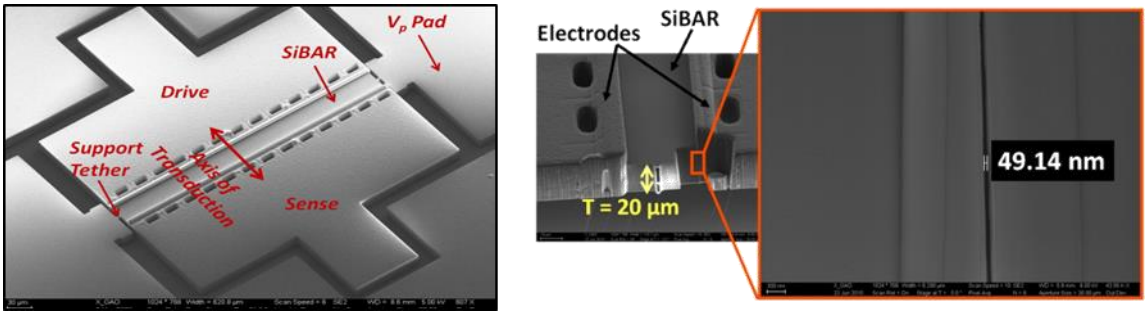

Figure 2.10: Silicon bulk acoustic resonator with sub-50 nm capacitive gaps provided for R_m improvement.

2.4.2 PIEZOELECTRIC TRANSDUCTION

Piezoelectric transduction provides a higher efficiency compared to capacitive transducers. This substantially linear transduction mechanism (in contrary with nonlinear electrostatic counterpart) does not need any polarization voltage for operation and its efficiency is independent from resonance frequency. Thin piezoelectric films can be used as transducer of the acoustic cavity implemented from acoustically passive material, or can simultaneously serve as the structural body of the resonator. Piezoelectric films can provide two different transduction schemes. Application of an electric field across the film can result in two orthogonal forces: 1) in the same direction of the electric field (longitudinal effect) and 2) in in-plane radial directions (transverse effect). Due to larger longitudinal piezoelectric coefficient of thin films, higher electromechanical transduction efficiency can be achieved using longitudinal piezoelectric effect. Low R_m FBARs has

been implemented [29] and electrically coupled [30] to form low-loss filters in UHF regime (figure 2.11). However, since the mechanical force generated in this scheme is aligned with applied electric fields, only out-of-plane modes can be excited when piezoelectric film deposited on the top surface of substrate. Such devices implemented in piezo-on-substrate platforms lacks from frequency versatility, which is the most promising feature of lithographically defined MEMS structures. This is due to inflexibility of the frequency of out-of-plane modes, which are tightly tied to the thickness of the materials used in resonator stack and is constant across the wafer.

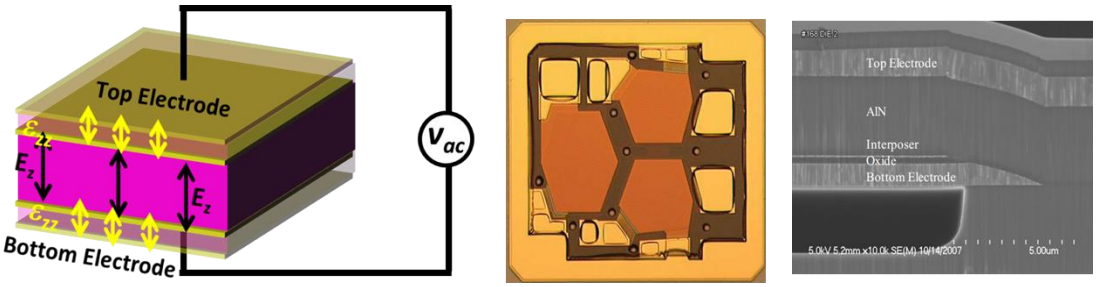

Figure 2.11: (a) Longitudinal piezoelectric transduction scheme. (b) Electrically coupled FBAR filter. (c) The cross-section of the FBAR showing piezoelectric film sandwiched between metallic electrodes.

Transverse piezoelectric transduction, on the other hand, can provide in-plane forces required for lithographically-defined resonance modes. Furthermore, since the electromechanical force can be applied in selective regions with metallic electrodes, higher order tones or even linearly independent resonance modes can be excited in the resonator while spurious suppression of undesired modes can be easily achieved by proper patterning of sense electrodes (figure 2.12). This, in addition to unique temperature and acoustic features which can be offered by acoustic cavities implemented in semiconductor materials, provides a powerful platform for versatile acoustic engineering of the resonator. However, although thin-film piezo-on-substrate platforms using transverse piezoelectric effect are promising for sensing and frequency reference

applications, they are not able to provide very low R_m required for implementation of low-loss filters; thus preventing from realization of lithographically-defined low-loss electrically- or acoustically-coupled filters.

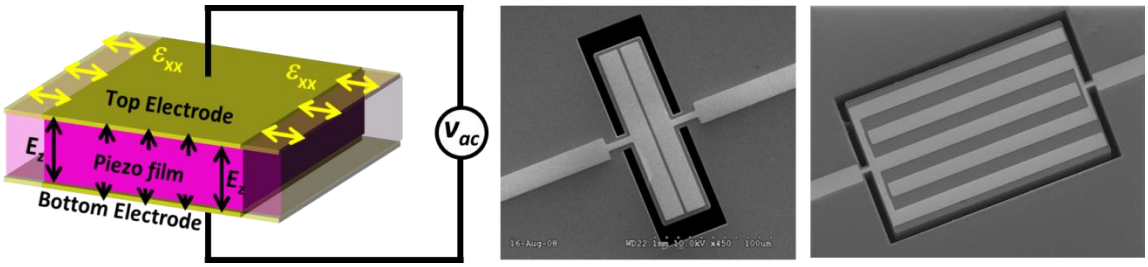

Figure 2.12: (a) Transverse piezoelectric transduction scheme. (b) First-order and(c) fifth-order silicon bulk acoustic resonators with transverse AlN piezoelectric signal transduction.

3 TEMPERATURE-STABLE SILICON-OXIDE (SILOX) MICROMECHANICAL RESONATORS

This chapter presents a passive temperature compensation technique that can provide full cancellation of the linear temperature coefficient of frequency (TCF_1) in silicon resonators. A uniformly distributed matrix of silicon dioxide pillars is embedded inside the silicon substrate to form a homogenous composite silicon-oxide platform (SilOx) with nearly perfect temperature-compensated stiffness moduli. This composite platform enables the implementation of temperature-stable micro-resonators operating in any desired in- and out-of-plane resonance modes. Full compensation of TCF_1 has been achieved for extensional and shear modes of SilOx resonators resulting in a quadratic temperature characteristic with an overall frequency drift as low as 83 ppm over the industrial temperature range (-40°C to 80°C). Beside a 40 times reduction in temperature-induced frequency drift in this range, SilOx resonators exhibit improved temperature stability of *Q* compared to their single crystal silicon counterparts.

3.1 INTRODUCTION

Silicon resonators have become of increasing interest for timing and frequency reference applications [4]. The ability to offer low impedances at high frequencies and the high intrinsic quality factor (Q) of silicon [31] make such resonators very attractive for low-phase-noise high frequency reference oscillators. However, the main drawback of silicon resonators is their relatively high temperature coefficient of frequency (TCF), which results in a large temperature-induced frequency drift. Various active and passive temperature compensation techniques [32] have been proposed for MEMS resonators. While active compensation techniques provide real-time frequency control with high

precision, they increase power consumption and introduce undesired noise and complexity into the system. On the other hand, full or partial compensation of the large linear TCF of silicon resonators by means of conventional passive techniques has been only achieved in thin flexural and extensional resonators and specific bulk acoustic wave (BAW) resonance modes in certain crystallographic orientations.

In this section we present a novel passive temperature compensation technique that can realize silicon-based composite platforms with temperature-compensated acoustic properties, for implementation of temperature-stable devices oriented in arbitrary crystallographic directions and operating in any in- and out-of-plane resonance modes. Using this technique, full compensation of the large linear TCF has been achieved simultaneously for several resonance modes of micro-resonators without degradation of other important performance metrics such as Q and insertion loss (IL).

3.2 SIO_2 TEMPERATURE COMPENSATION IN RESONATORS

The temperature sensitivity of the resonance frequency (f_{res}) of a resonator can be defined using its temperature coefficients:

$$f_{res}(T) = f_0 \cdot \sum_{n=0}^{\infty} TCF_n \cdot (T - T_0)^n, \qquad (3.1)$$

where f_0 is the resonance frequency at an arbitrary operating temperature T_0, and TCF_n is the n^{th} order temperature coefficient of frequency:

$$TCF_n = \frac{1}{n! f_0} \cdot \frac{\partial^n f_T}{\partial T^n}\Big|_{T=T_0}. \qquad (3.2)$$

The finite TCF_i of the resonance modes excited in a micromechanical resonator is a result of temperature sensitivity of the resonator dimensions as well as of several material properties such as its elastic moduli (λ), Poisson's ratio (υ) and mass density (ρ).

For the case of in-plane bulk acoustic resonance modes of an infinitely long ($L \to \infty$) and thin/thick ($H \to 0$ or ∞) acoustic waveguide of width W, the resonance frequency of the n^{th} width-extensional (WE) and width-shear (WS) bulk modes are given by:

$$f_{res} = \frac{n}{2W}\sqrt{\lambda/\rho}, \qquad (3.3)$$

where λ is the effective elastic modulus — either Young's (E) or shear modulus (G) — of the resonator material in the wave propagation direction. It follows from (3.3) that for the bulk acoustic modes, TCF_i is related to the intrinsic material properties by:

$$TCF_i = \frac{1}{2}(TC\lambda_i + CTE_i), \qquad (3.4)$$

where $TC\boldsymbol{\lambda}_i \left(= \frac{1}{i!\lambda_0} \cdot \frac{\partial^i \lambda_T}{\partial T^i}|_{T=T_0}\right)$ is the temperature coefficient of the elastic modulus and $CTE_i \left(= \frac{1}{i!W_0} \cdot \frac{\partial^i W_T}{\partial T^i}|_{T=T_0}\right)$ is the coefficient of thermal expansion of the material.

Unlike quartz crystal resonators [33], the temperature-induced frequency drift of MEMS resonators is mainly determined by their linear temperature coefficient ($TCF_1 = (TC\lambda_1 + CTE_1)/2$ in the case of bulk modes) over the temperature range of interest. In native single crystal silicon (SCS), $TC\boldsymbol{\lambda}_1$ ranges between –47 and –63 ppm/°C depending on the resonance particle polarization and mode of operation (shear or extensional). This variation is a result of dissimilar temperature characteristics of different stiffness coefficients of silicon. Considering the relatively small CTE_1 of silicon (approximately 2.6 ppm/°C), the large value of $TC\boldsymbol{\lambda}_1$ is mainly responsible for the TCF_1 of silicon bulk acoustic resonators (SiBAR), which typically ranges between –22 and –30 ppm/°C.

Although the TCF of bulk acoustic modes in infinitely long and thin waveguides can be related to the intrinsic material properties through (3.4), a similarly simple relationship does not exist for all the resonance modes excited in micromechanical structures with finite dimensions. This is due to the fact that the resonance frequency of these modes cannot be related to the material properties and resonators dimensions through a simple closed-form expression; and unlike bulk modes, all different independent elastic constants (E, G and υ) may contribute effectively in defining the resonance frequency. Hence, a passive compensation technique should provide full temperature compensation for all independent elastic constants in order to be effective for all resonance modes. In micromechanical resonators implemented in native SCS, the large negative $TC\boldsymbol{\lambda}_1$ can be compensated by the addition of a material with positive $TC\boldsymbol{\lambda}_1$ such as silicon dioxide (SiO_2), thus forming a composite Si/SiO2 structure. The degree of temperature compensation of $TC\boldsymbol{\lambda}_1$ depends both on the amount and the configuration of SiO_2 distribution relative to Si in the composite structure.

3.2.1 SURFACE OXIDE COMPENSATION

The compensating SiO_2 can be added in the form of layers covering the surfaces of a silicon resonator: we refer to this method as surface oxide compensation. In this case the resonant structure is composed of several layers of different materials stacked in certain directions. They include one or more compensation layers and possibly a piezoelectric electromechanical transducer sandwiched between metallic electrodes (Aluminum Nitride (AlN) and Molybdenum (Mo) layers in Figure 3.1(a).

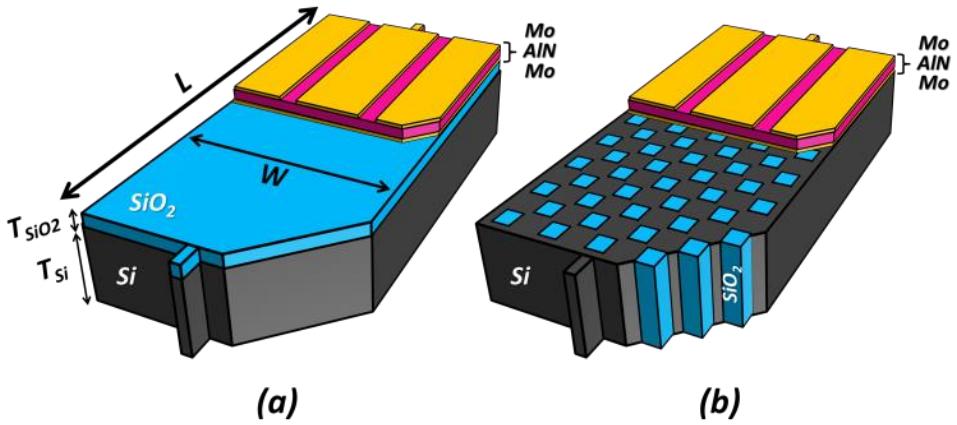

Figure 3.1: Silicon resonators with piezoelectric transduction: (a) with surface oxide compensation and (b) with bulk oxide compensation.

The overall TCF_1 of such a composite resonator with surface SiO_2 compensation operating in WE or WS bulk acoustic modes can be estimated as follows:

$$TCF_1 \approx \frac{1}{2}\sum_i \frac{T_i}{T_{res}}(TC\lambda_{1,i} + CTE_{1,i}), \qquad (3.5)$$

where $TC\boldsymbol{\lambda}_{1,i}$, $CTE_{1,i}$ and T_i are respectively the temperature coefficient of the elastic modulus, the linear coefficient of thermal expansion and the thickness of the i^{th} layer, and T_{res} is the overall thickness of the stack. Since the SiO_2 layer is placed in parallel with a silicon layer with a much larger elastic modulus, it follows from (3.5) that surface SiO_2 compensation becomes less efficient as the relative thickness of silicon in the stack increases. Furthermore, since this technique provides only one degree of freedom, i.e. the thickness of the SiO_2 layer, the compensation effect on various elastic constants and hence different resonance modes differs considerably.

3.2.2 BULK OXIDE COMPENSATION

In order to increase the relative contribution of SiO_2 in $TC\boldsymbol{\lambda}_1$ of a composite Si/SiO2 structure, the compensating SiO_2 can be embedded in the bulk of the silicon resonant structure: this is referred to as bulk oxide compensation. In this technique, a

matrix of SiO_2 pillars with a desirable pattern is distributed inside the body of a silicon resonator to form a silicon-oxide composite resonator. In this manner, since the additional SiO_2 can be embedded in series with silicon in the path of in-plane propagating acoustic waves, full compensation of the large TCF_1 for different resonance modes can be achieved by adding a minimum amount of SiO_2. This makes bulk compensation fully compatible with the limitations of standard micro-fabrication processes.

Furthermore, this technique is scalable with resonator thickness, and can be applied even to thick resonant structures. Last but not least, the in-plane lateral dimensions of the SiO_2 pillars as well as the pattern and density of their distribution in the matrix can be exploited as additional degrees of freedom to simultaneously compensate multiple resonance modes through the compensation of corresponding elastic constants in desired orientation.

3.2.3 COMPENSATION EFFECT OF SiO_2 IN PARALLEL AND SERIES DISTRIBUTION

Considering the equivalent Young's modulus of a Si/SiO2 composite resonator (E_{comp}) as a function of that of Si and SiO_2 (i.e. $E_{comp} = f(E_{Si}, E_{SiO2})$), the linear temperature dependence of E_{comp} can be described as a function of TCE_{Si} and TCE_{SiO2} using the chain rule:

$$\frac{\partial E_{comp}}{\partial T} = \frac{\partial E_{Si}}{\partial T} \cdot \frac{\partial E_{comp}}{\partial E_{Si}} + \frac{\partial E_{SiO2}}{\partial T} \cdot \frac{\partial E_{comp}}{\partial E_{SiO2}}$$

$$= E_{Si} \cdot TCE_{Si} \cdot \frac{\partial E_{comp}}{\partial E_{Si}} + E_{SiO2} \cdot TCE_{SiO2} \cdot \frac{\partial E_{comp}}{\partial E_{SiO2}}$$

$$\approx E_{Si} \cdot TCE_{Si} \cdot \frac{\partial E_{comp}}{\partial E_{Si}} \cdot \left(1 - \frac{\frac{\partial E_{comp}}{\partial E_{SiO2}}}{\frac{\partial E_{comp}}{\partial E_{Si}}} \right) \qquad (3.6)$$

Interestingly, for <110> crystalline direction of silicon, $E_{Si}.TCE_{Si}$ and $E_{SiO2}.TCE_{SiO2}$ are very similar in magnitude but are opposite in sign; hence the approximation in (3.6) is valid. So, in order to achieve full compensation (i.e. $\frac{\partial E_{comp}}{\partial T} = 0$), $\frac{\frac{\partial E_{comp}}{\partial E_{SiO2}}}{\frac{\partial E_{comp}}{\partial E_{Si}}}$ ratio should be as close as possible to 1. $\frac{\frac{\partial E_{comp}}{\partial E_{SiO2}}}{\frac{\partial E_{comp}}{\partial E_{Si}}}$ ratio depends on both the configuration as well as distribution density of additional SiO_2 to the Si platform. Considering two extreme cases of parallel and series homogenous distribution of SiO_2 in Si (Figure 3.2), E_{comp} can be described based on mass-spring equivalent model and as formulated in (3.8).

Figure 3.2 shows the mass-spring equivalents for a unit cell with ideally homogenous/uniform distribution of SiO_2 in Si platform in (a) series and (b) parallel configuration with respect to longitudinal wave propagation direction.

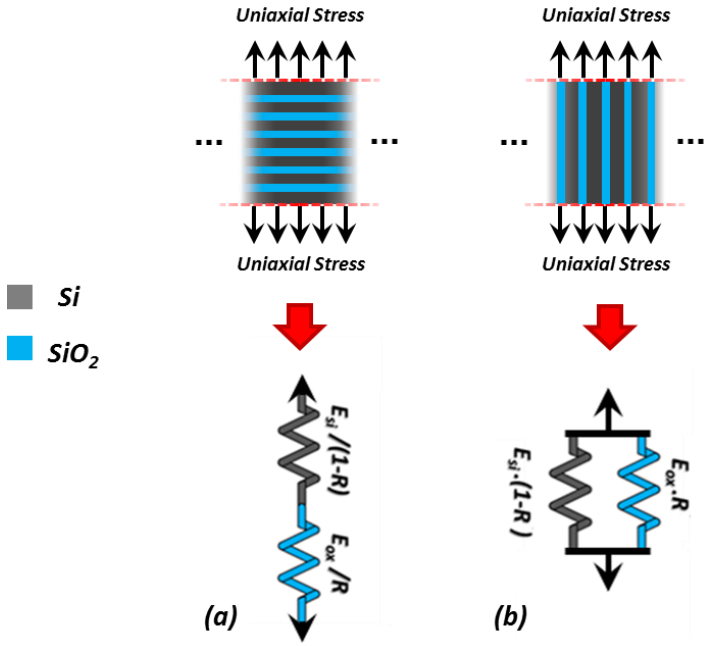

Figure 3.2: Silicon/oxide composite resonators having (a) and (b) series distribution configuration. The equivalent modulus is shown schematically as a function of silicon and oxide Young's modulus.

Considering R = V_{SiO2} / V_{cell} the equivalent Young's modulus of the structures can be formulated as:

$$E_{parallel} = R \cdot E_{SiO2} + (1 - R) \cdot E_{Si} \qquad (3.7)$$

$$E_{series} = \left(\left(\frac{E_{SiO2}}{R}\right)^{-1} + \left(\frac{E_{Si}}{1-R}\right)^{-1}\right)^{-1} \qquad (3.8)$$

Consequently, $\frac{\partial E_{comp}}{\partial E_{SiO2}} \Big/ \frac{\partial E_{comp}}{\partial E_{Si}}$ for series and parallel extremes can be written as:

$$\left(\frac{\partial E_{SilOx}}{\partial E_{SiO2}} \Big/ \frac{\partial E_{SilOx}}{\partial E_{Si}}\right)_{parallel} = \frac{R}{1-R} \qquad (3.9)$$

$$\left(\frac{\partial E_{SilOx}}{\partial E_{SiO2}} \Big/ \frac{\partial E_{SilOx}}{\partial E_{Si}}\right)_{series} = \left(\frac{E_{Si}}{E_{SiO2}}\right)^2 \cdot \frac{R}{1-R} \qquad (3.10)$$

(3.9) suggests achieving full compensation (i.e. $\frac{\partial E_{comp}}{\partial E_{SiO2}} \Big/ \frac{\partial E_{comp}}{\partial E_{Si}} = 1$) for the case of parallel oxide requires R = 0.5 (or in other words similar volumetric amount of SiO_2 and Si in the composition). However, (3.10) suggests full compensation in the series configuration can be achieved by R = 0.15 (i.e. much smaller amount of SiO_2), and this is due to the larger value of E_{Si} compared to E_{SiO2}.

This clearly shows why the fact that Si has a larger Young's modulus compared to SiO_2 (at room temperature) is playing an important role in defining the compensation efficiency of bulk vs. surface compensation techniques. In other words, in order to have least amount of additional SiO_2 (i.e. smaller R in above equations) to achieve full temperature compensation of Young's modulus, series configuration (and hence bulk compensation) is much more efficient. For any arbitrary in-plane resonance mode, the surface SiO_2 will always serve as parallel oxide. However, in bulk SiO_2 compensation technique, additional SiO_2 is partially aligned in series with silicon for any in-plane resonance mode. To conclude, a platform with uniform distribution of SiO_2 pillars (SilOx) guarantees the compensation for all arbitrary modes with in-plane particle polarization with the least amount of SiO_2.

3.3 SILOX ACOUSTIC PLATFORM WITH BULK OXIDE COMPENSATION

In micromechanical resonators, each resonance mode can be interpreted as a superposition/interaction of longitudinal and shear quasi-plane waves propagating in arbitrary directions and reflecting back from the stress-free boundaries of the structure. Therefore the distribution of the SiO_2 pillars in the Si substrate should be designed so as to (1) facilitate the propagation of the acoustic waves corresponding to the desired modes of operation without destructive dispersion and (2) provide adequate distribution in regions with high acoustic energy density.

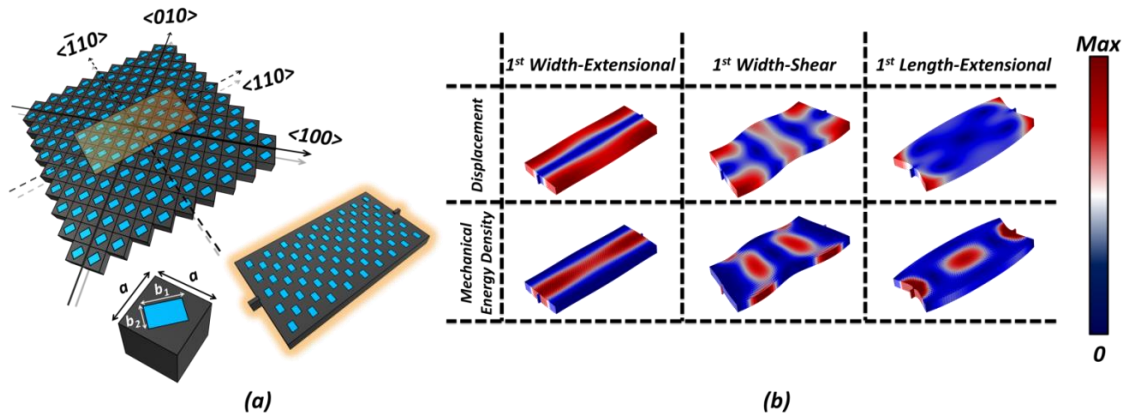

Figure 3.3: (a) Rectangular SilOx resonator. a and b1,2 are SilOx unit and SiO2 pillar lateral dimensions respectively. (b) Displacement and mechanical energy density of a rectangular SilOx resonator for its first width-extensional (WE1), width-shear (WS1) and length-extensional (LE1) modes.

Thus, in order to provide temperature compensation for desirably all resonance modes, a proper matrix of pillars should be as uniform as possible, forming a nearly homogenous silicon-oxide composite structure with temperature-compensated elastic moduli. Such a homogenous platform is called a SilOx matrix hereafter. Figure 3.3(a) shows a rectangular SilOx resonator oriented in <110> crystalline direction of silicon. Figure 3.3(b) shows the displacement and mechanical energy density fields for WE_1, WS_1 and LE_1 modes of the rectangular parallelepiped SilOx structure of figure 3.3(a) Considering the uniform distribution of SiO_2 pillars, the composite resonator shown in figure 3.3 can be regarded as an array of SilOx units (Figure 3.3(a)). For the purpose of approximate analytical modeling, these units can be replaced by an equivalent cell with similar dimensions but made of a homogeneous material. Then the equivalent elastic modulus ($\boldsymbol{\lambda}_{SilOx}$) and mass density ($\rho_{SilOx}$) can be estimated as a function of R1, the volumetric ratio of SiO_2 in the SilOx unit cell with square cross section ($R_1 = {V_{SiO2}}/{V_{cell}} = {b_1 \cdot b_2}/{a^2}$) and R_2, the in-plane aspect ratio of SiO_2 pillars ($R_2 = {b_1}/{b_2}$) .

Using these equivalent values in (3.4), R_1 and R_2 can be calculated to achieve full compensation of $TC\boldsymbol{\lambda}_1$ ($\boldsymbol{\lambda}$ = E and G) for the composite SilOx platform in desired

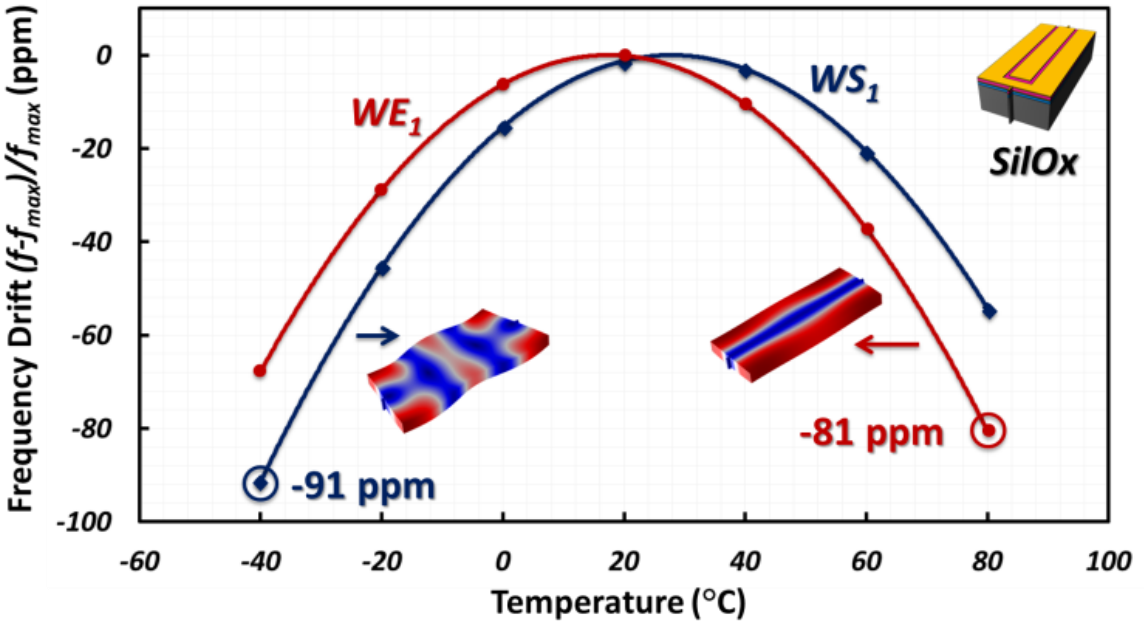

Figure 3.4: Simulated temperature characteristic of TCF_1-compensated SilOx resonator for first width-extensional (WE_1) and width-shear (WS_1) modes. R_1 and R_2 are optimized to achieve best cancellation of linear temperature dependency for the two modes.

crystalline orientation of silicon. These approximate values of R_1 and R_2 are then taken as the starting point for ANSYS numerical simulations which were used to refine first-cut designs derived from the analytical model. Lateral (in-plane) SiO_2 pillars dimensions as well as their distribution density in silicon substrate were optimized to minimize the overall frequency drift for different modes of extensional and shear types (Figure 3.3b), over the temperature range of interest. Only a few iterations of this procedure were needed to generate resonator designs that minimized the resonance frequency drift over the temperature range of interest. Figure 3.4 shows the simulated temperature characteristic of the WE_1 and WS_1 modes for a temperature-compensated SilOx resonator. Full cancelation of TCF_1 results in a quadratic temperature characteristic of the resonance frequency. Therefore the overall frequency drift over the temperature range of interest can be minimized by locating the temperature characteristic turn-over point at the center of the temperature range of interest (20°C).

3.4 FABRICATION OF SILOX RESONATORS WITH ALN TRANSDUCTION

SiO_2 pillars array is formed by etching square-shape trenches inside the device layer of an SOI wafer. These trenches were then filled by multiple deposition and etching steps of LPCVD SiO_2. This can also be done by thermal oxidation of trenches with smaller dimensions to end-up with similar pillar size after SiO_2 growth. However since higher uniformity of distribution can be achieved by SiO_2 pillars with smaller lateral dimensions, LPCVD SiO_2 is desirable since the final size of the pillar can be as small as lithography limitations to define narrow trenches.

Despite the conformal nature of LPCVD deposition of SiO_2 at high temperatures, the formation of voids inside SiO_2-filled trenches is inevitable due to higher deposition rates at the corners of trench openings. This results in the closure of these openings prior to the complete filling of the holes. In order to overcome this challenge, trenches were etched in the silicon device layer with slightly tapered sidewalls. These tapered sidewalls were achieved by controlling the time ratio of etching to passivation cycles in the Bosch DRIE process. The longer time needed for the larger openings of these tapered trenches to get closed by SiO_2 resulted in a more efficient filling of trenches. Table 3.1 compares Bosch process recipes used to achieve straight and tapered sidewalls. By increasing the etching to passivation cycle time ratio from 7.5/5 to 7.8/5, tapered sidewalls inclined at an angle of 86-88° were achieved.

Table 3.1: Comparison of Bosch DRIE recipes used to achieve high aspect ratio trenches with straight and tapered sidewall

Sidewall	Straight	Tapered
Cycle length (etch/passivation)	7.5s/5s	7.8s/5s
Gas (etch/passivation)	150 sccm SF_6, 15 sccm O_2 /100 sccm C_4F_8	150 sccm SF_6, 15 sccm O_2 /100 sccm C_4F_8
Coil power (etch/passivation)	600W/600W	600W/600W
Platen power (etch/passivation)	12W/0W	12W/0W

Figure 3.5 shows the cross-section of tapered trenches.

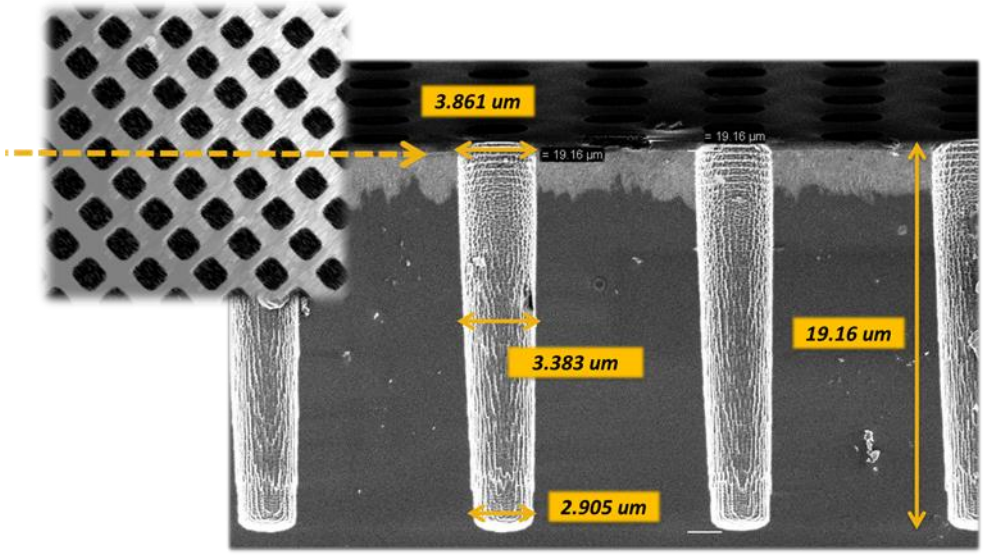

Figure 3.5: Top and cross-sectional view of tapered trenches etched in silicon substrate using recipe explained in table 3.1.

After formation of the trenches, conformal LPCVD SiO_2 was deposited at 850 °C until the closure of the trench openings, still resulting in the formation of partially filled holes. However, the void space inside the pillars decreases considerably as a result of the tapered sidewalls, and can be further reduced by using DRIE etching of SiO_2 in an ICP tool to open the trenches again for further deposition of SiO_2. This has been done by complete removal of SiO_2 on the surface, as well as 0.7-1μm of SiO_2 inside the trenches.

Figure 3.6(a) shows the cross-section view of the trenches after first deposition of LPCVD oxide and removal of the surface oxide to open the voids for further deposition. Figure 3.6(b) shows the reduction in void size and depth after the subsequent oxide deposition.

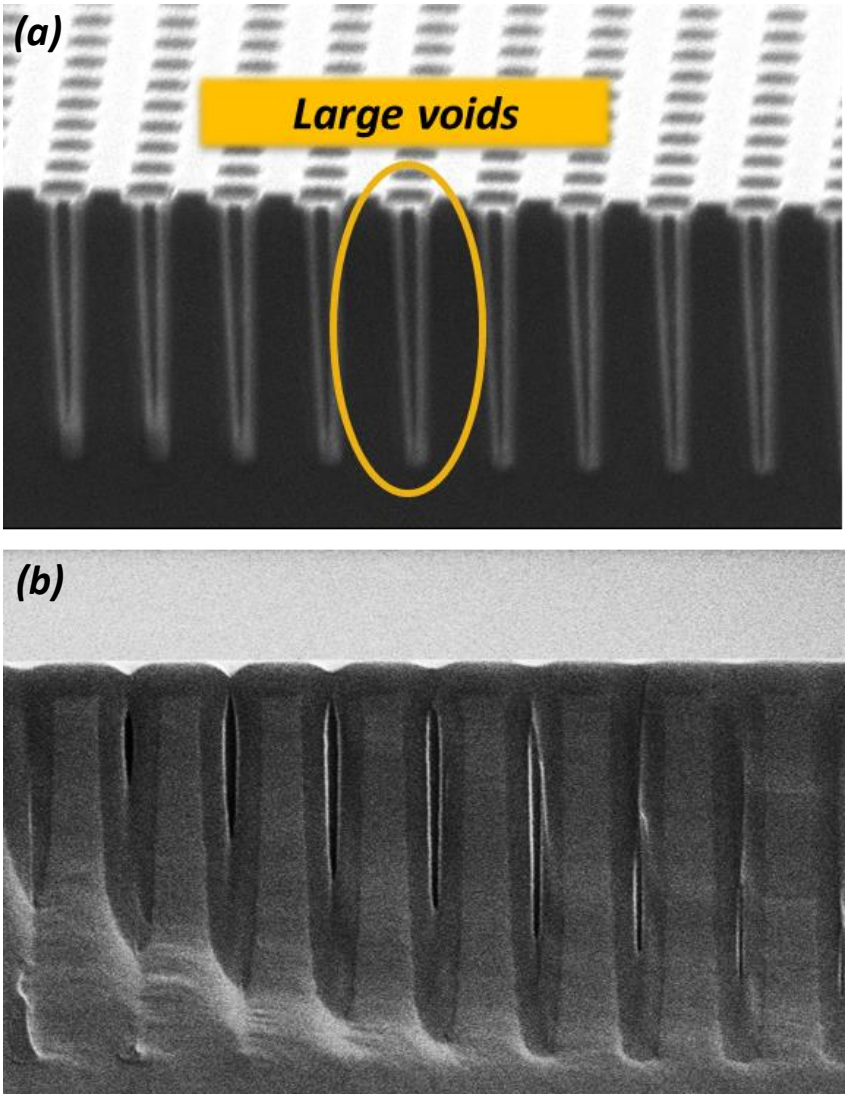

Figure 3.6: Cross-section view of SilOx substrate after (a) first deposition of LPCVD oxide and removal of the surface oxide to open voids and (b) after second deposition of LPCVD oxide to fill voids.

Figure 3.7 shows the complete process used to fabricate SilOx BAW resonators with AlN piezoelectric transduction.

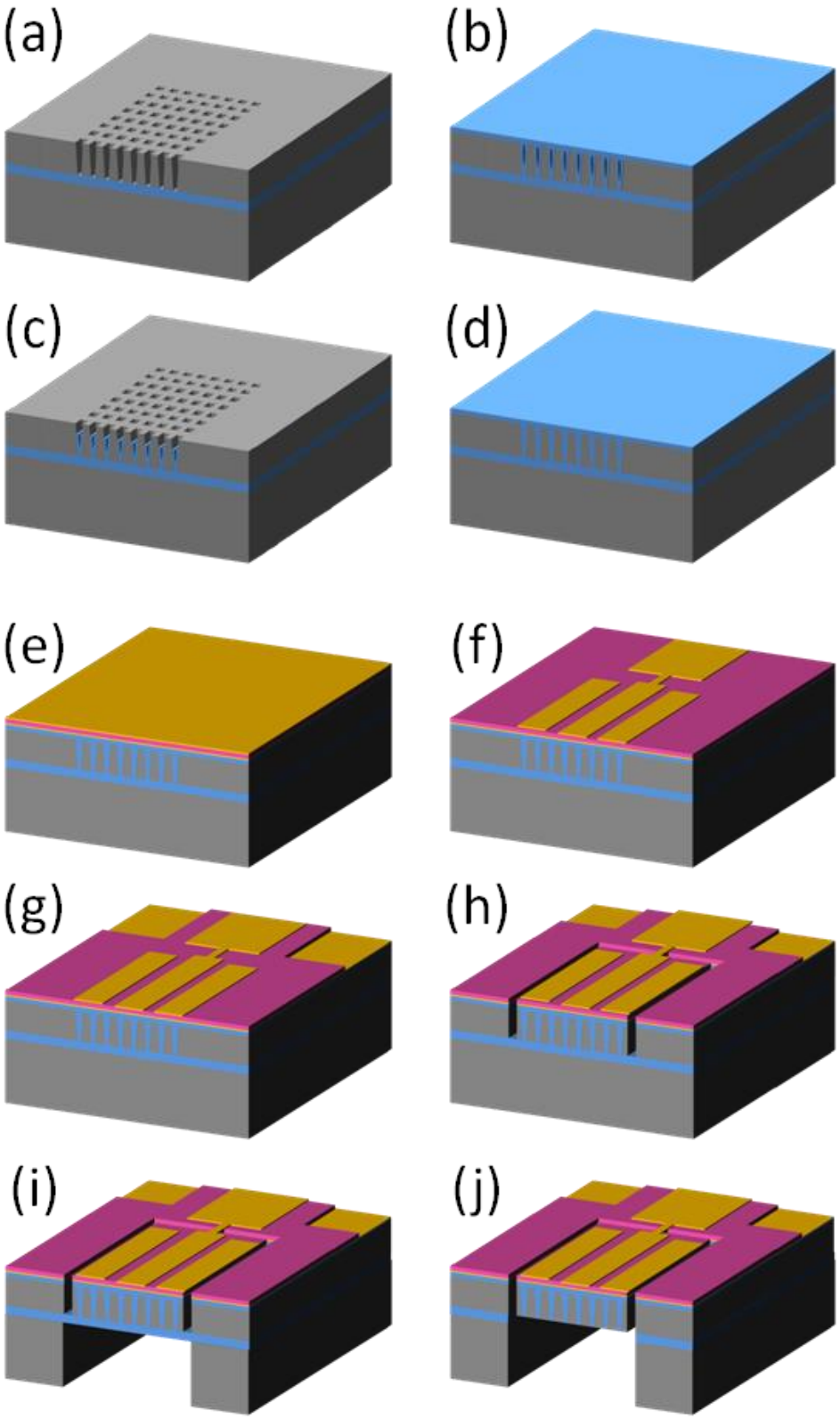

Figure 3.7: The fabrication process flow: (a-d) preparation of silicon substrate with embedded oxide pillars (SilOx). (e) deposition of Mo/AlN/Mo stack; (f) patterning top Mo; (g) patterning AlN to access bottom Mo; (h) etching trenches around the resonator; (i-j) releasing the resonator by dry etching silicon handle layer as well as BOX layer.

The initial three steps consist of the preparation of partially filled silicon substrates, which were described above in detail. These steps were followed by the deposition of a thick layer of LPCVD SiO_2 in order to achieve nearly void-free pillars and to create a layer of SiO_2 with a thickness of 3μm on the surface. Since a smooth surface is required for the deposition of a high-quality AlN layer with the C-axis perpendicular to the surface, the SiO_2 layer was thinned down to 1.4μm by wet etching in BOE to decrease surface roughness. Then a 0.5 μm layer of AlN sandwiched between 50nm Mo films was deposited on the substrate using reactive magnetron sputtering. The top Mo layer was then patterned to form the top electrodes using DRIE etching with a mixture of SF_6/O_2 gases. This process has very high selectivity with respect to AlN. Next, in order to access the bottom Mo layer, which serves as bottom electrode, AlN was patterned using TMAH at 40°C. This was followed by DRIE of a thick stack including Mo, AlN, SiO_2 and Si layers. A fairly thick SiO_2 layer was used as hard mask in the trench etching step. Finally the device was released by dry etching of the silicon handle and buried oxide layers from the backside of the wafer. Figure 3.8 shows the SEM images of a fabricated SilOx resonator with AlN piezoelectric signal transduction. The SiO_2 pillars are made visible by purposely over-etching the silicon body of the resonator from a backside release opening.

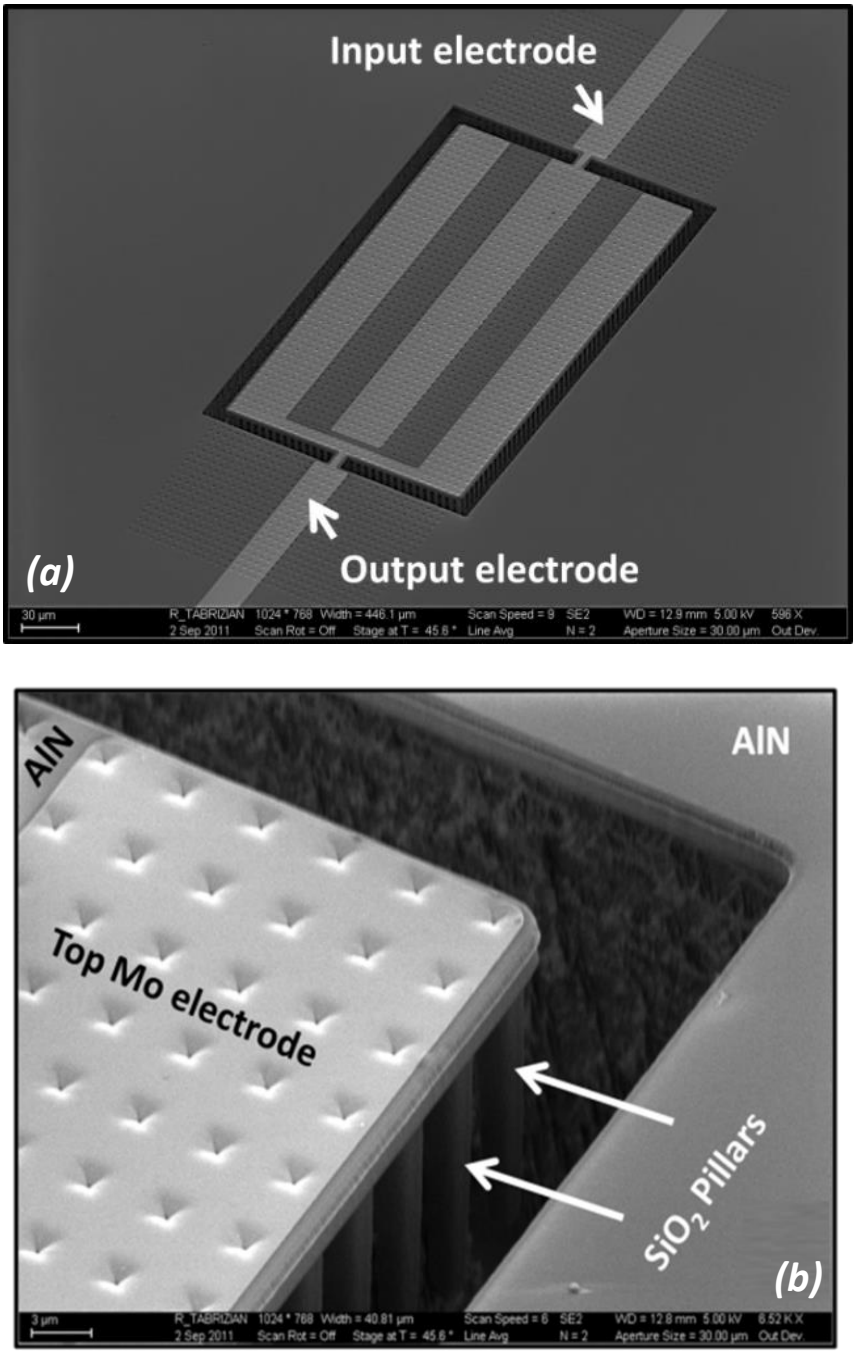

Figure 3.8: SEM images of (a) temperature-stable AlN-on-SilOx resonator and (b) SiO_2 pillars extruding from the resonator sidewall.

3.5 CHARACTERIZATION OF ALN-ON-SILOX RESONATORS

Any SilOx resonator may possess multiple resonance modes in the vicinity of the desired temperature-compensated modes, some of which may be under/over-compensated over

the temperature range of interest or have a turn-over point of temperature characteristic in undesirably low or high temperatures. In frequency reference applications the oscillator may lock in to any of the excited modes in the operation band of the trans-impedance amplifier. Therefore proper design of the electromechanical transducer is essential to excite the resonance modes of interest, while suppressing undesired spurious modes situated in a relatively wide frequency span around it. In this work, AlN piezoelectric transduction has been used since mode selection and suppression can be easily done by proper patterning of the metallic electrodes. Furthermore, since this transduction scheme does not require a DC polarization voltage for operation, it is intrinsically immune to dielectric charging effect which may induce frequency fluctuations over time in capacitive resonators with surface SiO_2 compensation [34]. Figure 3.9 shows the frequency response of a rectangular SilOx resonator with an electrode design resulting in excitation of all first width and length-extensional as well as width-shear modes in a 10 MHz frequency span.

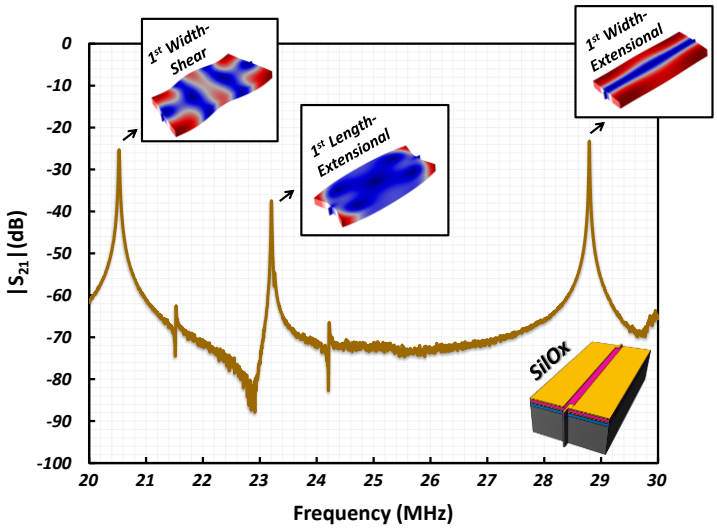

Figure 3.9: Measured large-span frequency response of a SilOx resonator with proper electrode configuration to excite three modes in the measured span.

Figure 3.10 shows the frequency response of a 26.3 MHz SilOx resonator with proper electrode configuration for excitation of the 1st WE mode in a spurious-free 10MHz span. The IL of the WE_1 resonance mode is more than 50 dB higher than the noise floor, thus facilitating the implementation of MEMS oscillators without any concern about locking to an undesired mode.

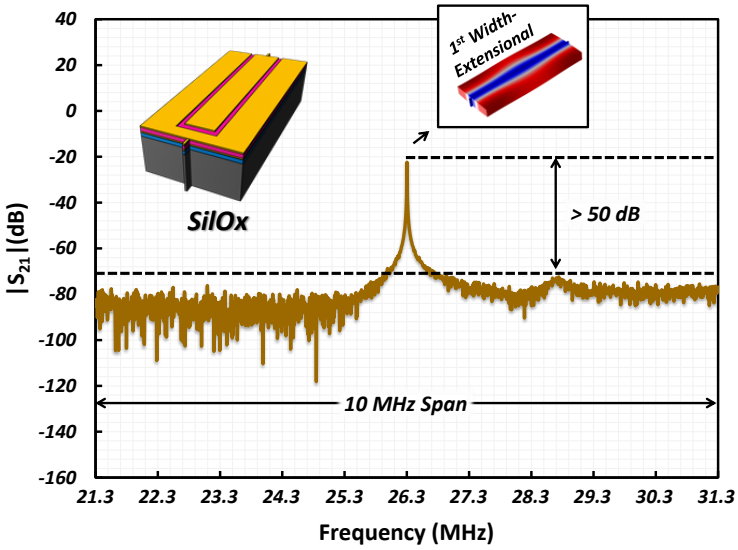

Figure 3.10: Measured frequency response of a SilOx resonator with proper AlN transducer designed for effective excitation of WE_1 mode, resulting in a spurious-free 10 MHz span around the temperature-compensated resonance mode.

3.5.1 Resonator Performance Characterization

Two-port SilOx resonators were tested in a temperature-controlled environmental chamber. A vector network analyzer (VNA) in two-port configuration was used to measure the frequency response of the devices as well as their temperature characteristics. Figure 3.11 shows the frequency response of the SilOx resonator in a 100 kHz frequency span around the WE_1 resonance mode. A high *Q* of ~10,000 was measured at 26.3 MHz in air with an IL of -22.35 dB.

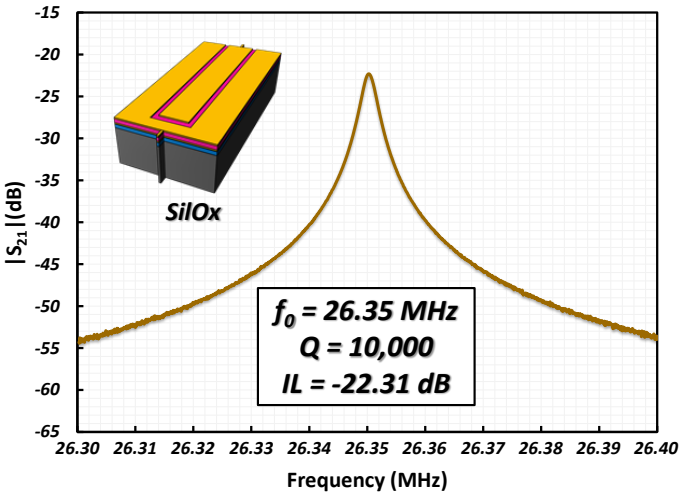

Figure 3.11: Measured frequency response of the of the SilOx resonator in a 100 kHz frequency span around its WE_1 resonance mode, measured in air.

3.5.2 TEMPERATURE CHARACTERIZATION

The temperature characteristics of the SilOx resonators were measured over the range of -40°C to 80°C and compared with their SCS counterparts implemented in the same batch. Figure 3.12 shows the temperature characteristic of the resonance frequency for WE_1, WS_1 and LE_1 modes of SCS and SilOx resonators with similar dimensions and electrode configuration.

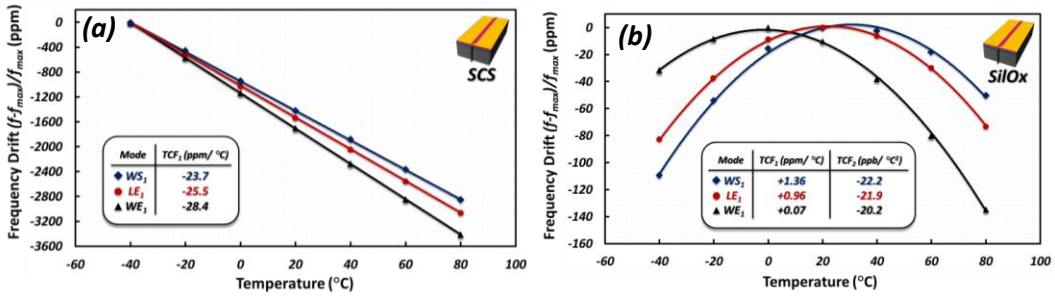

Figure 3.12: Measured temperature characteristic of the resonance frequency of three different resonance modes of (a) SCS and (b) SilOx resonators. The electrode configuration used for excitation of all modes is shown as well.

The difference between TCF_1 of different modes in the SCS device is due to the difference in the temperature coefficients of the stiffness constants of silicon [35]. In the case of SilOx resonator, the TCF_1 compensation has been achieved for several in-plane

resonance modes of a single device. Frequency drifts as small as 83 ppm were measured for WE_1 mode over the entire temperature range of -40°C to 80°C. This corresponds to a 40 times improvement in the overall frequency drift compared to a non-compensated silicon resonator. Furthermore, the quadratic temperature characteristic achieved by cancelation of TCF_1 possesses a turnover point between 20-25 °C with a zero TCF_1. This is very close to the turn-over point of the simulated temperature characteristic (20°C), which guarantees the minimum overall frequency drift over the temperature range of -40°C to 80°C. However, higher turn-over temperatures may be required for oven-controlled crystal oscillator (OCXO) applications since they need to operate at a constant temperature exceeding the operational temperature range of interest (typically 90°C). This can be achieved lithographically by a slight modification of the volumetric ratio of oxide in SilOx unit (R_1) to locate the turn-over point at a higher temperature (Figure 3.12). SilOx temperature-compensated resonators exhibit robust Q over the entire temperature range. Figure 3.13 compares the Q temperature characteristic of the SilOx resonator with its SCS counterpart with similar dimension and transducer configuration.

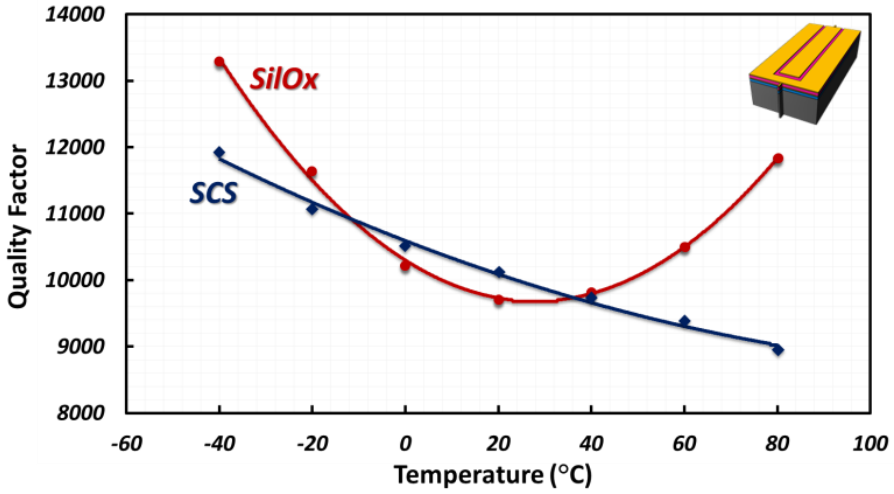

Figure 3.13: Measured temperature characteristic of the Q for SCS and SilOx resonators with similar dimensions and transducer configuration, operating in WE_1 mode.

Besides providing high performance temperature-compensated in-plane WE, LE and WS modes, SilOx platforms can be optimized to provide temperature-compensated thickness modes with high quality factors. Figure 3.14 shows the large-span frequency response of a rectangular SilOx resonator. The resonance frequencies and measured *Q* values of three in- and out-of-plane extensional modes are shown (Figure 3.14a), while their temperature characteristics of resonance frequency are compared (Figure 3.14b).

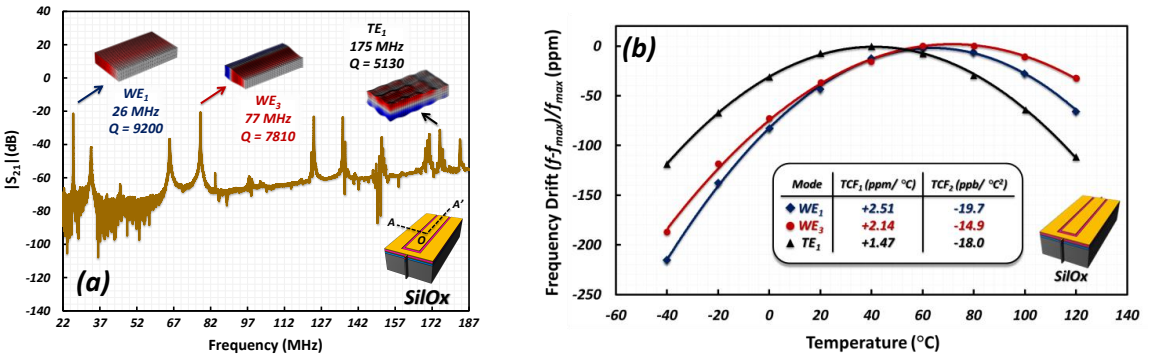

Figure 3.14: (a) Large span frequency response of a rectangular SilOx resonator; (b) temperature characteristic of resonance frequency for the first and third width-extensional ($WE_{1,3}$) and the first thickness-extensional (TE_1) modes.

Unlike in-plane extensional and shear modes, where the resonance frequency can be defined lithographically and is independent of resonator thickness, the resonance frequency of the thickness-extensional mode is mainly defined by the thickness of the structure as well as the distribution density of SiO_2 pillars. Hence, by selecting appropriate thicknesses, SilOx resonators can be implemented to provide two high-*Q* temperature-compensated modes with independent resonance frequencies and orthogonal particle displacement. This can potentially cut the manufacturing cost of MEMS temperature-stable oscillators into half, since a single device can be used as a frequency reference at two substantially different and independent frequencies.

3.5.3 STABILITY

To measure the resonance frequency stability of SilOx resonators, a number of devices were mounted on boards using a small piece of copper tape and wire-bonded to SMA connector pads. Both long-term stability and short-term hysteresis measurements were performed by placing the mounted test boards under a ~100 μtorr vacuum inside a temperature-controlled environmental chamber. This was done to eliminate any possible environmental source of frequency and *Q* perturbation. The temperature accuracy of the environmental chamber was ±1°C. Figure 3.15 shows the long-term stability of the resonance frequency for a temperature-stable SilOx resonator. An elevated temperature of 100°C was used to accelerate aging processes requiring thermal activation energy.

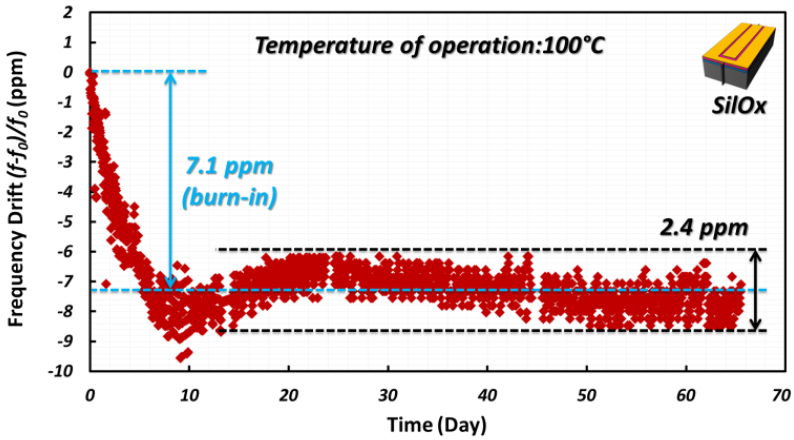

Figure 3.15: Long-term stability of the resonance frequency for a temperature-stable SilOx resonator operating in WE_1 mode at 100°C; burn-in period as well as stabilized range of operation are indicated.

A burn-in drift of 7.1 ppm over a period of ~10 days was observed in these resonators prior to frequency stabilization. This burn-in drift is comparable to that of quartz crystal resonators [36] and can be attributed to the large effective surface between Si and SiO_2 in SilOx resonators which can aggravate the stress induced due to CTE mismatch at the interface of SiO_2 pillars and SCS. After the burn-in period, a frequency fluctuation of ±1.2 ppm was observed. Considering the local TCF_1 of -3 ppm/°C at 100°C

$\left(\text{i.e. } \frac{1}{f_0} \cdot \frac{\partial f_0}{\partial T}|_{T=100°C} = -3\ \text{ppm}/°C\right)$ for the SilOx resonator beside temperature accuracy of the measurement unit, this variation can be attributed to temperature instabilities of environmental chamber and the resolution of temperature sensor.

Beside long-term stability, short-term hysteresis measurement was also performed on SilOx resonators to study the effect of rapid environmental temperature changes. Since SilOx composite resonators with AlN signal transduction are composed of different materials with various CTEs, rapid temperature variations may induce axial stresses, resulting in frequency drifts or even cracks in the device [37].

Hysteresis characterization was done by applying temperature cycles to the resonator and monitoring its resonance frequency and Q. For this purpose, the temperature was rapidly ramped down from 120°C to -40°C and then ramped up back to 120°C. A temperature stabilization time of one hour was considered between consecutive temperature changes prior to frequency and Q measurements. Figure 3.16 shows the measurement results for short-term hysteresis characterization after 22 cycles for resonance frequency and Q. The stabilization behavior observed in the hysteresis characteristic of the resonance frequency is similar to the long-term stabilization at the elevated temperature (Figure 3.15). However, the stabilization period has been considerably reduced in response to the rapid temperature cycling. This can be attributed to the higher efficiency of stress-release and thermo-mechanical processes in the resonator for the temperature cycling case. Overall frequency fluctuations of 1.6 ppm and 3.2 ppm were measured respectively, for 120°C and -40°C temperature points of the cycles in the stabilized period, while the Q remained stable after a slight increase over the stabilization period. The small frequency fluctuations can be attributed to the non-zero

local TCF_1 of the measured device at two different temperatures and ±1°C temperature accuracy of the chamber.

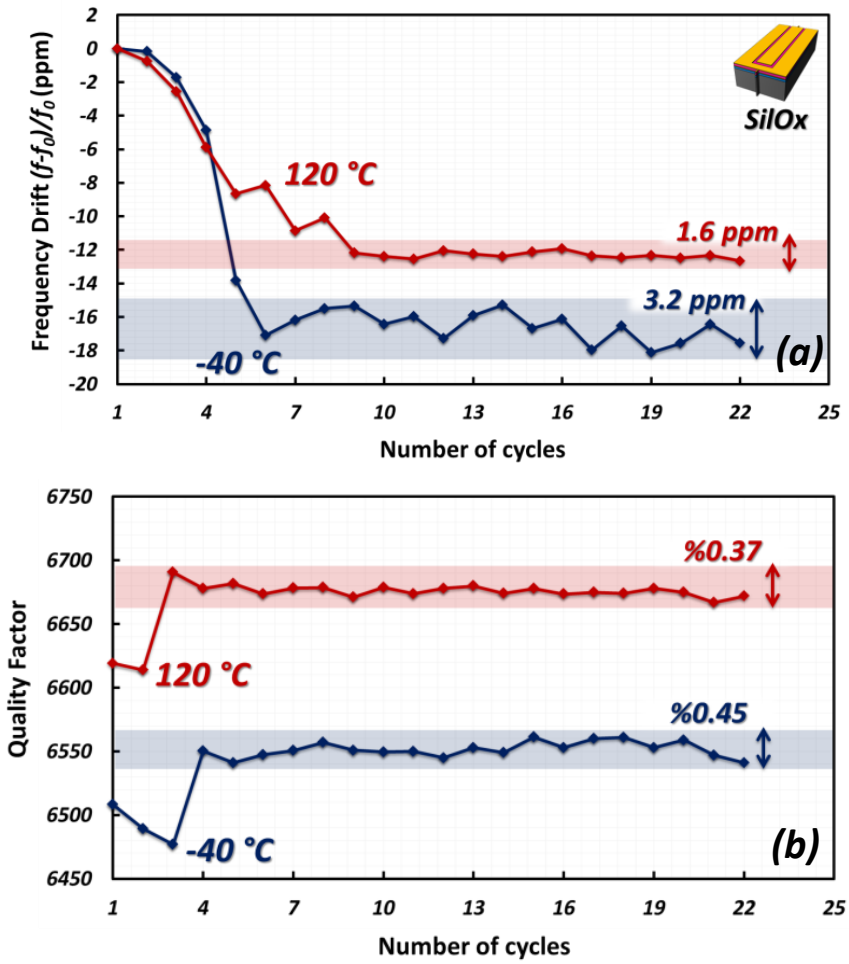

Figure 3.16: Hysteresis characteristics of (a) resonance frequency and (b) Q of a SilOx resonator operating in WE_1 mode. The resonance frequency and Q of the device have been measured after upward and downward halves of 22 consecutive wide temperature cycles between -40°C and 120°C, to evaluate performance stability under rapid temperature fluctuations. Each measurement took place after holding for 1 hour to reach thermal equilibrium.

3.5.4 POWER HANDLING

The power handling characteristic of SilOx resonators has been measured. Figure 3.17 compares the resonance frequency drift with applied input power which is a measure of resonator's linearity averaged on a group of 10 resonators for each SilOx configuration as well as SCS devices. Higher power handling and linearity of SilOx resonators can be attributed to the partial cancellation of Si and SiO_2 third order elastic moduli which are

opposite in sign [38], [39]. Superior linearity characteristic of checkerboard SilOx resonators is a result of highly uniform distribution of SiO_2 pillars in this configuration.

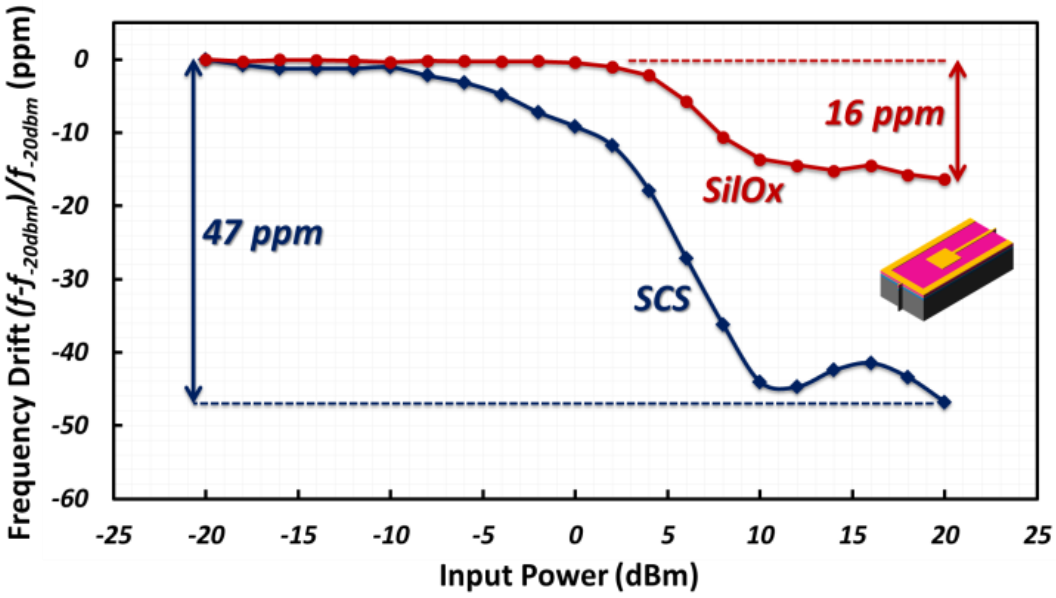

Figure 3.17: Power handling and linearity characteristic of the SilOx resonators in comparison with their SCS counterparts when devices are operating in WE_1 mode.

3.6 TEMPERATURE-STABLE SILOX OSCILLATORS WITH SUB-PPM INSTABILITY

SilOx resonators can be used for implementation of highly-stable temperature compensated MEMS oscillators. In these oscillators, electronic tuning can be used to further reduce the thermal drift in resonance frequency of SilOx resonator. The main challenge in using circuit techniques for this task is the presence of large parasitic shunt capacitances in the device, resulted from large dielectric constant of AlN and extended Mo pads required for efficient transduction. These shunt capacitances considerably limit the frequency pulling range and hence the electronic tuning efficiency. To maximize the available tuning range, electronic cancellation of these shunt capacitances is achieved by using active inductors to resonate out the shunt parasitic capacitances. For this purpose,

high-Q tunable active inductors are implemented on-chip to provide the specific value of the emulated inductor required for parasitic compensation.

Selectable on-chip capacitor-banks in addition to a phase-shifter have been placed in the feedback loop to provide required electronic tuning of the resonance frequency at the operating temperature. Figure 3.18 shows the system block diagram for the compensated MEMS oscillator. A TIA-based sustaining amplifier is used to reduce the input referred noise, and to minimize the loading of the resonant device. The inverter-based TIA offers about 100dB gain and embeds the phase-shifter for tuning. The switched scheme of the capacitor banks provides about 60ppm of tuning (in discrete steps of 15ppm/step) while the TIA phase-shifter provides 60ppm of continuous tuning with high precision.

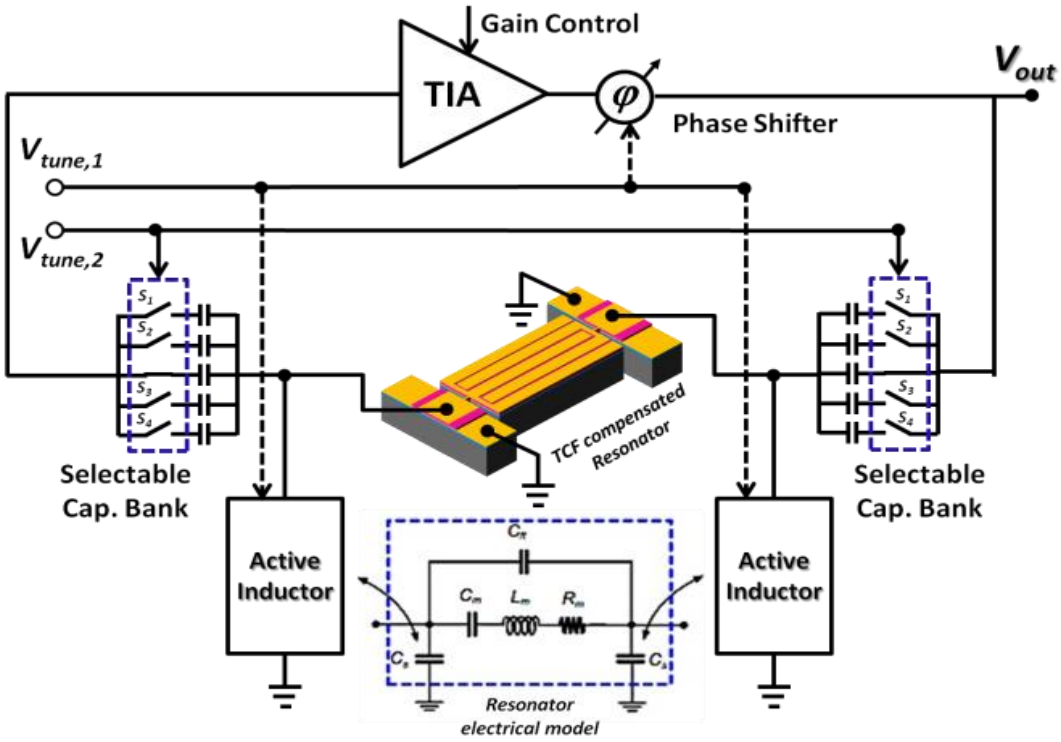

Figure 3.18: The system block diagram for the 27 MHz temperature-compensated MEMS oscillator.

3.6.1 OSCILLATOR CHARACTERIZATION

Figure 3.19 shows the PN performance measured for 6 temperature points.

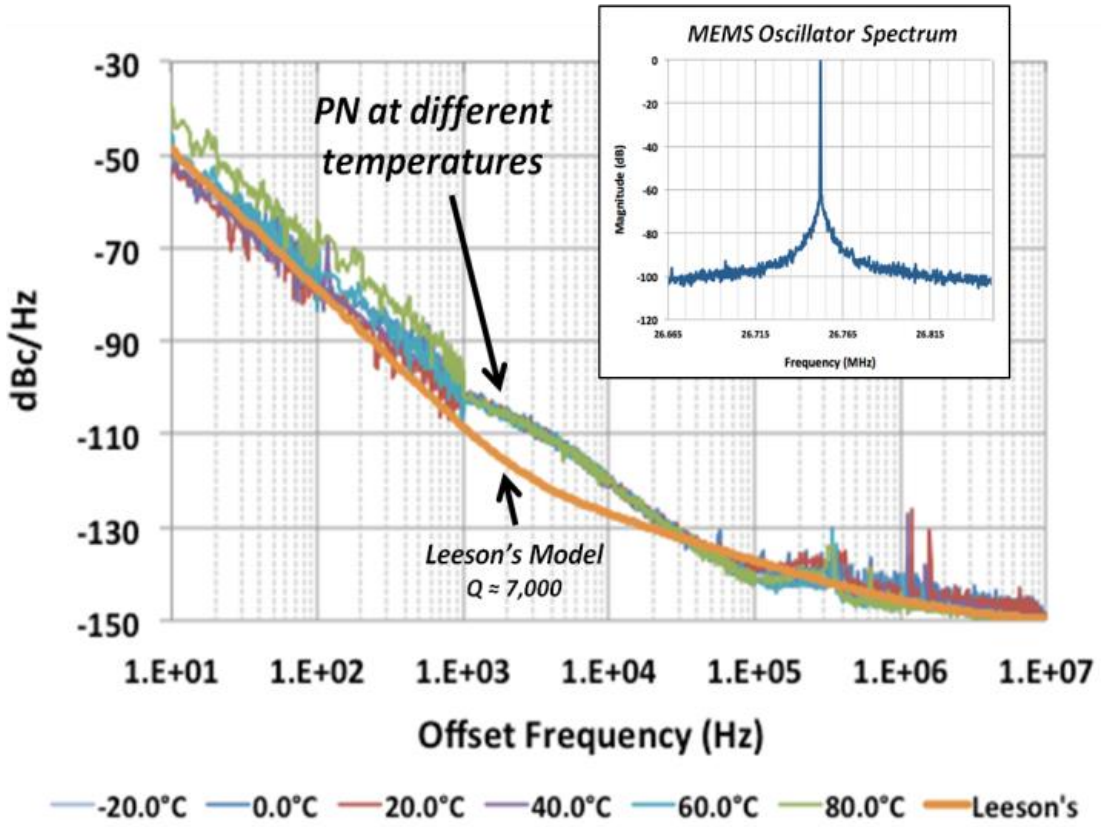

Figure 3.19: Phase noise performance of temperature-compensated oscillator at 6 temperature points showing consistent behavior over the temperature range.

A PN of -101dBc/Hz at 1 kHz offset-frequency with consistent behavior across the entire temperature range is measured for the temperature-compensated MEMS oscillator. This is the lowest reported PN to date for any temperature compensated MEMS oscillator with sub-ppm temperature instability. Figure 3.20 shows the result of stability measurement for the oscillator operating in air, which has been carried out in a chamber with temperature-control accuracy of ±0.3°C at 6 different temperature points after applying required tuning to operate at a constant frequency with an accuracy of ±0.1 Hz (< 4ppb). This accuracy is provided by fine frequency tuning available from phase shifter and is limited by the resolution of frequency measurement setup (Agilent 53181A).

Interestingly, the stability result at 40°C, which corresponds to the local-zero-TCF region of the resonator, shows a variation of less than 100ppb.

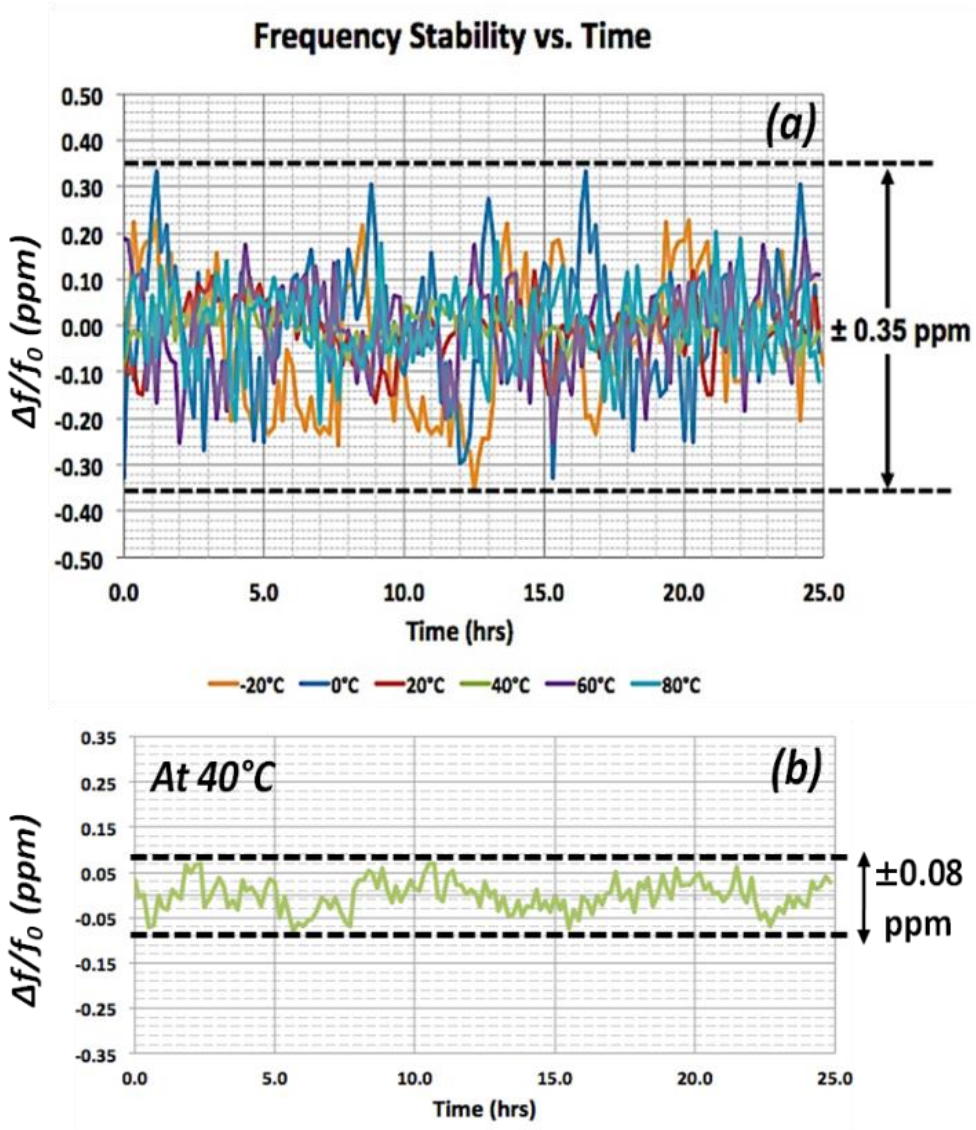

Figure 3.20: Steady-state stability measurement for fully-compensated oscillator after applying active tuning to operate at f0 ±0.1 Hz (a) at 6 temperature points; (b) at 40°C.

4 SILICON RESONATORS AS ENGINEERED ACOUSTIC WAVEGUIDS

This chapter presents several novel groups of microresonators designed based on an alternative and also more accurate formulization of acoustic resonance modes in solid micro-structures. Silicon resonators can be considered as 3D acoustic waveguides with finite dimensions. Based on this interpretation, resonance modes of the resonator can be considered as interaction of one or multiple guided waves propagating in arbitrary directions and reflected back from stress- or strain-free boundaries. Such formulation helps in explanation of several performance features and metrics of the microresonator including spurious modes, TCFs and Qs. The chapter starts with an introduction to the novel formulation in contrary with the current/previous common perception in MEMS community. After the introduction (section 4.1), section 4.2 introduces guided waves in silicon acoustic waveguides and their temperature characteristics. The rest of the chapter is dedicated to novel applications of acoustic engineering in silicon micro-resonators. Section 4.3 introduces mixed-mode high-Q and low-TCF resonators. Section 4.4 introduces acoustically-engineered tetherless resonators with energy-trapped modes and spurious suppression. Finally section 4.5 exploits the whole theory developed in the rest of the chapter to introduce acoustically-engineered multi-port resonators for accurate temperature sensing applications.

4.1 INTRODUCTION

Conventionally, different resonance modes of the microstructures have been named based on their acoustic wave constituents. As a result numerous MEMS resonators operating in flexural, shear and extensional modes with high Qs have been implemented

and reported throughout MEMS resonator short, yet fruitful, history. The earliest demonstrations of Quartz/MEMS resonators mainly include devices operating in low-frequency flexural/shear modes of mechanical structures. However, evolutionary advancements in micro-fabrication technologies facilitate integration of highly-efficient electromechanical transducers, providing large mechanical forces required for excitation of high-frequency extensional (or dilatational) modes in the micro-structures.

The fast development of MEMS resonators for relatively narrow consumer applications such as timing and signal processing, has resulted in a major focus on acoustically well-understood flexural and shear/extensional bulk modes among numerous acoustic modes which can be excited in a micro-structure. In this sense, other modes have been usually considered as spurs desired/required for suppression.

Recently, especial TCF characteristic of extensional and shear bulk modes in doped-silicon resonators have been reported and further studied, which highlights the superior advantage of doped-semiconductor materials to engineer temperature characteristic of the resonator. This further suggests the possibility of employing dissimilar temperature characteristic of different elastic coefficient of doped-silicon to implement resonators operating in TCF-engineered modes. An experimental demonstration of such modes is reported in geometrically-engineered silicon resonator with exceptionally ultra-high Q and low TCF. The unique resonance mode of these concave microstructures along with other non-bulk modes in rectangular silicon resonators each of them showing specific characteristics, cannot be simply categorized under either of flexural or bulk shear/extensional group of modes; thus necessitating a redefinition of acoustic modes in microstructures. This requires a thorough understanding

of the resonance modes by studying their constituent acoustic waves propagating in micro-structures with finite dimensions. This chapter can be considered as the first word on redefinition of resonance modes in MEMS structures based on their constituent guided acoustic waves, as well as several applications facilitated by such redefinition. As stated in chapter 1, TPOS platforms are essential for such study and its further applications, since it provides multiple exceptional and unique degrees of freedom including, among others, different temperature characteristic for different elastic constants, feasibility of selective, yet efficient, transduction of different modes with arbitrary particle polarizations and thickness control of the microstructure.

4.2 GUIDED WAVES IN SILICON PARALLELEPIPED

In acoustic MEMS terminology, bulk acoustic wave (BAW) is attributed to plane waves with an arbitrary polarization, propagating in a specific direction in solids with infinite dimensions. These waves can also exist (purely) in plates with finite thickness but infinite lateral dimensions (known as slab waveguide) if the propagation direction is normal to the boundary faces of the plate. However, propagating waves which may exist in a slab waveguide are not limited to BAWs. Different groups of waves which can propagate in a specific in-plane direction of a slab waveguide can be categorized based on their particle polarization into shear-horizontal and Lamb modes (all known universally as guided waves). The finite thickness of the slab waveguide results in dispersive behavior of propagating waves (i.e. the dependence of propagation velocity on the frequency), which defines the frequency of a guided wave as a specific function of its wavelength; thus resulting in a specific dispersion curve for each mode. Although thickness BAW resonance modes are created from interaction of BAWs reflected at two

stress-free faces of the slab waveguide, they can alternatively be defined as guided waves with infinitely large wavelengths. Figure 4.1 demonstrates different Lamb modes propagating in a silicon plate, for different wavelengths.

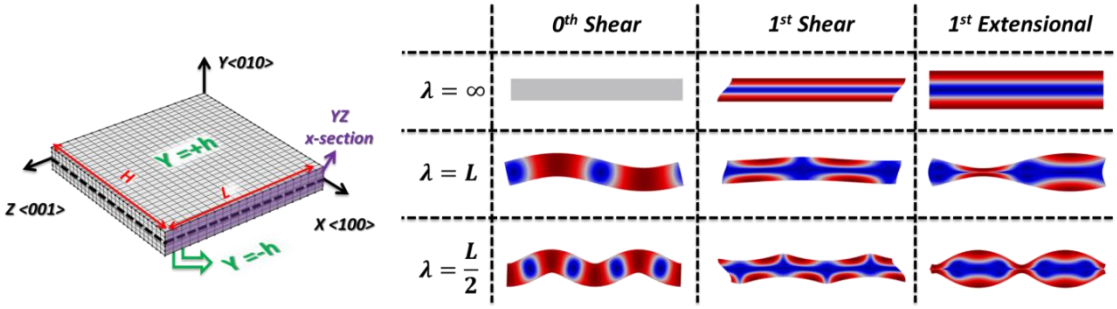

Figure 4.1: Silicon plate of width (2h) and infinitely large lateral area (left); three different guided modes with different wavelengths.

The Christoffel's equation for wave propagation in anisotropic solid [40] can be used to extract dispersion characteristics of guided waves propagating in Z <001> direction of a Y (010) silicon substrate:

$$\begin{bmatrix} \frac{\partial}{\partial x} & 0 & 0 & 0 & \frac{\partial}{\partial z} & \frac{\partial}{\partial y} \\ 0 & \frac{\partial}{\partial y} & 0 & \frac{\partial}{\partial z} & 0 & \frac{\partial}{\partial x} \\ 0 & 0 & \frac{\partial}{\partial z} & \frac{\partial}{\partial y} & \frac{\partial}{\partial x} & 0 \end{bmatrix} \begin{bmatrix} C_{11} & C_{12} & C_{13} & 0 & 0 & 0 \\ C_{21} & C_{22} & C_{23} & 0 & 0 & 0 \\ C_{31} & C_{32} & C_{33} & 0 & 0 & 0 \\ 0 & 0 & 0 & C_{44} & 0 & 0 \\ 0 & 0 & 0 & 0 & C_{55} & 0 \\ 0 & 0 & 0 & 0 & 0 & C_{66} \end{bmatrix} \begin{bmatrix} \frac{\partial}{\partial x} & 0 & 0 \\ 0 & \frac{\partial}{\partial y} & \frac{\partial}{\partial z} \\ 0 & \frac{\partial}{\partial z} & \frac{\partial}{\partial y} \\ \frac{\partial}{\partial z} & 0 & \frac{\partial}{\partial x} \\ \frac{\partial}{\partial y} & \frac{\partial}{\partial x} & 0 \end{bmatrix} \begin{bmatrix} 0 \\ U_y(y)e^{kz-\omega t} \\ U_z(y)e^{kz-\omega t} \end{bmatrix} =$$

$$\begin{bmatrix} 0 \\ -\rho\omega^2 U_y(y)e^{kz-\omega t} \\ -\rho\omega^2 U_z(y)e^{kz-\omega t} \end{bmatrix} \quad (4.1)$$

Here U_y and U_z are particle polarization amplitudes in Y and Z direction. K is the wave number. ω is the frequency in radian, and c_{ij} are elastic coefficients are SCS. (4.1) reduces to coupled differential equation set of:

$$\frac{d^2U_y}{dy^2} + \left(\frac{\rho\omega^2}{c_{22}} - \frac{c_{44}}{c_{22}}k^2\right)U_y + \frac{dU_z}{dy}\left(ik\frac{c_{23}+c_{44}}{c_{22}}\right) = 0 \;\&\; \frac{d^2U_z}{dy^2} + \left(\frac{\rho\omega^2}{c_{44}} - \frac{c_{33}}{c_{44}}k^2\right)U_z +$$

$$\frac{dU_y}{dy}\left(ik\frac{c_{23}+c_{44}}{c_{44}}\right) = 0 \quad (4.2)$$

Solving for equation set (4.2) considering stress-free boundaries at Y=±h, dispersion characteristic of these modes is:

$$\frac{\tan(p_2 h)}{\tan(p_1 h)} = \frac{\left(\frac{\rho\omega^2 - c_{44}k^2 - c_{22}{p_1}^2}{(c_{23}+c_{44})k} + k\right)\left(c_{22}p_2 + c_{23}\frac{\rho\omega^2 - c_{44}k^2 - c_{22}{p_2}^2}{p_2(c_{23}+c_{44})}\right)}{\left(\frac{\rho\omega^2 - c_{44}k^2 - c_{22}{p_2}^2}{(c_{23}+c_{44})k} + k\right)\left(c_{22}p_1 + c_{23}\frac{\rho\omega^2 - c_{44}k^2 - c_{22}{p_1}^2}{p_1(c_{23}+c_{44})k}\right)} \qquad (4.3)$$

where $p_{1,2}$ are the roots of:

$$(\rho\omega^2 - c_{44}k^2 - c_{22}p^2)(\rho\omega^2 - c_{22}k^2 - c_{44}p^2) = p^2k^2(c_{23} + c_{44})^2 \qquad (4.4)$$

The bisection method was used to numerically solve (4.3) and (4.4), thus resulting in dispersion curves in Figure 4.2 for h=25 μm and for waves propagating in <110> direction of a (100) single crystal silicon plate.

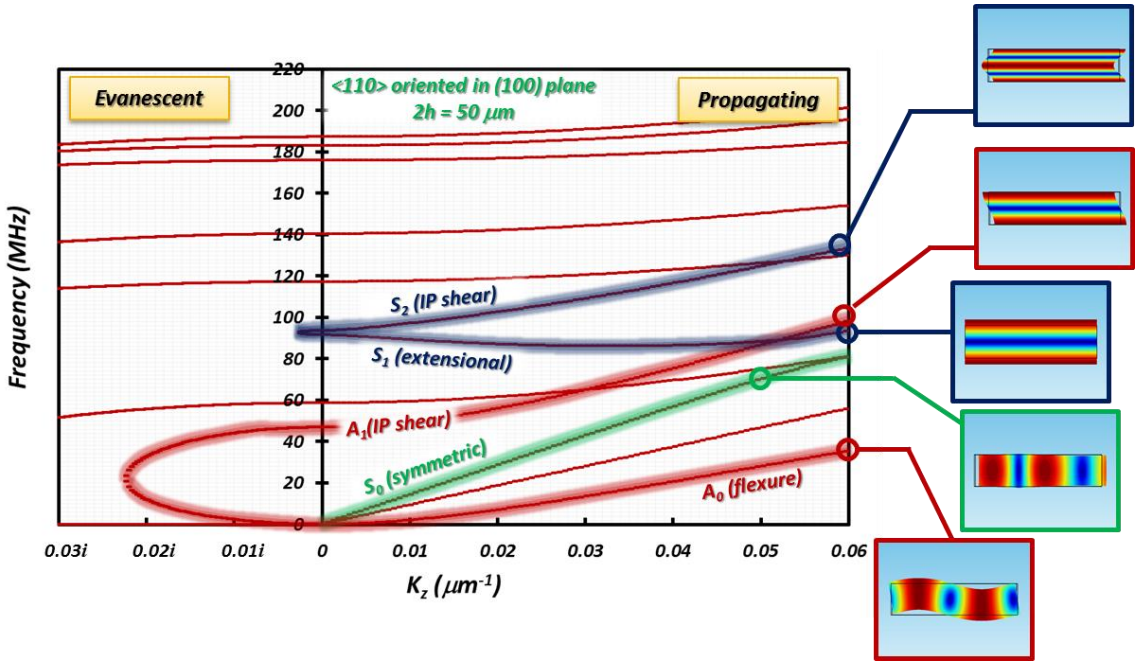

Figure 4.2: Dispersion characteristics of several guided waves in 50μm thick SCS plate for waves propagating in <110> direction of a (100) plate.

Both propagating (real K) and evanescent (imaginary) parts of the dispersion characteristics are shown in dispersion graph of figure 4.2.

Plates can be considered as rectangular waveguides of finite width and infinite thickness. In this manner, Lamb waves can be considered as vibration modes of a rectangular microstructure with infinite length and plane-strain boundary condition in thickness direction. MEMS resonators, however, are usually implemented on substrates with finite thickness. Thus, neglecting the finite length of a rectangular parallelepiped, the difference between in-plane modes of a silicon bar with Lamb modes comprises mainly from different boundary condition in thickness direction. In other words, MEMS resonators are closer to plane-stress boundary condition rather than plane-strain. Furthermore, as thickness of the microstructure increases, the frequency of symmetric resonance modes with out-of-plane polarization approaches to in-plane symmetric modes. Considering the possibility of coupling these modes together through finite Poisson's ratio, not only new dispersion branches are created in the case of rectangular wave-guide (considering infinite length for the microstructure) with close frequencies to in-plane modes, but in-plane dispersion branches will get affected. Figure 4.3(a) compares the dispersion characteristics of silicon plate of figure 4.2 with a rectangular waveguide with similar width and crystallographic orientation, but with finite thickness of 20μm. Large number of additional dispersion curves in frequency range of 140-220 MHz corresponds to guided waves with thickness-oriented particle polarization. Figure 4.3 (b) shows the zoomed-in view of the dispersion characteristic of first width-extensional and second width-shear modes for plate and rectangular waveguides.

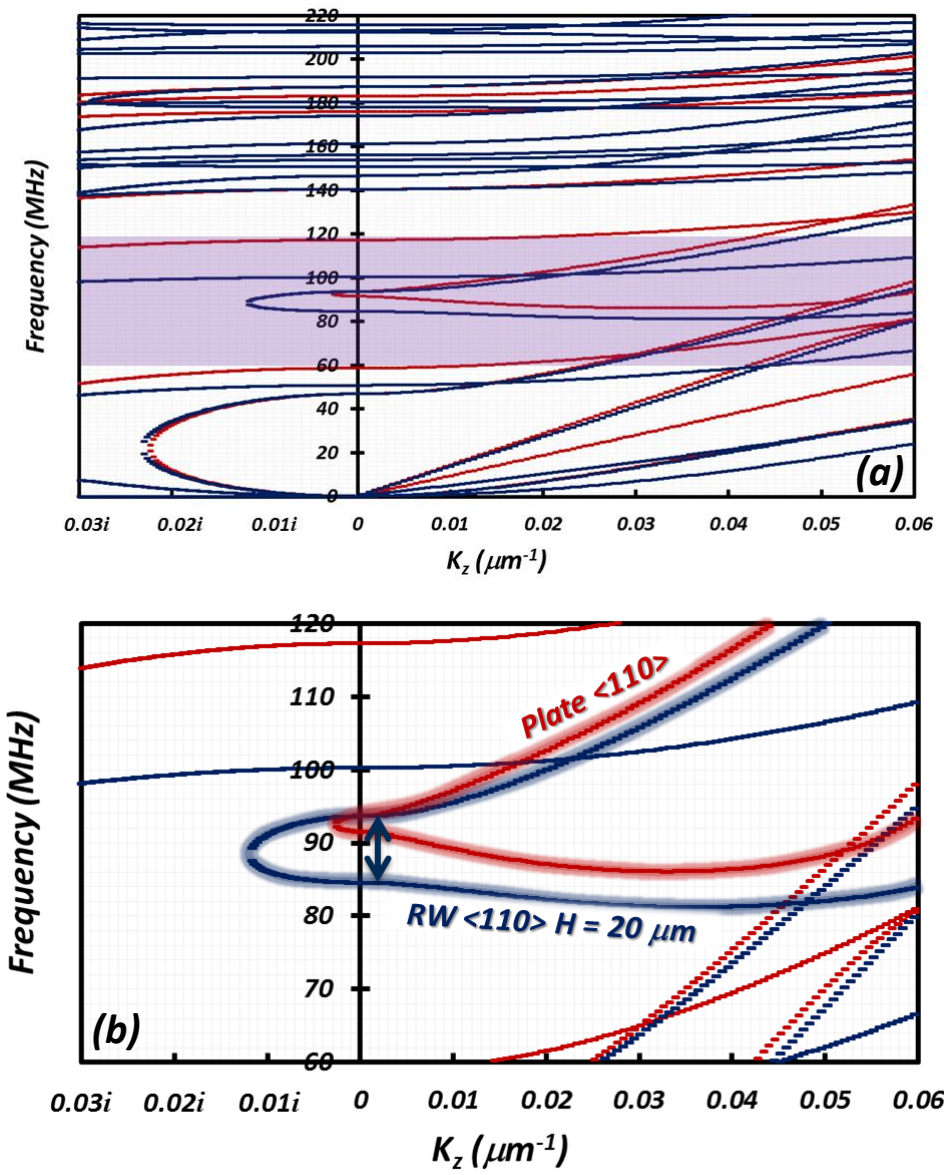

Figure 4.3: Dispersion characteristics of 50μm wide SCS waveguides of infinite thickness (plate) and finite thickness (20μm) for <110> propagation direction in (100) plate.

While the second width-shear branch of the rectangular wave guide remains close to that of plate, the change in the boundary condition in thickness direction has resulted in the width-extensional branch to be shifted to lower frequencies. This is due to the possibility of coupling of extensional strain/stress fields between width a thickness direction. Such a coupling does not exist in shear fields. Specifically, for the case of pure shear Lamb mode (K=0 of the second width-shear branch in figure 4.3 (b)), the frequency

remains unchanged between plate and rectangular waveguide cases. The large evanescent band between width-extensional and width-shear branches, created in the case of rectangular waveguide can be used for acoustic engineering of the microstructure geometry to efficiently trap acoustic energy.

Being anisotropic in (100) planes, silicon wave guides can show radically different dispersion characteristics if oriented in different directions. Figure 4.4 compares the dispersion characteristics of WE_1 and WS_2 branches of the waveguides in <110> and <100> crystallographic directions.

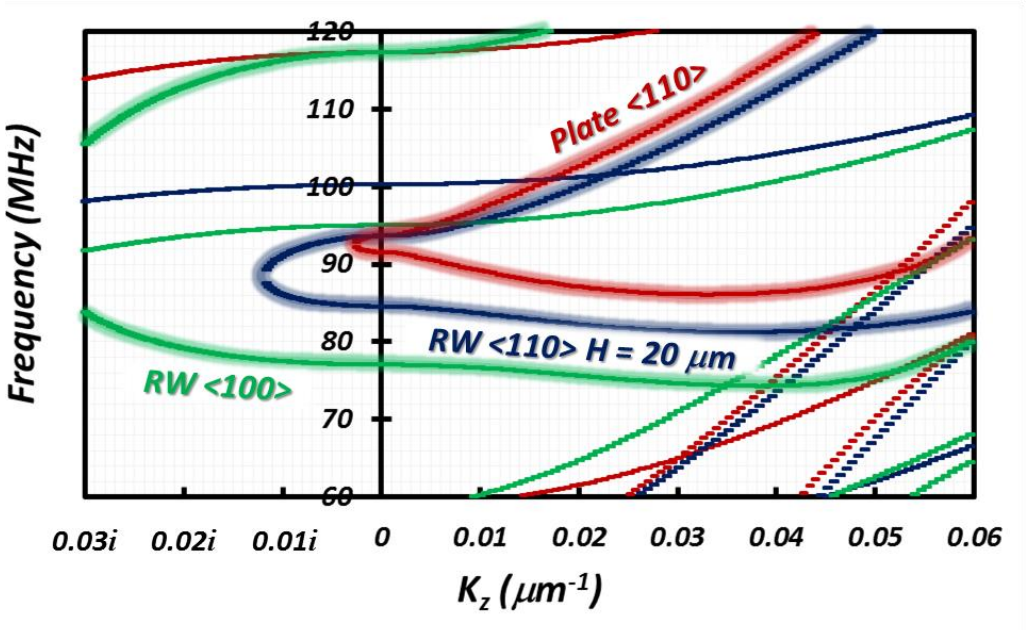

Figure 4.4: Dispersion characteristics of first width-extensional and second width-shear modes for rectangular waveguides of 50mm width and 20mm thickness, oriented in <110> and <100> crystallographic direction of (100) plane.

Although dispersion characteristics of rectangular wave-guides accounts for the finite thickness of the microstructures, however in practical cases, rectangular parallelepiped microstructures are finite in length, as well as width and thickness. Treating rectangular bar silicon resonators as acoustic waveguides with finite length (if this can be considered even an approximately valid assumption), can be very helpful in

analysis and design of resonators. In such treatment, several resonance modes of SiBARs can be attributed to the guided waves of an infinitely long waveguide; thus facilitating a qualitative study of the resonance modes of the microstructure using dispersion characteristics of guided waves in rectangular acoustic waveguides [41]. Figure 4.5 shows the resonance frequency of several modes of a rectangular microstructure with finite length (considering the length of the resonator as $\lambda/2$), on top of the dispersion characteristics of guided modes with similar shape propagating in infinitely long waveguide.

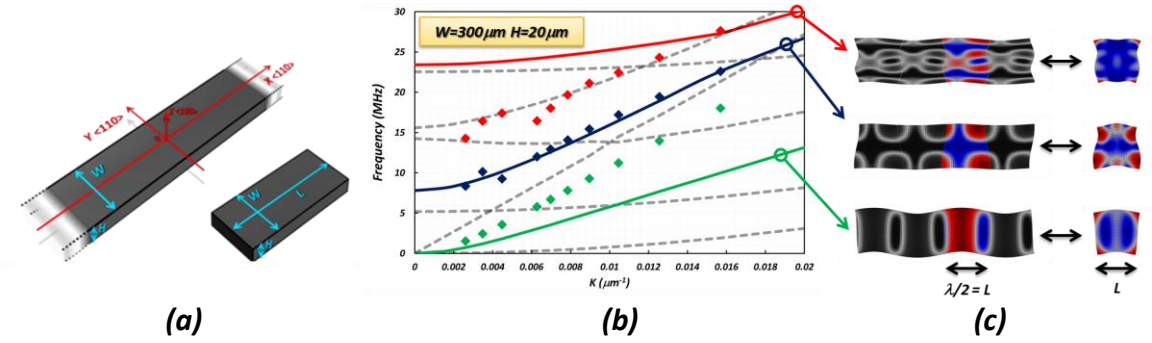

Figure 4.5: (a) Acoustic waveguide and rectangular resonator aligned with X-axis. (b) Dispersion curves of a silicon acoustic waveguide aligned to <110> direction of the (100) plane with characteristic width of 300μm and thickness of 20μm. (c) Lamb mode shapes with similar wavelength in the waveguide and their corresponding resonance mode shapes in square resonator.

It can be observed that the resonance frequencies of the modes are not following the dispersion characteristics even although the mode shapes are very similar. This is due to the additional stress-free boundary condition in length direction in the case of microstructure. It can be concluded that considering SiBARs as waveguides with finite length is not accurate unless the length can become virtually infinite. In such case, dispersion characteristics of the guided modes can be a very powerful tool to accurately designing the vibration mode of the microstructure accurately. Furthermore, as it will be shown in the following sections of this chapter, temperature characteristics of different dispersion curves can be used to control the thermal behavior of the resonator.

Finally, considering the dispersion characteristic of each guided modes in silicon waveguides as a function of its width (*W*) as well as thickness (*H*), the frequency of in-plane modes can be mainly controlled by the width and relatively independent from the thickness of the waveguide. However, for out-of-plane, either flexural or extensional/shear modes, the frequency is mainly defined by thickness. TPOS platforms facilitate implementation of waveguide on substrate with a thick layer of SCS, thus providing the opportunity to control the frequency of out-of-plane modes to be close to in-plane modes or their integer multiplication. Also, the dispersion curves of in-plane modes can be tuned by slight variation of waveguide width. This facilitates the coupling of different in-plane guided waves with different wavelengths through proper engineering of waveguide width across its length. While similar acoustic engineering has been previously used in FBARs [42] to suppress Lamb spurious modes and also increase coupling coefficient of piezoelectric transduction through trapping thickness extensional bulk mode in the central part of the device, unique features of TPOS provide exceptional opportunities to exploit this technique in a broader manner and for several novel applications. These applications include spurious suppression, *Q* and electromechanical coupling enhancement and TCF engineering. A proper design exploiting all these features in a single micro-structure can transform a resonator from a simple frequency reference into a monolithic, multi-port and complex component with a considerable engineering flexibility.

4.3 TETHERLESS ACOUSTICALLY-ENGINEERED HIGH-Q RESONATORS

A conventional high-frequency silicon resonator, designed to operate in first width-extensional bulk acoustic mode (hence the name SiBAR), can be considered as a

waveguide with characteristic width and height (*W* and *H*), doubly terminated in length direction with stress-free boundaries. Although the simple anchoring of such structure through two narrow tethers placed along the central nodal axis of the WE_1 mode results in the least acoustic energy leakage to the substrate and a high *Q* for WE_1 mode, it can provide the similar energy trapping for any other resonance mode with symmetric particle polarization with respect to nodal axis. This suggests several spurious modes initiated from different symmetric quasi-Lamb branches of the dispersion characteristic of waveguide can be trapped in the acoustic cavity and efficiently excited by the same transduction scheme. Although extension of electromechanical transducer across device length can considerably suppress several of these spurs initiated by Lamb mode with large wavenumbers and through charge cancellation, all modes generated from waves with $\lambda = \infty$ or L/2 can be efficiently transduced and stay problematic. Such modes are usually suppressed in frequency reference applications by employing CMOS filtering in the interface loop used for oscillator implementation. Furthermore, for the majority of vibration modes, no ideal nodal point exists and considering finite width of supporting tethers used to anchor the microstructure, the acoustic behavior of the device will get affected in presence of narrow tethers, thus resulting in energy leakage into the surrounding substrate. Finally, further scaling down of resonator dimensions for realization of devices operating in UHF regime requires ultra-narrow tethers which cannot be realized using conventional optical lithography. This section introduces a novel technique to synthesize bulk acoustic resonance modes with mechanical energy trapped in the central region of the acoustic cavity thus resulting in a quasi-levitating microstructure. Energy concentration in central part and far from device peripheral faces

along its length inherently eliminates energy leakage into the substrate and consequently obviates the need for narrow tethers to anchor the device. Monolithic connection of these faces to the substrate removes two stress-free boundaries of the microstructure which can potentially result in several spurious modes resulted from reflection of acoustic waves at solid/air interfaces along device length.

Several acoustic waveguides with different dimensions and subsequently different dispersion characteristics can be coupled together by cascading them in series along their length direction to form a geometrically engineered microstructure. A vibration mode of such a microstructure may exist, emerging from acoustic coupling of propagating or evanescent guided wave solutions in constituent waveguides, if the continuity of particle displacement and stress holds at transition interfaces. This can be used to trap a propagating mode in an active region by coupling it into evanescent modes in the waveguides surrounding it. Furthermore, the propagation of the guided waves in length direction can be ideally blocked if no solution, either propagating or evanescent, exists at propagation frequency. This can be used to realize ideal clamping as opposed to non-ideal anchoring to the substrate which may not practically represent a rigid anchoring platform.

Geometrical engineering of the waveguide width across its length has been used to couple three waveguides to form a synthetic resonance modes with acoustic energy trapped in the central region of the microstructure. Figure 4.6 shows the SEM picture of such microstructure connected to the substrate using narrow tethers.

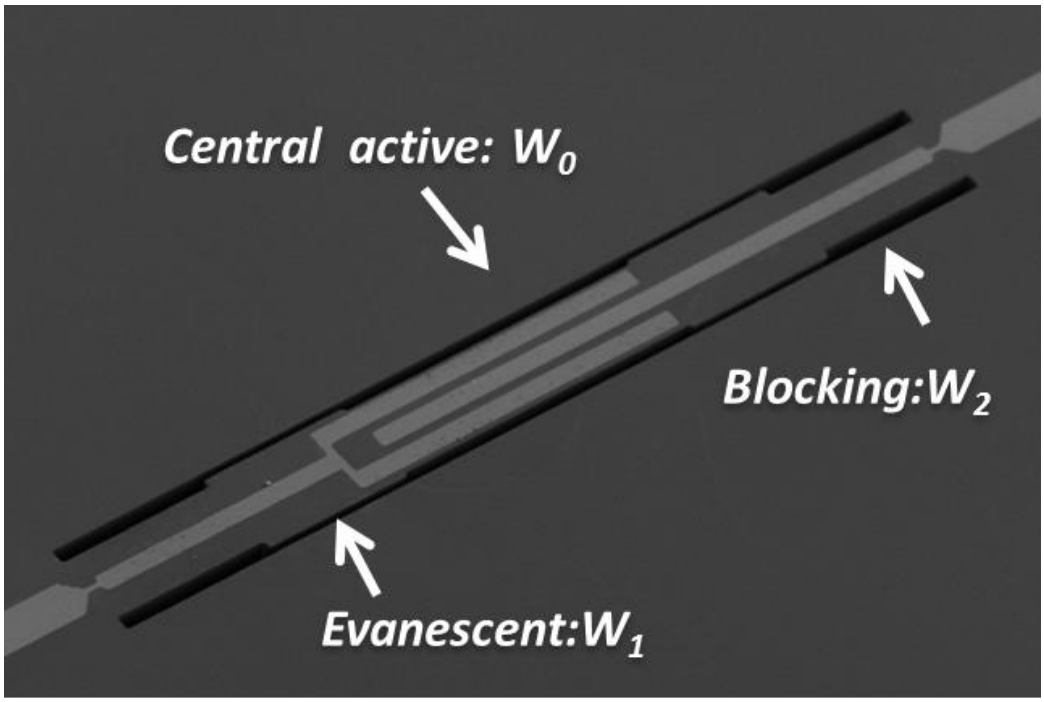

Figure 4.6: The SEM view of the acoustically engineered waveguide anchored to the substrate through peripheral faces along its length.

Figure 4.7 shows the dispersion characteristics of WE_1 and WS_2 branches for three constituent waveguides of the microstructure in figure 4.6. The width of the intermediate (W_1) region is chosen so that only evanescent solutions exist for small K_x (i.e. guided modes close to plane width-extensional bulk acoustic mode). The width of flanks has been chosen so that the lowest frequency of a guided mode on WE_1 branch locates at a frequency higher than propagating WE_1 cut-off in central region (W_0). This guarantees blocking of the evanescent wave excited in the intermediate region through coupling to the propagating solution in central region. Figure 4.7 shows this concept on the dispersion diagram of the different regions schematically.

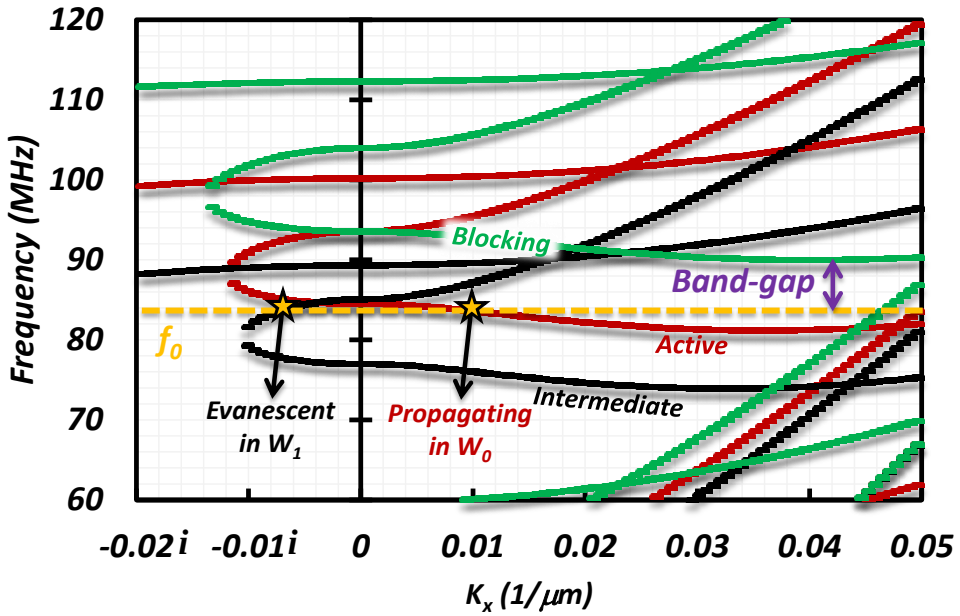

Figure 4.7: Dispersion characteristics of WE_1 and WS_2 modes for different waveguides forming the microstructure.

Figure 4.8 shows the mode synthesized mode shape of the resonator in figure 4.6. The acoustic energy is concentrated in the central region and the charge density decays as going towards the flanks.

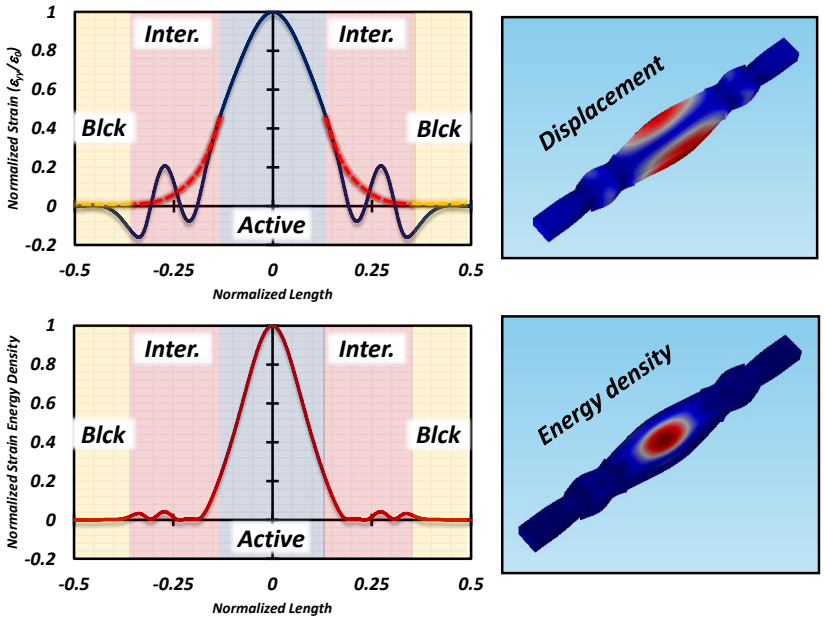

Figure 4.8: Displacement and energy density of the synthesized bulk acoustic mode. Energy density is maximum in the active region and vanishes in flanks.

Since the energy in blocking region is negligible, the peripheral face of the microstructure can be connected to the substrate without any concern for energy leakage of the synthesized mode. However, this is not the case for other modes with non-concentrated energy distribution across the length of the microstructure. Hence, facial clamping results in excessive suppression of these spurious modes. Figure 4.9 compares the large frequency responses of the tetherless microstructure with conventional tether-supported SiBARs.

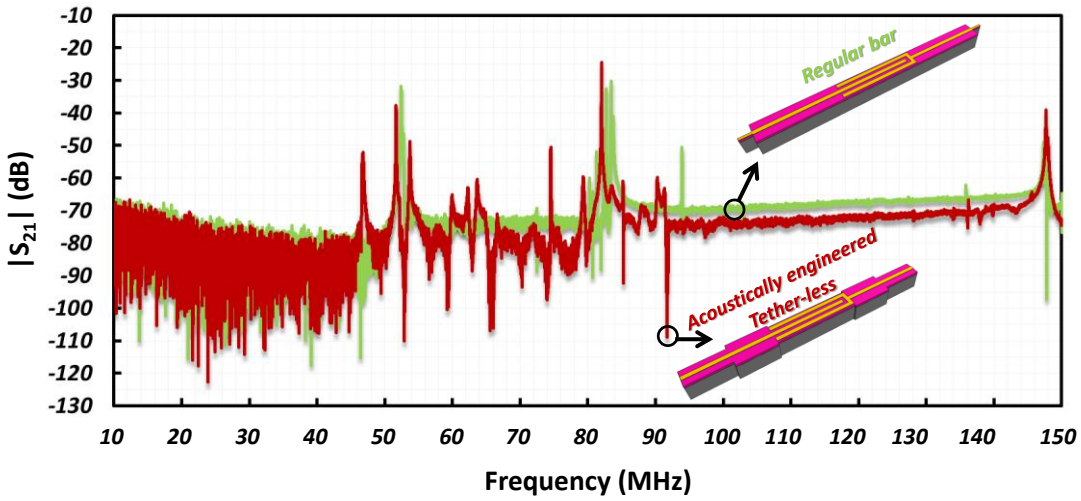

Figure 4.9: Measured large-span frequency response of the acoustically engineered tetherless resonator in comparison with a SiBAR anchored to the substrate through narrow tethers.

Efficient spurious suppression can be observed as a result of acoustic engineering of the microstructure, thus obviating narrow tether anchoring. Similar length and electrode configuration has been used for both microstructures.

Figure 4.10 shows the SEM picture of the devices with frequency responses shown in figure 4.9. In addition to these two resonators, another device is the case of acoustically engineered resonator connected to the substrate through narrow tethers.

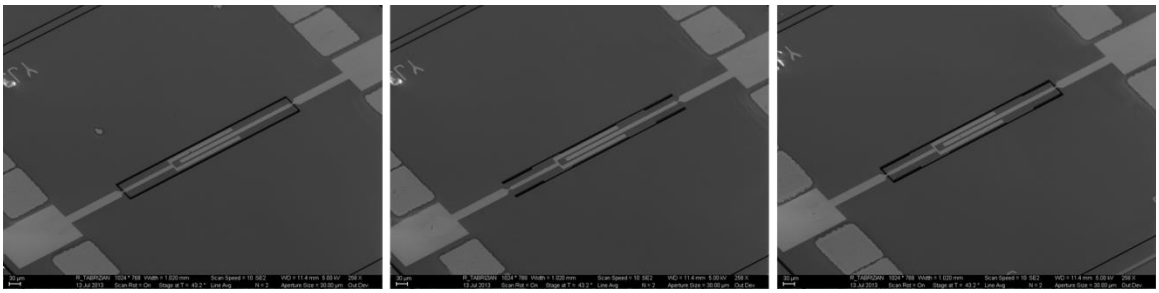

Figure 4.10: SEM image of the resonators with/without acoustic engineering of their width and anchored to the substrate with/without narrow tethers.

Figure 4.11 shows the frequency response of the devices in figure 4.10.

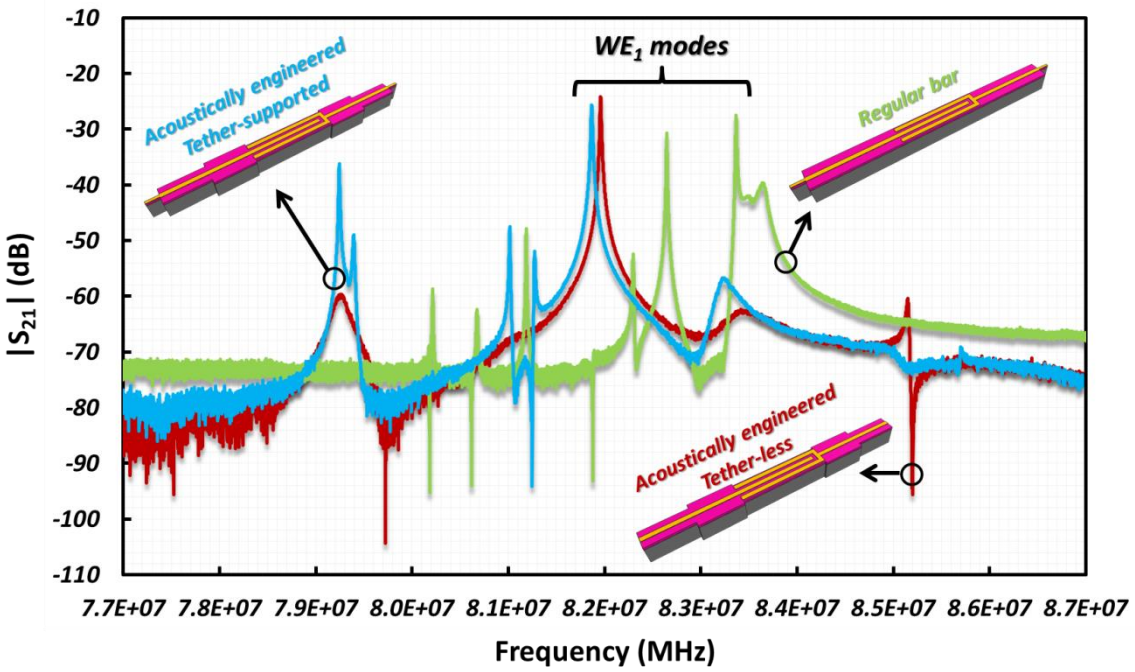

Figure 4.11: 10 MHz-span frequency response of three microresonators with similar piezoelectric transduction scheme: one simple SiBAR and two acoustically engineered w/o tethers.

While mere acoustic engineering is significantly suppressing the spurious modes in the close vicinity of the main resonance peak, it can generate new modes. These undesired spurs are suppressed when the tethers are removed and the acoustic cavity is monolithically connected through terminating faces to the substrate. The main mode remains unaffected since the energy is trapped in the central region and far from substrate.

In order to verify the effectiveness of each acoustic waveguide in forming energy trapped synthetic mode, devices consisting of only active region as well as structures with active and evanescent but without blocking has been implemented with similar dimensions of individual constituent waveguides and connected to the substrate without any tethers. Direct connection of the intermediate evanescent-supporting section to the substrate results in considerable energy leakage resulting from non-ideal fixed boundary provided by substrate. The intermediate region can be further extended in length to enhance the desirable attenuation of the evanescent wave and hence obviating the flanks; but costing increased form factor to the device. Figure 4.12 shows the SEM picture of the devices with removed flank, or removed flank as well as intermediate region in comparison with the acoustically engineered tetherless structure.

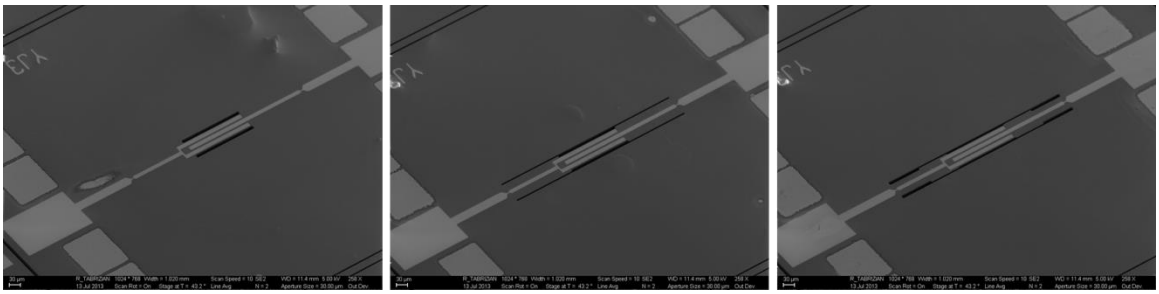

Figure 4.12: SEM image of the resonators without intermediate and flank (left), without flank (middle) and complete acoustically engineered tetherless structure (right).

Figure 4.13 compares short-span frequency response of cases with removed flank, or removed both intermediate and flank, with the complete microstructure, showing the importance of both intermediate and flank regions in efficient energy trapping of the WE_1 mode in the central region.

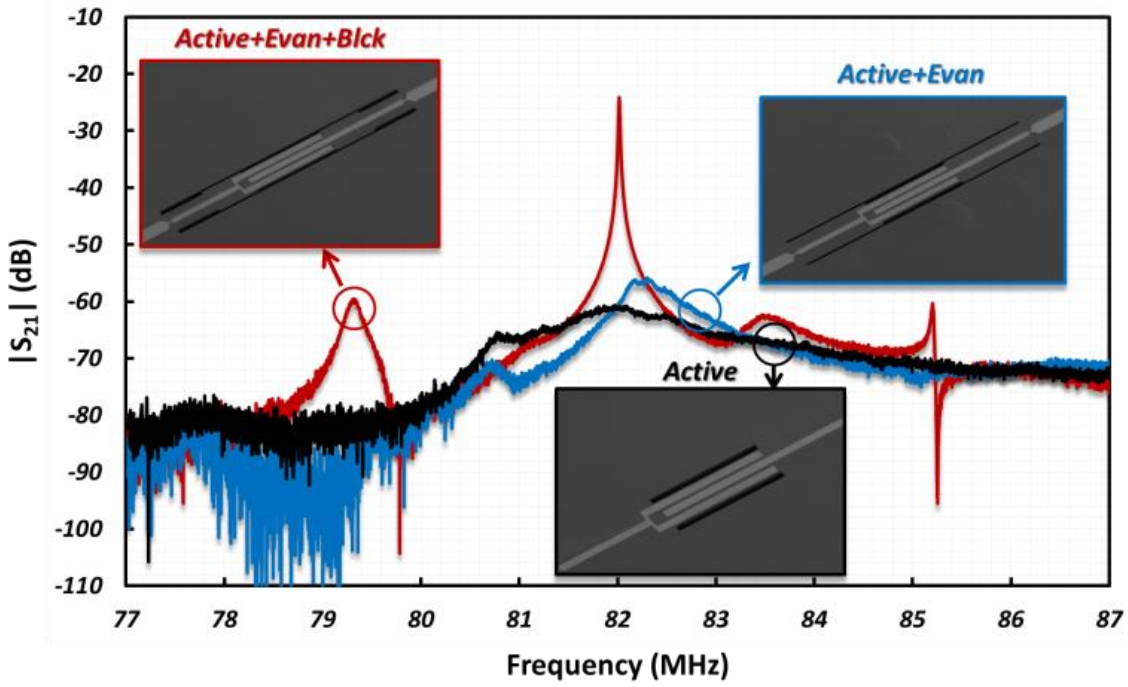

Figure 4.13: Short-span frequency responses of three microresonators with similar piezoelectric transduction scheme, but different acoustic termination: design 1 without flank and intermediate, design 2 without flank but with intermediate, and design 3 with both flank and intermediate sections. While WE_1 cannot be excited in design1, the anchoring of design 2 considerably suppress this mode due to non-ideal fixed boundary defined by the substrate. In design 3, ideal fixed boundary created acoustically by properly design flank forces the evanescent wave propagating in the intermediate region to be terminated, thus trapping the WE_1 mode in the central region.

4.4 SHEAR-EXTENSIONAL MIXED-MODE RESONATORS WITH HIGH-Q AND LOW-TCF

Acoustic engineering of the device through slight variation of waveguide width has been introduced in section 4.3 to provide efficient spurious suppression and eliminate the need for narrow tethers. In these structures, the synthesized resonance modes consist of different extensional Lamb waves, either propagating or evanescent, with different wavelengths coupled together. In this section, synthesized modes resulted from acoustic coupling of symmetric extensional and shear modes through evanescent supporting intermediate region will be introduced to provide considerable *Q* enhancement and TCF reduction compared to SiBARs operating in WE bulk modes.

Different Lamb modes propagating in silicon waveguides show different temperature characteristics. This is due to dissimilar temperature characteristics and contribution of different elastic constants of SCS contributing in dispersive behavior of propagating waves. Table 4.2 shows different temperature characteristics of elastic constants in native (non-doped) SCS.

Table 4.1: Native silicon elastic constants and their temperature coefficients

Elastic Coefficient	**Value at 25°C (GPa)**	**Temperature Coefficient (ppm°/C)**
C_{11}	166	67
C_{12}	64	99
C_{44}	80	44
$C'=(C_{11}-C_{12})/2$	51	47
$C''=(C_{11}+C_{12}+2C_{44})/2$	195	63

For silicon waveguides aligned to <110> crystallographic direction of SCS, shear-based branches are showing lower TCF compared to extensional modes. This is mainly due to higher contribution of low TCE quasi-shear elastic constant C' in shear modes, and high-TCD quasi-longitudinal elastic constant C" in extensional modes. Figure 4.14 compares the TCF of different first width-extensional and second width-shear branches as a function of wavenumber for waveguide implemented in native SCS.

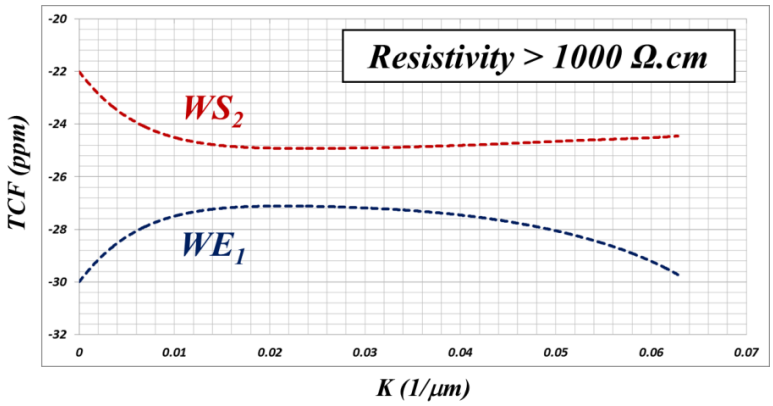

Figure 4.14: TCF of WE_1 and WS_2 branches as a function of wavenumber, in native SCS, showing a considerable difference between their TCF.

This results in TCF variation of different resonance modes in SiBAR (Figure 4.15).

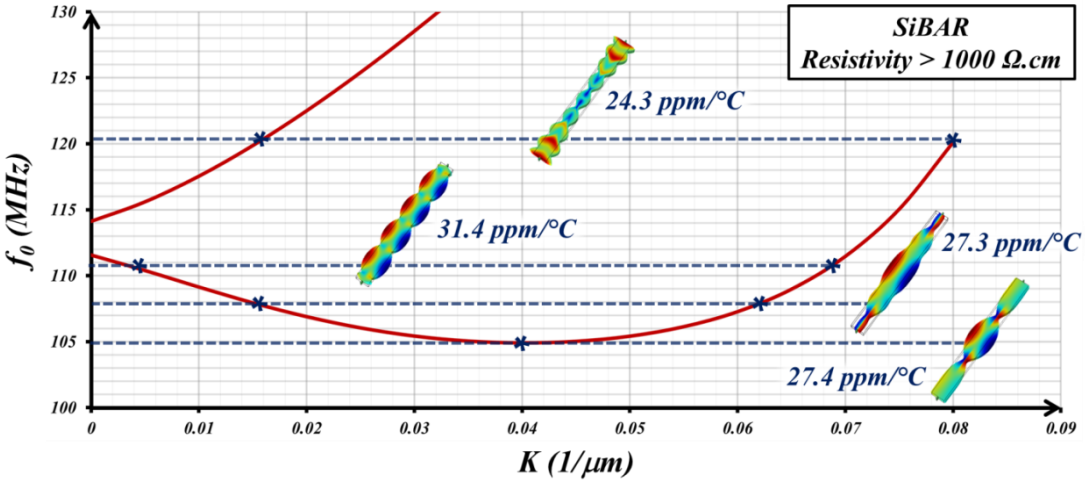

Figure 4.15: The mode shape of different resonance modes of a SiBAR and their constituent Lamb waves. Dissimilar TCF of the modes can be explained as a result of different temperature characteristics of lamb modes with different wavenumbers.

The TCE of SCS different elastic constants can be further reduced by doping the substrate. Figure 4.16 compares the TCF of WE_1 and WS_2 branches for a waveguide implemented in a highly doped SCS substrate.

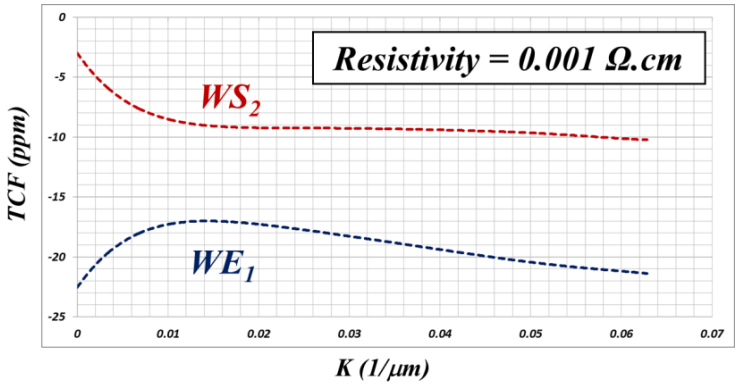

Figure 4.16: TCF of WE_1 and WS_2 branches as a function of wavenumber, in low resistivity SCS, showing a considerable reduction in TCF of both branches.WS_2 branch shows a TCF smaller (in absolute value) than -5 ppm/°C suggesting implementation of temperature stable oscillators using shear mode resonators implemented in highly doped SCS.

Lower TCF of shear Lamb waves suggests implementation of shear-mode resonators instead of extensional mode. However, while electrostatic transduction can only provide normal (rather than shear) forces across the capacitive gap, thin

piezoelectric films are polycrystalline; thus lacking efficient d_{15} (shear) piezoelectric coefficient. This section introduces a novel group of acoustically-engineered micro-structures which provides a unique way of excitation of shear Lamb waves in silicon waveguides using piezoelectric or capacitive transducers. In these devices, which will be called mixed-mode hereafter, the resonance mode is synthesized by coupling an extensional lamb mode with a symmetric shear mode through evanescent waves. Figure 4.17 shows the SEM picture of a mixed-mode resonator implemented in TPOS platform.

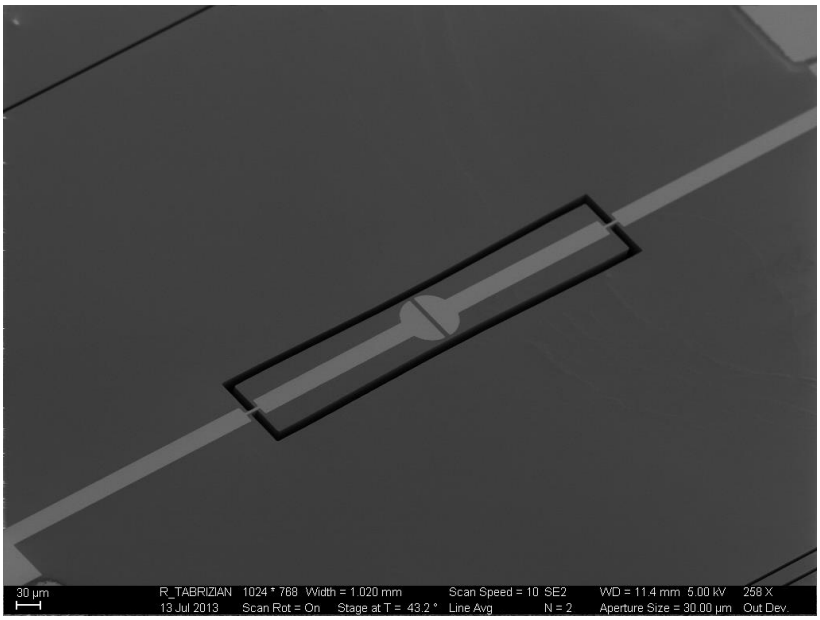

Figure 4.17: SEM image of a mixed-mode resonator implemented on TPOS platform.

Figure 4.18 shows the shear-extensional mode shape of the device. Large shear acoustic fields excited in this mode can be clearly observed.

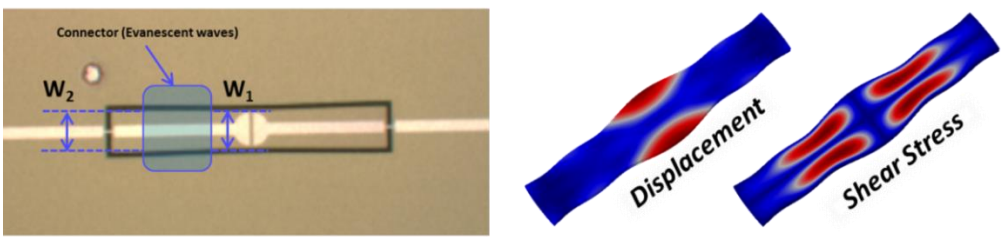

Figure 4.18: Optical image of a mixed-mode resonator implemented on TPOS platform and displacement and shear stress fields of the mixed shear-extensional mode.

Figure 4.19 shows the dispersion curves corresponding to central part (supporting WE_1) and flanks (supporting WS_2) of the microstructure.

Considering Figure 4.16, shear branch with the smallest wavenumber (k=0) shows the lowest TCF. Hence, in order to have the best TCF performance, the flanks are designed to support the WS_2 with infinitely large wavelength (i.e. k=0) and lowest TCF at the same frequency of bulk WE_1 wave in the narrower central part. This is shown in dispersion characteristic of figure 4.19.

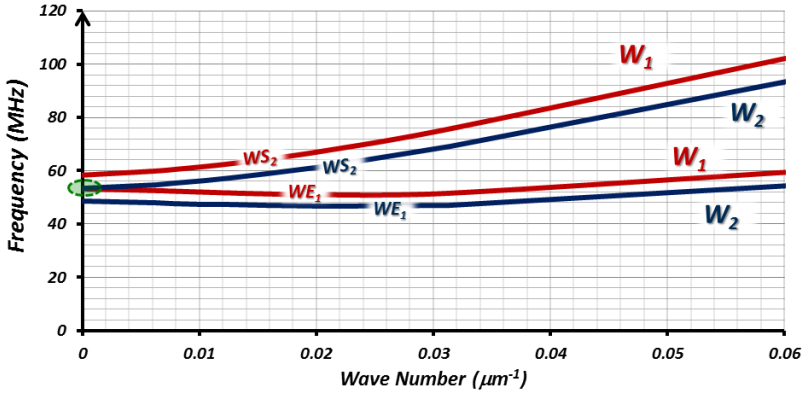

Figure 4.19: Dispersion characteristics of central part with W_1 width (red) and flanks with W_2 width (blue), designed to have WE_1 of the central part coincide with WS_2 of the flanks at the mixed shear-extensional resonance mode.

The flank to central width ratio can be calculated based on acoustic velocity of quasi-bulk longitudinal and shear waves propagating in width direction of the waveguide. For <110> oriented waveguide this ratio can be written based on elastic coefficients of SCS:

$$\frac{W_2}{W_1} = \left(\frac{4(c_{11}-c_{12})}{c_{11}+c_{12}+2c_{44}}\right)^2 \qquad (4.5)$$

Implementing such a mixed-mode facilitate excitation of shear waves in flanks using piezoelectric transducer: the WE_1 Lamb mode can be excited using d_{31} piezoelectric transduction in the small central part (where electrodes are placed in figure

4.17) and coupled to the WS_2 in flanks through connector regions (which support evanescent waves). Figure 4.20 shows the frequency response of the device shown in figure 4.17.

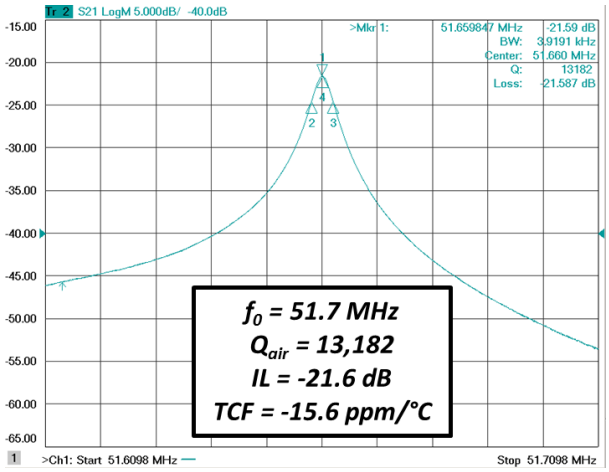

Figure 4.20: Short-span frequency response of the mixed-mode resonator showing very high-Q and an improved TCF of -15.6 ppm/°C (compared to WE1 TCF of -21 ppm/°C in SiBARs implemented in the same batch).

4.5 ACOUSTICALLY-ENGINEERED MULTIPORT RESONATORS FOR ACCURATE TEMPERATURE SENSING

This section introduces a novel silicon microresonator that is acoustically engineered to facilitate independent piezoelectric transduction of multiple energy-trapped high-*Q* resonance modes with large TCF difference and integer frequency ratios, while suppressing other spurious modes. Acoustic energy trapping in the central part of the resonator and far from the substrate obviates the need for narrow support tethers, facilitating integration of several isolated metallic electrodes on the thin-film piezoelectric transducer that are freely routed through wide anchors of the microstructure towards separate electrical ports. This enables the implementation of multiple electrically isolated oscillators using a single resonator, which can be used to generate small beat frequency with very high temperature sensitivity from an integer linear combination of

multiple energy-trapped modes. Such a beat frequency can be used to provide accurate device-level temperature sensing.

Silicon frequency references are moving towards products aiming at temperature-compensated and oven-controlled quartz crystal oscillator (TCXO and OCXO) markets. Given the large temperature sensitivity of silicon resonators compared to their quartz crystal counterparts, realization of high frequency stabilities over a large temperature range requires highly accurate continuous temperature monitoring of the device to apply proper pulling and/or temperature control to compensate temperature-induced frequency drifts. While accurate CMOS temperature sensing solutions impose excessive power consumption and complexity, being physically separate and consequently thermally isolated from the micromechanical frequency reference make these techniques prone to offset and delay in temperature monitoring of the device which can result in frequency drifts exceeding the instability tolerance. Hence, device-level temperature sensing is desirable. Dual-mode quartz crystal and MEMS resonant temperature sensors have been designed and implemented using a higher tone of the main resonance mode along with the first tone to generate a small beat frequency with large temperature sensitivity. However, these techniques are very limited by the small TCF variation of different tones of a resonance mode. Furthermore, similar particle polarization and/or common electrical transduction ports used for excitation and sensing of both modes may result in destructive mechanical and/or electrical interference when device operates in two oscillation loops simultaneously. In this section we introduce a new class of microresonators, which possess linearly independent resonance modes with integer frequency ratios, and large TCF difference. The novel tether-less architecture of these rigidly/facially anchored

piezoelectrically transduced resonators provides versatile electrode routing, facilitating independent transduction of multiple modes through electrically isolated ports. This substantially eliminates any potential destructive electrical loading between several oscillator-loops interfaced with the device.

Acoustic engineering of the device in-plane geometry based on unique dispersion characteristics of guided modes in SCS wave-guides can be used to provide efficient energy trapping for several, rather than one, in-plane and out-of-plane modes.

These energy trapped modes can be categorized in two groups, based on the dispersion behavior of the guided wave forming the resonance mode. In the first group, which was explained in detail in section 4.3, the resonator body consists of an active region surrounded by evanescent and blocking extensions. In this group, since the frequency of the evanescent portion of the corresponding dispersion branch is higher than propagating portion around K=0 (dispersion type I), an increase in the width of the waveguide results in acoustic coupling of propagating wave in central region to evanescent wave in intermediate region. However, different dispersion branches may show an opposite trend around K=0. In these branches, the frequency of the evanescent portions is lower than propagating mode in close vicinity of K=0 (dispersion type II). For a rectangular waveguide, even dispersion branches of different tones of the same mode may belong to different dispersion types. Figure 4.21 shows the dispersion characteristics of first and third width-extensional modes of a rectangular waveguide with 114μm width and 20μm thickness, oriented in <100> and <110> directions of a (100) plane.

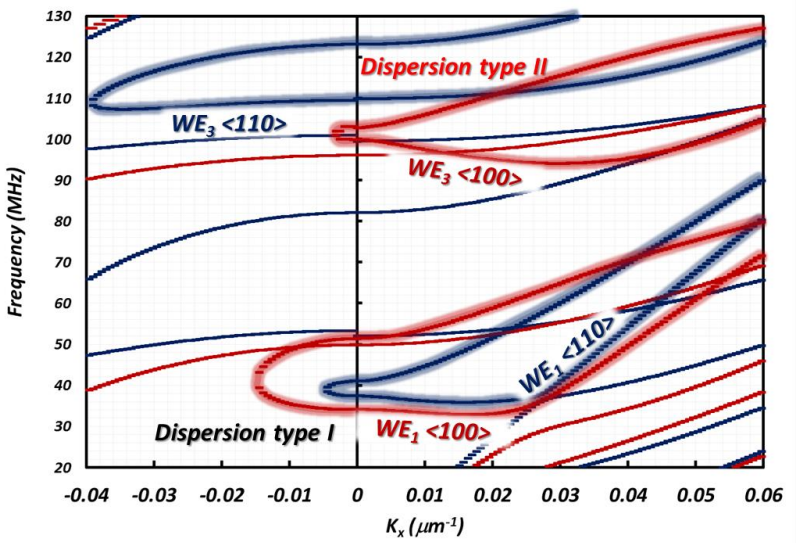

Figure 4.21: Dispersion characteristics of 1st and 3rd width-extensional modes of a rectangular waveguide with 114μm width and 20μm thickness oriented in <100> and <110> directions of a (100) plane. For <100> orientation, both WE_1 and WE_3 show dispersion type I. However for <110> orientation, while WE_1 shows dispersion type I, WE_3 shows type II behavior.

Different dispersion characteristic of type II can be used to trap the quasi-plane bulk acoustic mode (K=0) in the central region of the acoustically-engineered waveguide. Figure 4.22 shows the microstructure acoustically engineered for this purpose.

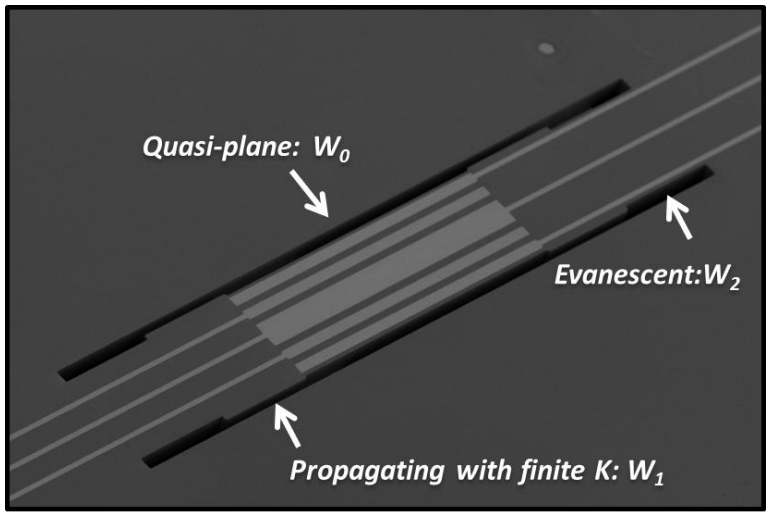

Figure 4.22: Acoustically-engineered waveguide designed for energy trapping of the 3rd width-extensional quasi-plane mode in the central region of the microstructure.

Figure 4.23 shows the dispersion characteristics of constituent waveguides of the microstructure of figure 4.22 as well as the resonance mode shape.

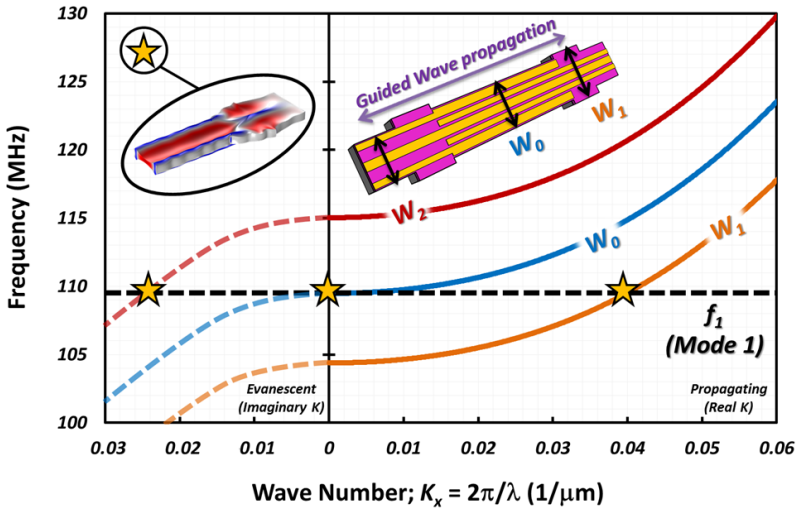

Figure 4.23: Dispersion characteristics of WE_3 mode for constituent waveguides of the resonator. The inset shows the displacement mode-shape of the half-resonator.

The resonance mode of the device is formed from acoustic coupling of the quasi-plane wave (K=0) in central region with the propagating wave of finite K in intermediate region and finally the evanescent wave propagating in flanks. This results in a piston shaped displacement of the structure in its central region during resonance.

Figure 4.24 shows the normalized charge density in central electrode region for the piston mode.

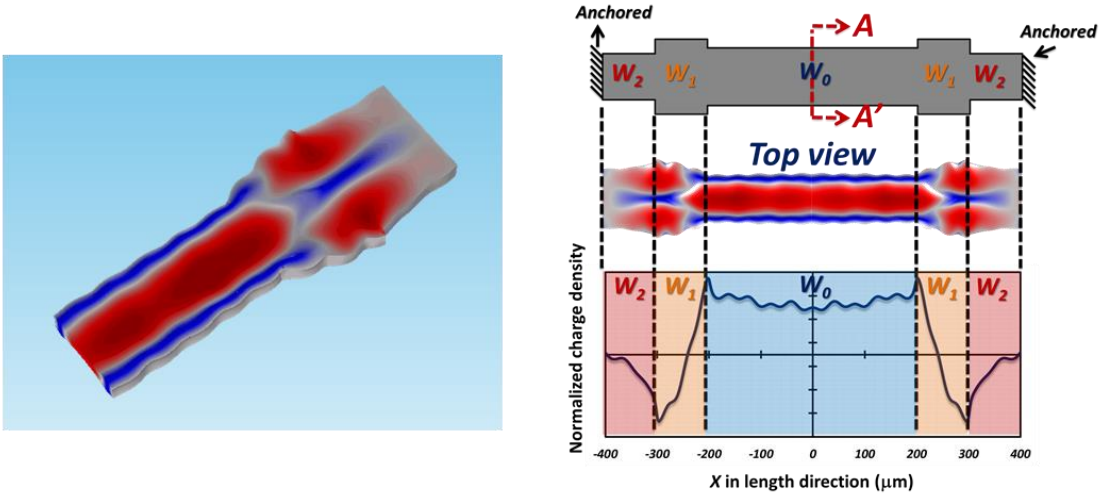

Figure 4.24: The mode shape of the piston mode (left) and the normalized charge density in the central electrode region of the resonator (figure 4.22).

Besides piston mode, acoustic engineering of the device results in other energy trapped modes. The wide anchoring regions provided by tetherless structure of the resonator facilitate simultaneous transduction of several of these modes through electrically isolated ports. Figure 4.25 compares dispersion characteristics and electrical charge density of the in-plane piston mode with an energy-trapped symmetric out-of-plane mode.

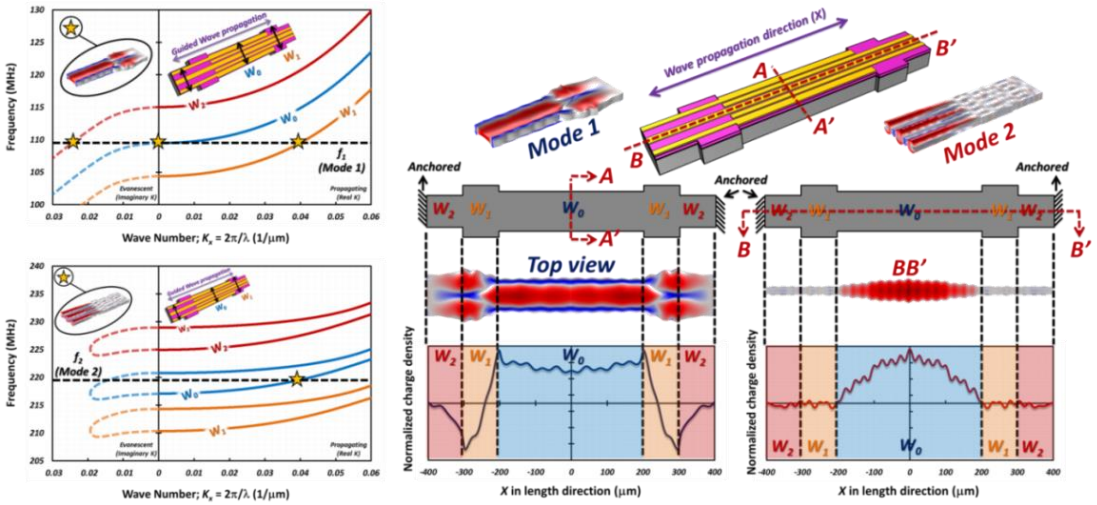

Figure 4.25: (a) Dispersion curves for guided waves resulting in modes 1(in-plane) and 2 (out-of-plane). In mode 1, the 3rd width-extensional bulk acoustic mode ($K_x = 0$) in the central region (W_0) is coupled to the evanescent wave in flanks (W_2) through intermediate regions (W_1); therefore resulting in acoustic energy trapping in the central part of the device. In mode 2, the symmetric out-of-plane wave in the central region (W_0) is not supported in the flanks; thus imposing ideally-clamped (as opposed to non-ideal clamping/anchoring of the cavity to the substrate) boundary condition at the two ends of the central region and prevents energy leakage to the substrate. (b) Simulated mode shape (AA' cross section) and normalized charge density for the two resonance modes (over the BB' crossing line) showing the effect of acoustic engineering on energy-trapping in the central region.

Since several transduction ports can be integrated with the device, multiple oscillators can be made using a single resonator operating in different modes as frequency references. Figure 4.26 shows the general architecture of a dual-mode oscillator.

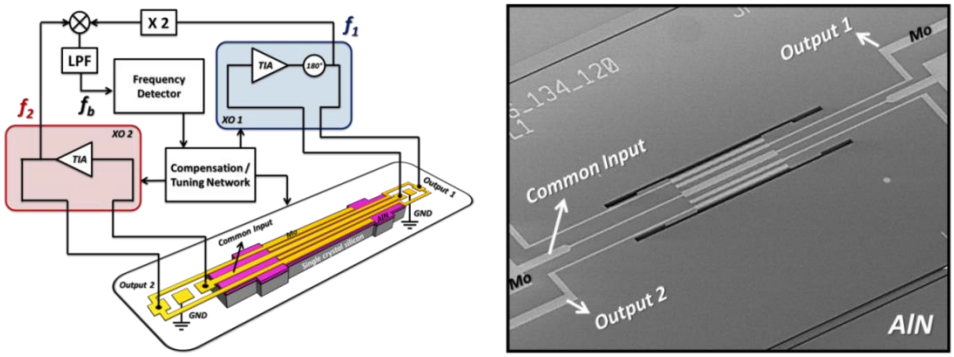

Figure 4.26: (a) The general architecture for a temperature stable dual-mode oscillator, which can be used in TCXO/ OCXO/MCXO configuration exploiting self-temperature sensing through beat frequency. (b) SEM image of the single-input double-output AlN-on-silicon resonator implemented on low resistivity substrate showing the geometry engineered to trap acoustic energy in the central part, thus facilitating wide anchoring of the device to the substrate. Multiple electrodes are freely routed through the wide support towards electrically isolated ports.

Furthermore, by opting for proper substrate thickness, energy-trapped out-of-plane resonant modes with integer-fold frequencies of any in-plane extensional piston mode can be efficiently excited, some of them showing very large TCF difference when the device is implemented in ultra-low resistivity (100) silicon substrates and aligned to <110> crystallographic direction. This is a result of dissimilar temperature characteristics of different stiffness coefficients of SCS. Having integer frequency ratios and large TCF difference, a beat frequency with very high temperature sensitivity can be generated from an integer (rather than fractional) linear combination of multiple of these modes using a simple architecture (Figure 4.26a) without introduction of excessive complexity and noise. Figure 4.26b shows the SEM image of a three port resonator (single-input double-output) , acoustically engineered to have two energy-trapped modes, among others, at 109 MHz (in-plane mode 1) and 218 MHz (out-of-plane mode 2) with *Q*s of 2,600 and 4,000 (measured in air) respectively (Figure 4.27).

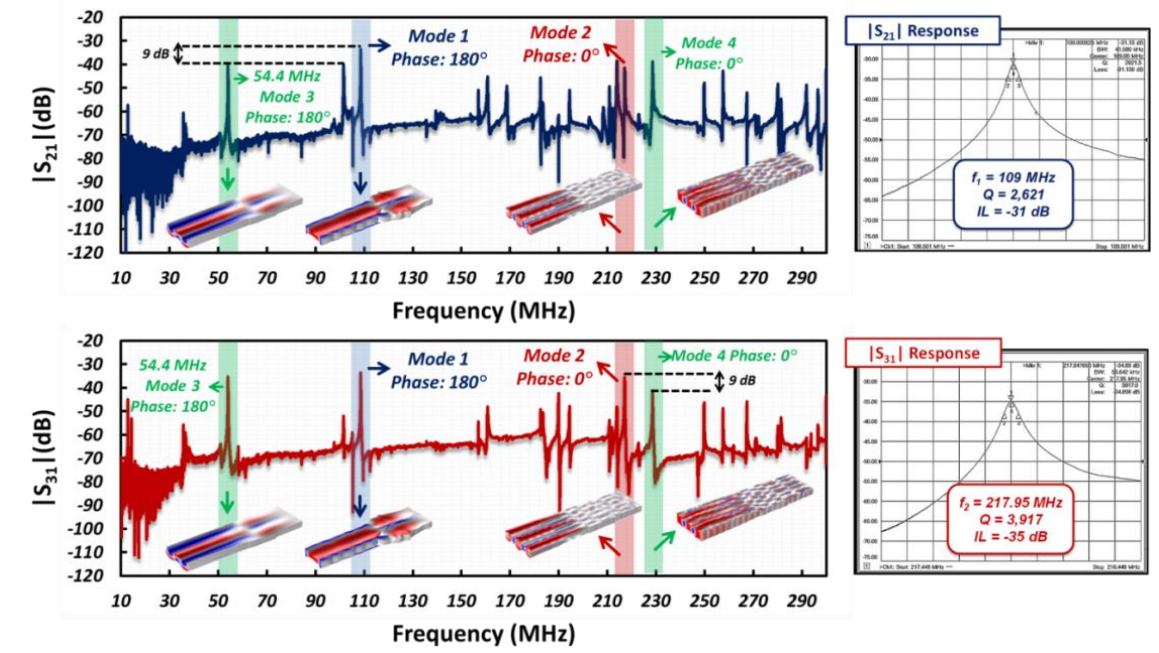

Figure 4.27: Measured large-span (left) and short-span screen-shot (right) of the frequency response for S_{21} and S_{31}. Energy-trapped modes including mode 1 and 2 used to generate beat frequency, are highlighted in the large-span frequency response. Efficient spurious suppression in addition to proper electrode configuration resulting in 180° phase-difference at two modes facilitate implementation of separate oscillators for modes 1 and 2, without any concern about locking in to spurs or one another.

The acoustic engineering as well as proper electrode configuration exploited in the device have resulted in efficient transduction of energy-trapped modes 1 and 2, while considerably suppressing other modes to > 9dB higher insertion-loss levels. Figure 4.28 shows the temperature characteristics of the modes.

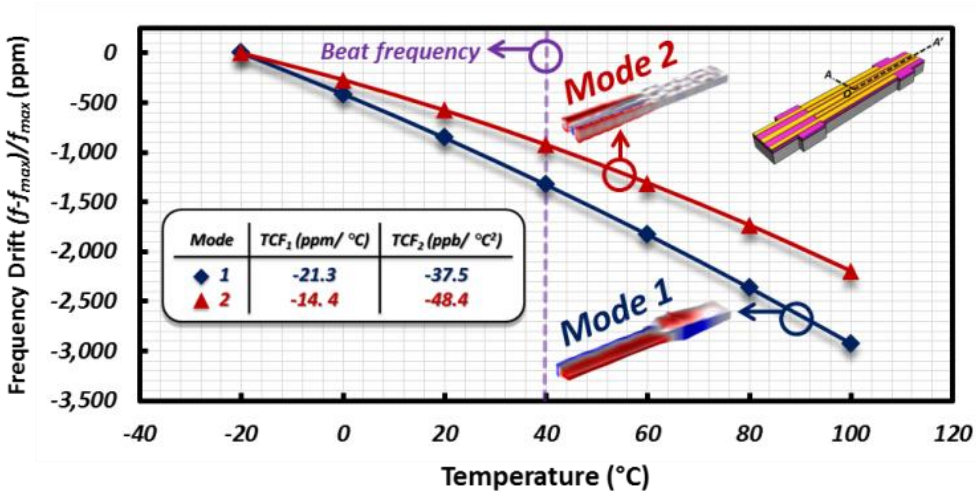

Figure 4.28: Measured temperature characteristics of the resonance frequency for modes 1 and 2 showing ~7 ppm/°C TCF_1 difference between them.

A linear TCF (TCF_1) of -21.3 ppm/°C and -14.4 ppm/°C have been measured for in-plane mode 1 and out-of-plane mode 2 respectively showing a large difference of ~7 ppm/°C. The beat frequency extracted from the modes ($f_b=f_2-2f_1$) shows a linear temperature characteristic with a TCF of ~8300 ppm/°C (Figure 4.29). This is the highest temperature sensitivity reported to date for any single-device dual-mode resonant temperature sensor with integer linear combination coefficients.

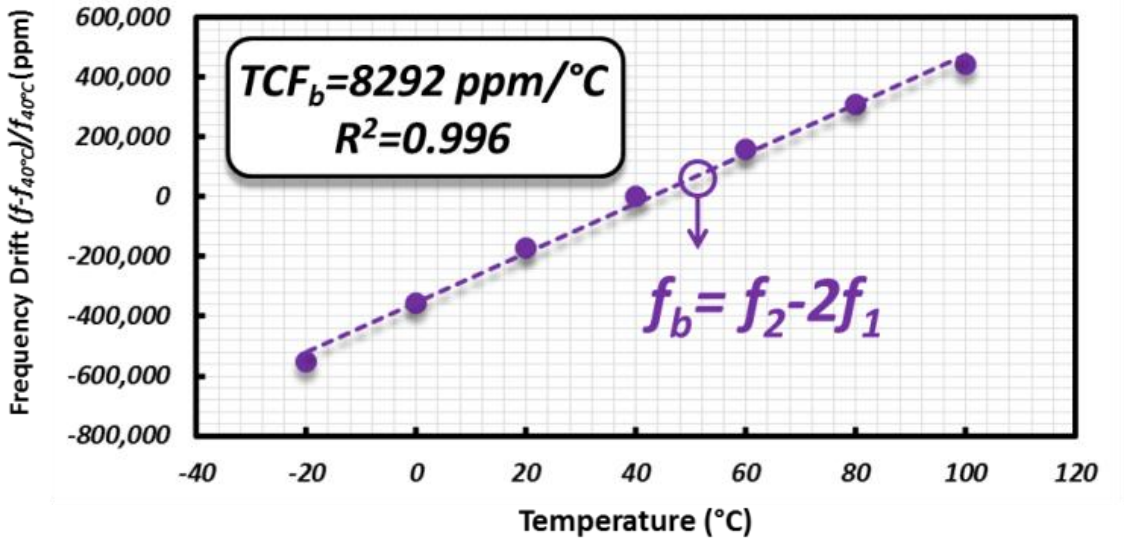

Figure 4.29: Temperature characteristic of the beat frequency extracted from integer linear combination of modes 1 and 2.

Although the large sensitivity of the beat frequency may be affected by process uncertainties such as substrate thickness variation, linear combination of three energy-trapped modes (rather than two) can be used to considerably compensate for beat frequency value and temperature sensitivity drifts. This can be realized thanks to opposite trend of thickness-dependency for extensional and flexural out-of-plane energy-trapped modes (modes 2 and 3 in Figure 4.30).

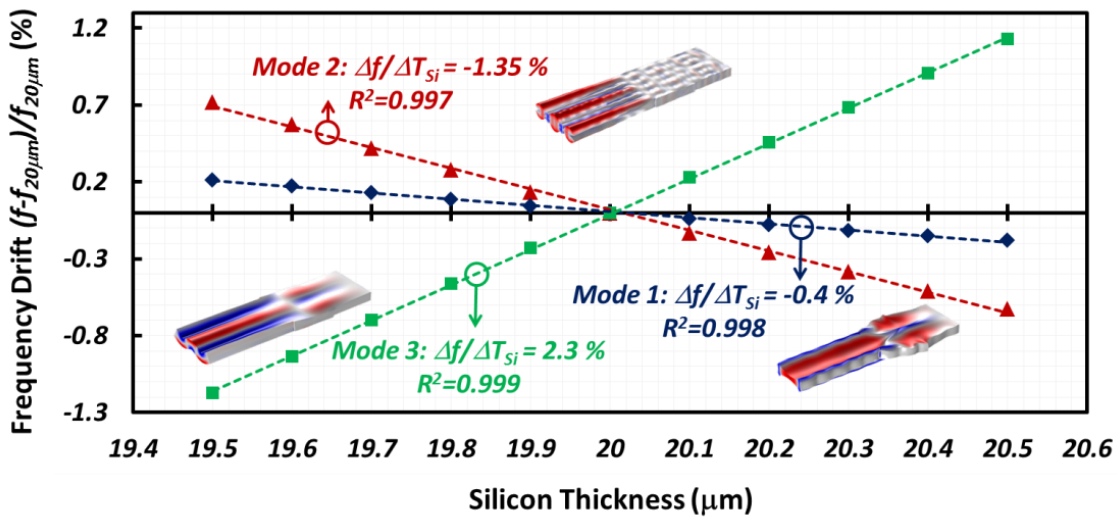

Figure 4.30: Simulated frequency drifts of the resonance modes 1, 2 and 3 over a thickness variation of ±0.5μm around silicon thickness (20μm) showing different trends for two out-of-plane modes (2 and 3). This offers feasibility of process variation compensation for the beat frequency by generating the f_b from a linear combination of the three modes (instead of two modes). This can be realized thanks to integer frequency ratios between all modes: $f_2 = 2f_1 = 4f_3$.

Figure 4.31 compares the thickness dependency of the TCF_b for beat frequencies t generated from different linear combinations of f_1, f_2 and f_3, in 1μm range around the nominal substrate thickness (20μm). Thickness dependency of the TCF_b is significantly reduced when the combination of the three resonance modes is used as beat frequency.

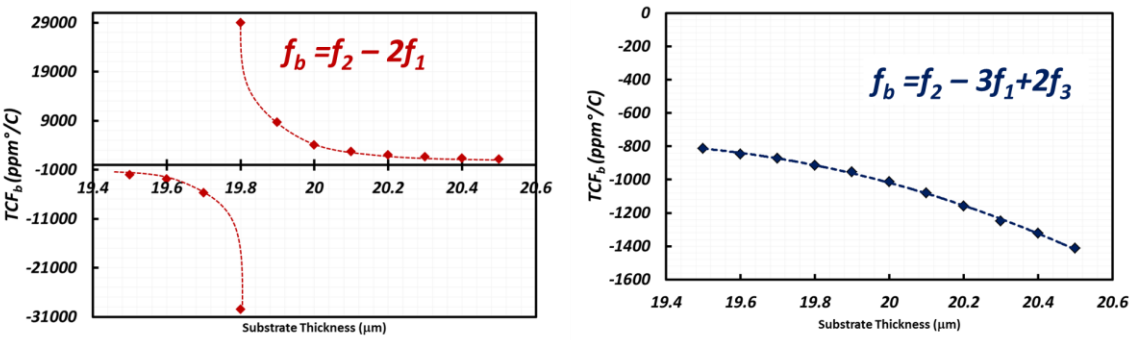

Figure 4.31: Substrate thickness dependency of TCF_b for beat frequencies generated from different linear combinations of $f_{1,2,3}$.

5 SILICON BULK ACOUSTIC RESONATORS WITH SIDEWALL ALN SIGNAL TRANSDUCTION

This chapter presents a piezoelectric transduction scheme which can be exploited for excitation/sensing in-plane resonance modes in thick silicon microstructures. In this novel piezoelectric transduction technique, aluminum nitride (AlN) thin films are integrated on the sidewalls of the silicon microstructure to provide normal stress, thus exciting in-plane resonance modes. High-frequency SiBARs have been implemented based on this technique using sputtered AlN that coats the sidewalls of a 20 um thick resonator conformally and with uniform thickness. The sidewall AlN layer enables efficient excitation of first width-extensional (WE_1) modes in the suspended silicon microstructure using the longitudinal piezoelectric effect. A motional resistance of ~35 Ω was measured in air for a 100 MHz SiBAR implemented using this technique, showing at least ten times smaller motional resistance compared to the capacitive counterpart. The low motional-resistance and high Q SiBARs with sidewall AlN can be used as building blocks for implementation of a versatile low-loss filter technology that can cover a wide frequency range (30 MHz to 3 GHz) in narrow channels and provide electronic bandwidth and frequency tunability. A one-stage ladder filter at ~100 MHz implemented using this technology shows an insertion loss (IL) of ~5 dB (with 50 Ω terminations) and a tunable bandwidth ranging between 110-360 kHz. An array of two adjacent channel-select filters with different bandwidths is also demonstrated.

5.1 INTRODUCTION

In the novel transduction mechanism explained in this chapter, instead of (only) using an aluminum nitride (AlN) layer on the top surface of the resonator for actuation

and sensing through the transverse piezoelectric effect (e_{31}), AlN layers on the sidewalls are (simultaneously) used to employ the larger longitudinal piezoelectric coefficient (e_{33}) for the transduction of bulk acoustic waves through the resonator sidewalls. This concept is schematically shown in figure 5.1.

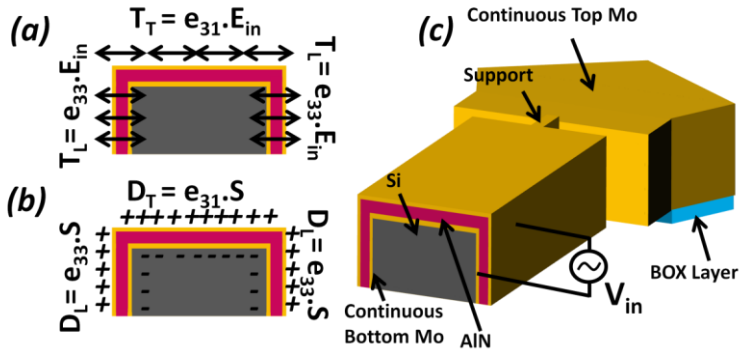

Figure 5.1: (a) The actuation mechanism and (b) the sense mechanism for a SiBAR with AlN layers on the top surface and sidewalls. (c) A cross section of the resonator and proper electrical termination for the application of electrical signal. E_{in} and D_L are the applied electric field and excited electric-displacement respectively.

Besides benefiting from larger piezoelectric longitudinal coefficient of the AlN thin-film, such a scheme enables excitation of in-plane resonance modes by providing normal stress on the sidewalls of the microstructure. Hence, sidewall AlN transduction mixes the benefits of lithographical frequency definition of MEMS, with highly efficient longitudinal piezoelectric transduction which was previously limited to thickness mode film bulk acoustic resonators (FBAR).

In sidewall AlN transduction mechanism, since the molybdenum (Mo) electrodes are connecting AlN surfaces with similar mechanical strain, the charge cancellation is substantially smaller compared to the transverse AlN transduction mechanism. Moreover, since the transduction occurs on two (or multiple) sidewalls instead of the top surface, it is scalable with the thickness of the resonator, alleviating the need for high order mode resonators to provide large transduction areas. Besides showing superior transduction

efficiency compared to the conventional micromechanical resonators, SiBARs with sidewall AlN layers offer substantially higher frequency definition versatility compared to film bulk acoustic resonators (FBAR). While in FBARs the resonance frequency of the device is mainly a function of the piezoelectric film thickness, the resonance frequency of SiBARs with sidewall AlN is defined by the lateral dimensions of the relatively thick silicon microstructure rather than piezoelectric thin film. This implies that the resonance frequency of such devices can be defined lithographically, simplifying the implementation of resonator arrays with different operating frequencies on a common substrate and in the same batch.

5.2 THEORY OF SIDEWALL ALN SIGNAL TRANSDUCTION

In sidewall AlN actuation mechanism (Figure 5.1a), the electrical voltage applied across the AlN layer creates a longitudinal stress (T_L) in that can be calculated from:

$$T_L = e_{33} \cdot \frac{V_{in}}{W_{AlN}}, \qquad (5.1)$$

where V_{in} is the applied voltage and W_{AlN} is the thickness of sidewall AlN layers. T_L excites a width-extensional strain in the SiBAR and AlN films which is amplified at the resonance frequency by the mechanical quality factor (Q) of the resonator. The amplified strain induces electrical charges on the Mo electrodes sandwiching AlN layers as a result of longitudinal piezoelectric effect (Figure 5.1). The induced charge (q) at the resonance frequency can be calculated from:

$$q = A_{SW} \cdot e_{33} \cdot \frac{\Delta W_{AlN}}{W_{AlN}} + \frac{\varepsilon^S \cdot A_{SW}}{W_{AlN}} \cdot V_{in} = A_{SW} \cdot e_{33} \cdot (S_1 - S_2) + \frac{\varepsilon^S \cdot A_{SW}}{W_{AlN}} \cdot V_{in}, \qquad (5.2)$$

where A_{SW} is the sidewall surface area, ΔW_{AlN} is the thickness change of the sidewall AlN film at resonance, ε^S is the strain-free dielectric permittivity of AlN, and S_1 and S_2

are the normalized particle displacements of sidewall AlN at the interface of top and bottom Mo electrodes. It can be implied from (5.2) that the amount of excited charge on the sidewall AlN layer is directly proportional to the resonator sidewall area and is scalable with resonator thickness. Figure 5.2 shows the first width-extensional resonance mode-shape of the SiBAR with sidewall AlN.

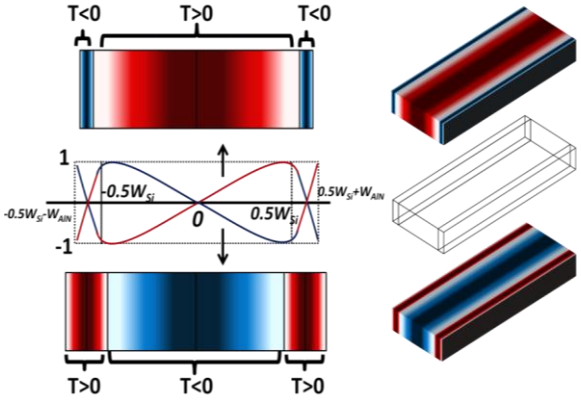

Figure 5.2: Stress field (T) and deformation in two half-cycles of the first width-extensional resonance for the SiBAR with sidewall AlN transduction.

To derive an electrical equivalent model for a SiBAR with AlN transduction layers on its top surface and sidewalls, each AlN layer should be considered as a separate electromechanical transducer. Therefore, a SiBAR with top surface and sidewall AlN layers can be modeled as a three-port device (Figure 5.3).

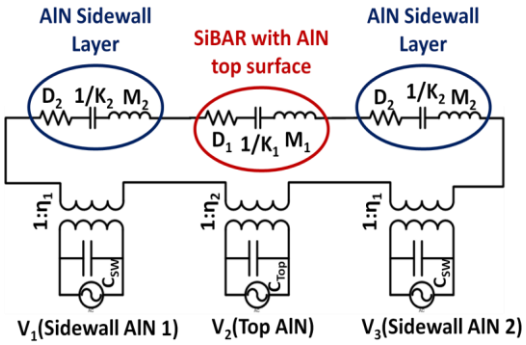

Figure 5.3: Electrical equivalent circuit for a SiBAR with AlN transducers on its sidewalls and top surface. The device can be considered as a one-port resonator if the top Mo layer is continuous over the sidewall and top surfaces of the device. In that case $V_1=V_2=V_3$.

In this model, the transformers represent the two piezoelectric transduction mechanisms with the longitudinal (η_1) and transverse (η_2) coupling coefficients. This model can also be considered as three mechanical resonators (two AlN thickness-extensional resonators on the sidewalls and the SiBAR with AlN on its top surface) that are acoustically coupled in series..

In the equivalent circuit of the figure 5.3, D_i, K_i and M_i are equivalent damping, stiffness and mass of the SiBAR with top AlN (i=1) and sidewall AlN layers (i=2) respectively. C_{SW} and C_{Top} are the capacitances of the sidewall and top AlN layers, respectively. The longitudinal coupling coefficient ($\eta_{1)}$ can be calculated from:

$$\eta_1 = \frac{F_{Si/AlN}}{V_{in}} = \frac{T_{Si/AlN} \cdot A_{SW}}{V_{in}} = e_{33} \frac{A_{SW}}{W_{AlN}} [\varphi(x)]_{(W_{si}/2)}^{(W_{si}/2+W_{AlN})}, \qquad (5.3)$$

where $F_{Si/AlN}$ is the force exerted by the sidewall AlN layer at the Si-AlN interface, A_{SW} is the sidewall surface area and $\varphi(x)$ is the mode shape at resonance. Considering the mode shape shown in Figure 5.2, η_1 becomes:

$$\eta_1 = 2e_{33} \frac{A_{SW}}{W_{AlN}} = 2e_{33} \frac{L_{res}}{W_{AlN}} \cdot T_{res}, \qquad (5.4)$$

where L_{res} is the length of the resonator.

The transverse coupling coefficient (η_2) can be calculated from:

$$\eta_2 = \frac{F_{Top}}{V_{in}} = e_{31} L_{res} [\varphi(x)]_{-W_{si}/2}^{W_{si}/2}, \qquad (5.5)$$

where F_{Top} is the force applied by the top AlN layer to the resonator and T_{res} is the thickness of the resonator. For the first width-extensional resonance mode η_2 can be simplified as:

$$\eta_2 = 2e_{31}L_{res} = 2e_{31}\frac{A_{SW}}{T_{res}}, \qquad (5.6)$$

In the special case of figure 5.1c where the conformal Mo layers are electrically shorting all three ports of the equivalent circuit of figure 5.3, the resonator becomes a one-port device and hence, its motional resistance (R_m) can be estimated from:

$$R_m = \frac{D_{tot}}{(2\eta_1 + \eta_2)^2}, \qquad (5.7)$$

where D_{tot} represents the total mechanical damping factor of the resonator. Since $|e_{33}| \approx 3|e_{31}|$ and T_{res} is much larger than W_{AlN}, η_1 is much larger than η_2 (in this work $\eta_1 \approx 100\eta_2$), implying that actuation and sensing of the bulk acoustic resonance is much more efficient using piezoelectric films on the sidewalls rather than the top surface. Thus, bulk acoustic resonators with sidewall piezoelectric transduction should provide a considerably lower R_m than those employing top surface AlN actuation and sensing. Additionally, since η_1 is directly proportional to T_{res}, R_m can be further reduced by increasing T_{res}. This is a superior advantage of sidewall compared to top surface transduction, where a piezoelectric layer with large surface area is required to achieve small values of R_m.

5.3 FABRICATION PROCESS FOR SIBARS WITH SIDEWALL ALN

The fabrication process of one-port SiBARs with top and sidewall AlN requires only two masks (figure 5.4).

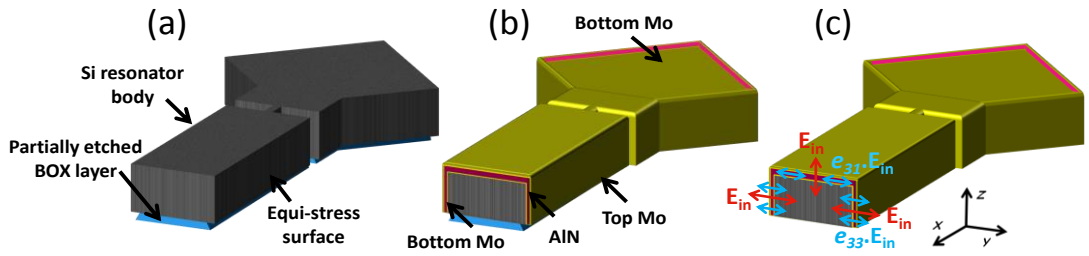

Figure 5.4: Resonator fabrication process: (a) Patterning Si device layer and partially etching the BOX layer; (b) Deposition of Mo/AlN/Mo layers, etching top Mo and AlN on one pad to expose

First, the resonator body is patterned in the silicon device layer of a thick SOI wafer (figure 5.4a) using Bosch-DRIE process. The special nature of Bosch-DRIE process results in sidewall scalloping and striation (Figure 5.5).

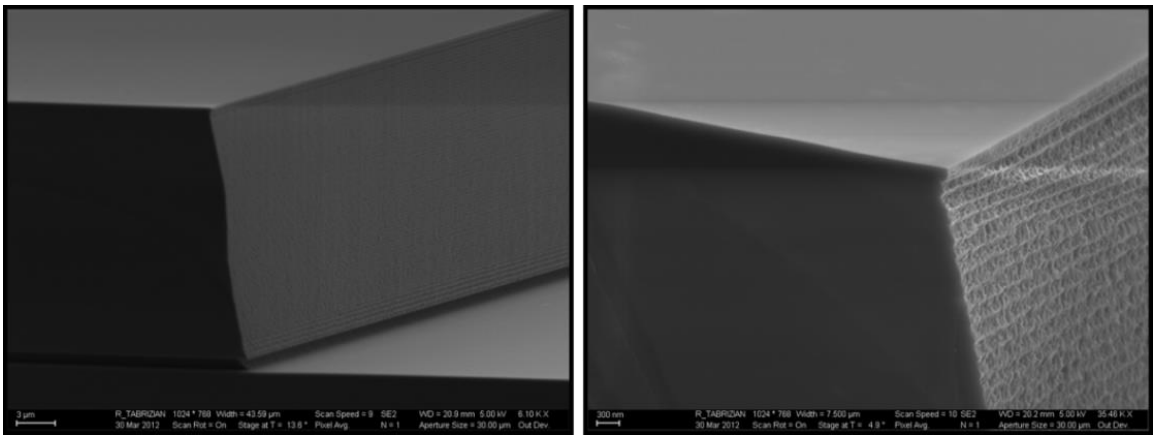

Figure 5.5: Sidewall surface roughness after Bosch-DRIE process. Scalloping and striation is clear in the zoomed-in figure (right).

This makes the sidewall surface rough, thus undesirable for AlN film deposition. Therefore surface smoothening treatments for the sidewall of patterned silicon platforms is of crucial importance. Figure 5.6 shows the low-quality AlN films with large grains deposited on rough silicon sidewall surface after Bosch-DRIE.

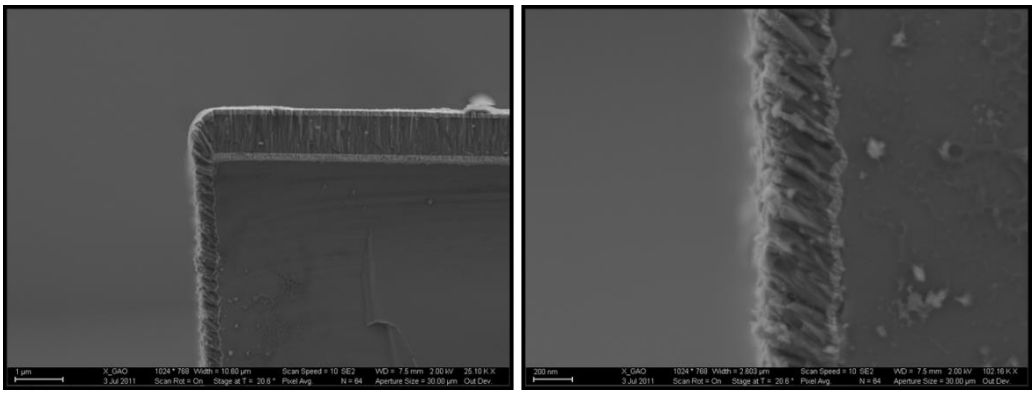

Figure 5.6: Low-quality of AlN film deposited on non-treated sidewall surface after Bosch-DRIE step.

For the purpose surface smoothening, several steps of dry-oxidation and oxide removal has been used, followed by annealing in H_2 at 1100°C to remove sidewall roughness and prepare the smooth surface required for high quality AlN deposition (Figure 5.7).

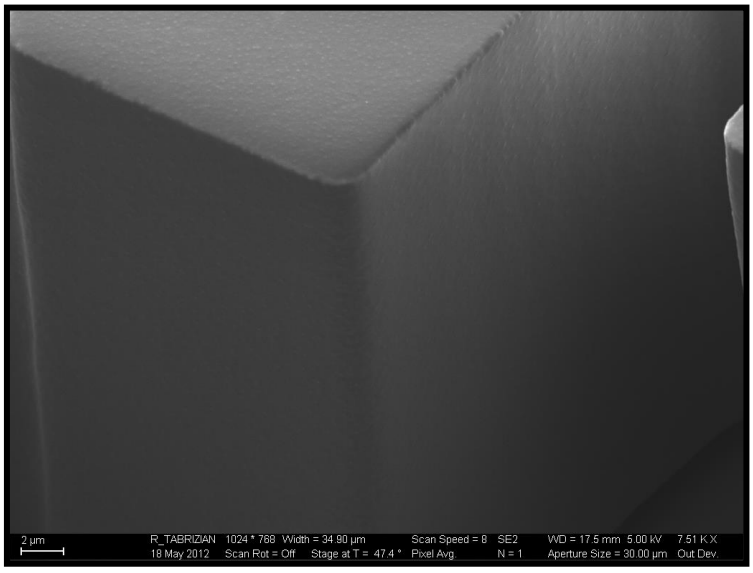

Figure 5.7: Smoothened surface of the silicon microstructure after dry oxidation/removal and H_2 annealing resulting on complete removal of surface scalloping and striation.

This is followed by RF sputter deposition of a thin AlN layer sandwiched between bottom and top Mo electrodes on the resonator top surface and sidewalls (Figure 5.8). High-quality AlN layers resulted from sputtering on smooth surface has been achieved

showing film continuity over sidewall and top surfaces.

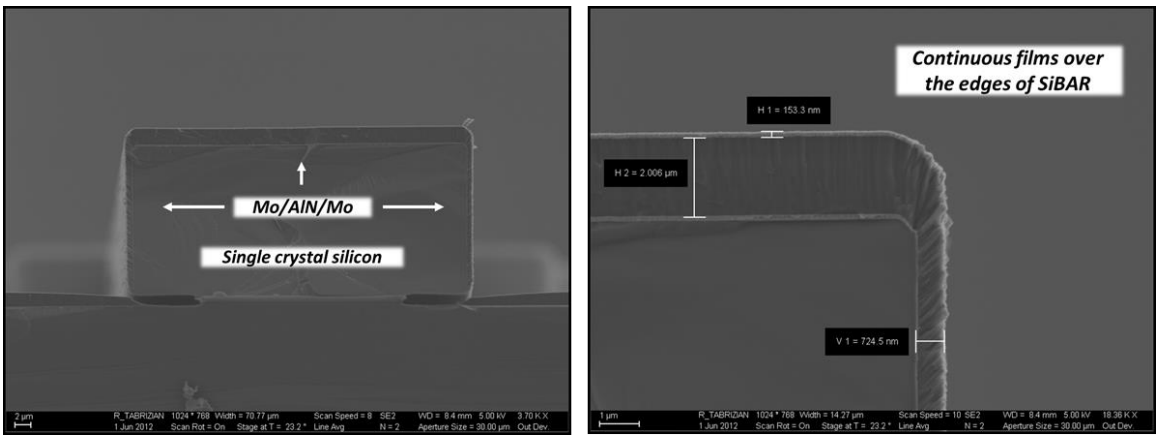

Figure 5.8: Conformal AlN layer covering sidewalls and top surface of the silicon resonator. Film continuity can be clearly observed at the corner of the structure.

Figure 5.9(a) shows the thickness uniformity of the sidewall AlN film across silicon structure thickness. The film termination at the bottom corner of the SiBAR can be observed in figure 5.9(b).

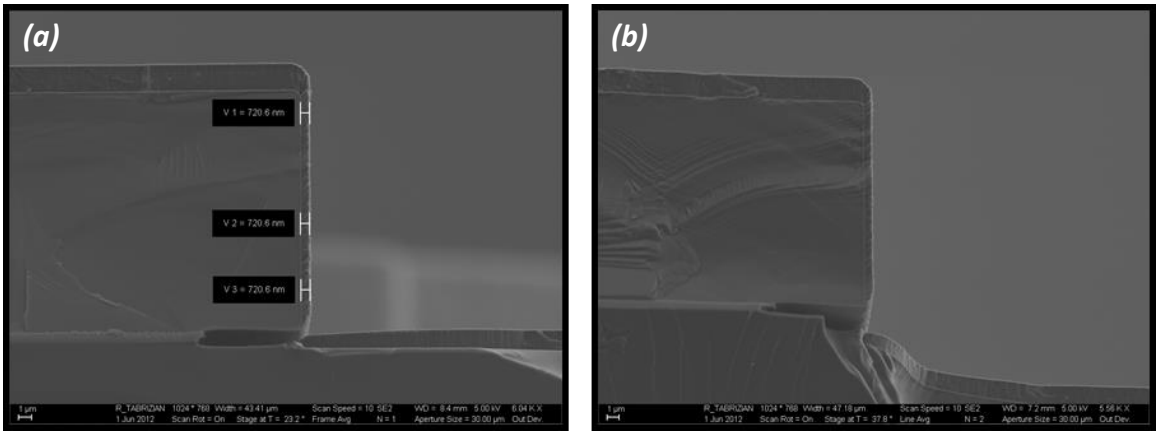

Figure 5.9: (a) Sidewall film thickness uniformity across the entire SiBAR thickness and (b) film termination at the bottom corner of the microstructure facilitating device release in BOE.

Then, the top Mo and AlN layers are etched from one pad to access the bottom Mo which serves as an electrical signal ground (figure 5.4b). Finally, the device is released by etching the BOX layer in HF (figure 5.4c). Figure 5.10 shows an SEM image of a fabricated one-port SiBAR with AlN on sidewalls and top surface and schematic of

the electrical interface for measurement. The bottom Mo serves as ground for sidewall and top AlN layers. An input signal is applied to the continuous top Mo.

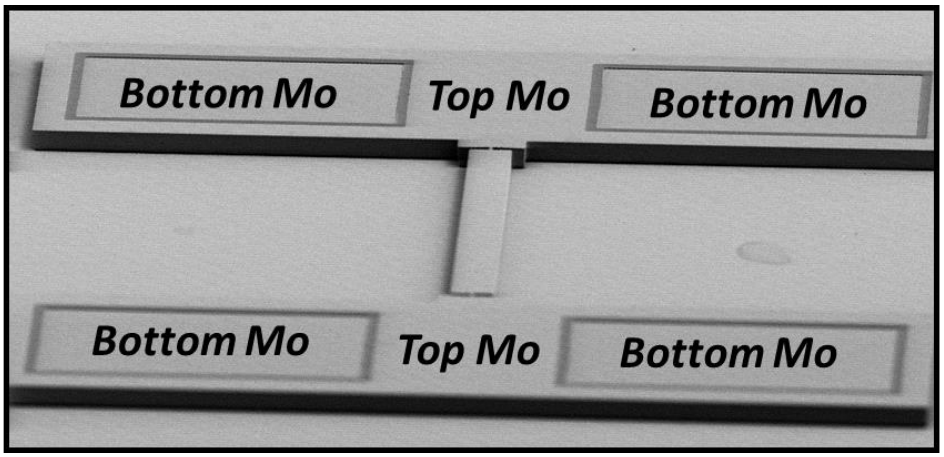

Figure 5.10: The SEM picture of the one-port SiBAR with Sidewall and top surface AlN signal transduction. The bottom Mo serves as the ground for the electrical signal applied to the top Mo.

Experimental results are obtained using a vector network analyzer. Figure 5.11 shows the measured reflection coefficient (S_{11}) of the one-port resonator. A motional resistance as small as 33 Ω has been measured for a ~100 MHz resonator with a Q of ~7,800 measured in air.

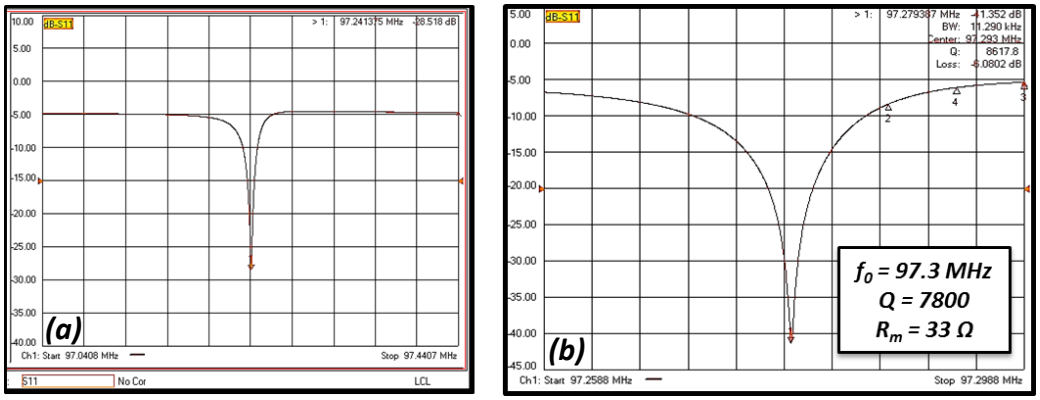

Figure 5.11: (a) Large-span and (b) short-span S_{11} response of the SiBAR with sidewall AlN signal transduction.

5.4 RECONFIGURABLE SIBAR FILTERS WITH SIDEWALL ALN TRANSDUCTION

A truly reconfigurable filter technology should offer center frequency, bandwidth, and order reconfiguration in a wide frequency range. This requires a low-impedance, high-Q resonator technology that can cover a useful spectrum via tuning and/or arraying (e.g., 30MHz to 3GHz) and can lend itself well to electrical coupling to create arbitrary filter responses. This has been difficult to achieve using acoustic resonators due to various issues related to physical size, impedance, Q factor and tuning. In our earlier work, we had reported on sidewall AlN transduction of high-Q silicon bulk acoustic resonators (SiBAR) with rectangular bar geometry. These are one-port width-extensional resonators with lithographically-defined frequencies. By engineering the dimensions, especially the thickness of the bar structures, lateral BAW resonators with very low motional resistances can be realized, enabled by the very efficient longitudinal piezoelectric coefficient (d_{33}) of an AlN layer covering the large sidewalls of the device. Furthermore, this transduction configuration results in inherently negligible charge cancellation at the transduction port, since the metallic electrodes sandwiching the AlN layer are extended over unistress surfaces with uniformly-excited charge distribution (figure 5.1a).

These resonators can essentially be interpreted as lateral FBARs sandwiching a layer of silicon with lithographically-defined dimensions. Following this interpretation, these devices not only inherit AlN FBAR advantages, but also surpass them in several aspects: since the resonance frequency of AlN-on-sidewall SiBARs is mainly defined by the lateral dimensions of their central silicon structure, band-pass filters with any

desirable frequency can be implemented on a common substrate, while a single deposition of a piezoelectric AlN layer suffices for providing efficient electromechanical transduction to all the resonators. Furthermore, since these resonators have two dimensions with frequency dependencies extended at the two extremes (i.e., small frequency dependency on the length as opposed to high frequency sensitivity to the width of the resonator), a large range of frequencies can be realized, comfortably extending from 30 MHz to 3 GHz to cover the entire VHF and UHF bands. Last, but not least, real-time bandwidth and frequency tuning can be realized by running small currents through the silicon body of individual resonators. In this paper, we use these resonators in ladder-type topology to implement reconfigurable narrowband filters with extremely sharp skirts and low pass-band insertion-loss.

A one-stage ladder-type filter consist of two AlN-on-sidewall SiBARs with high Q (~ 7,800 in air) and low motional resistance, one in series and one in parallel with offset frequency. Figure 5.12 schematically shows the filter construction as well as the principle of operation.

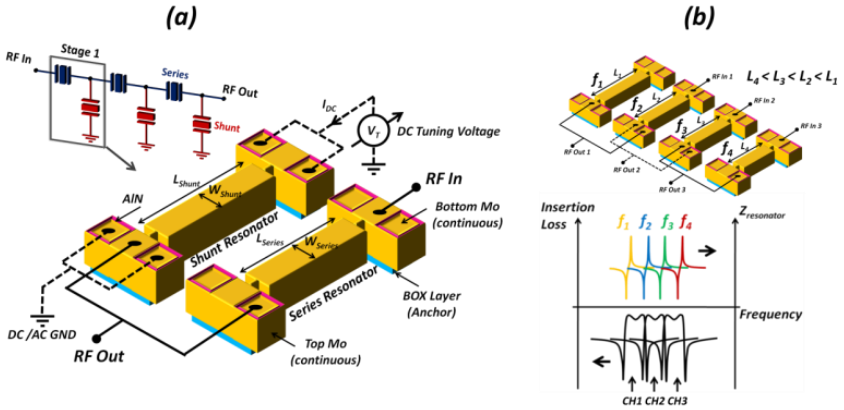

Figure 5.12: (a) Reconfigurable SiBAR filter with sidewall AlN transduction and thermal bandwidth and frequency tuning: one-stage ladder-type filter; (b) an array of adjacent channel-select ladder-type filters; each resonator serve as series and shunt element for two adjacent filters resulting in intrinsically-adjacent filter array.

The small frequency offset and hence filter bandwidth is achieved by modifying the length of the SiBARs. Larger offsets can be obtained by adjusting the width of the resonator (primary frequency determining dimension). Furthermore, having a large negative TCF of -32 ppm/°C (Figure 5.13), considerable frequency drift can be achieved by thermal tuning of each resonator of the filter, independently. This is done by passing a DC current via the body of the resonator resulting in the Joule heating. Large tuning ranges can be achieved using this technique by applying small DC voltages across the resonator.

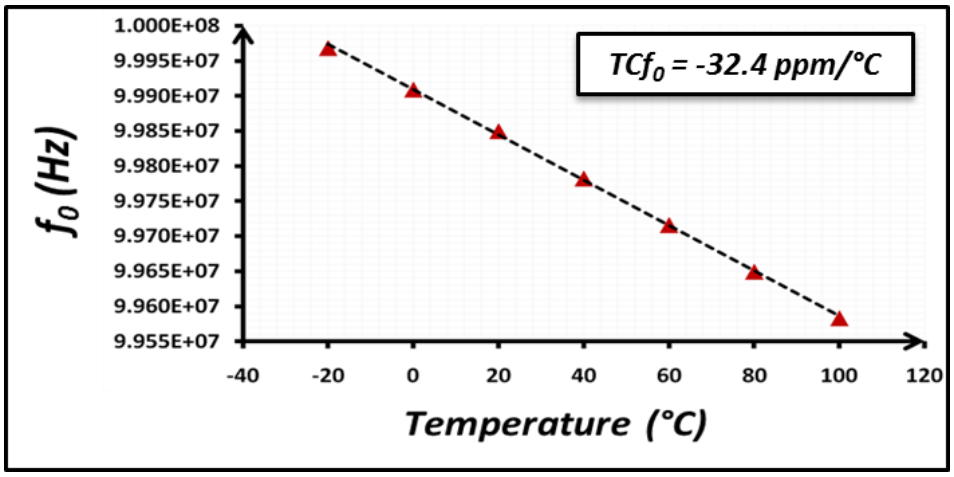

Figure 5.13: The temperature characteristic of the SiBAR with sidewall AlN signal transduction showing a large TCF of -32.4 ppm/C. This large temperature sensitivity has been used to provide device level tuning through self-ovenization of the silicon body through passing dc current and Joule heating.

Figure 5.14a shows the SEM picture of the fabricated AlN-on-sidewall SiBAR with electrical termination used for tuning. The AC ground ports of this resonator can be used to apply tuning voltage across the resonator (Figure 5.14b).

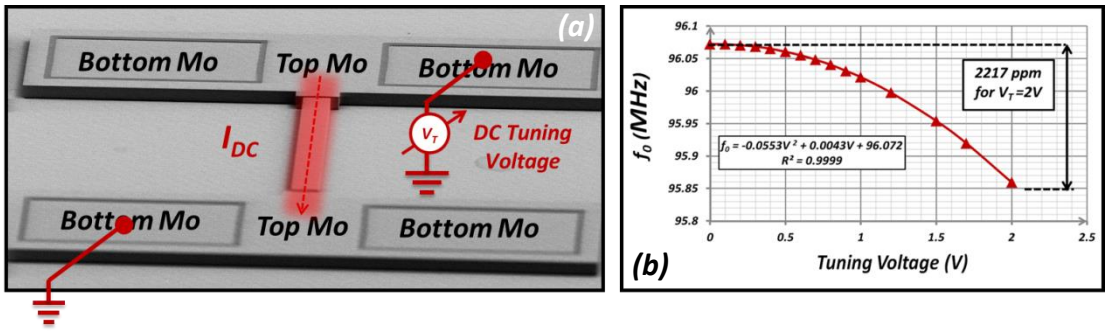

Figure 5.14: (a) The SEM picture of the device with required electrical termination for application of DC tuning current. (b) Tuning characteristic of the device, showing 2217 ppm of tuning with application of 2V. This is due to large TCF of the silicon resonator.

The bandwidth and frequency of a narrow ladder filter implemented using two devices with slight frequency mismatch can be dynamically reconfigured by applying tuning current to one or both constituent resonators. Figure 5.15 shows the measured frequency response of the filter implemented based on two resonators. A large bandwidth tuning of ~227% has been achieved by application of 2V to the shunt resonator of the ladder configuration.

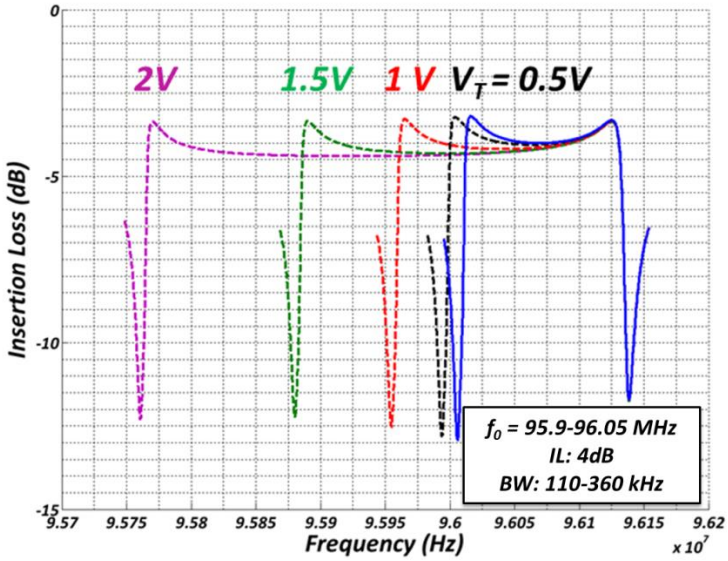

Figure 5.15: Measured frequency response of the ladder filter implemented from two SiBARs with sidewall AlN and with slight frequency mismatch. Bandwidth and frequency tuning has been achieved by application of ovenizing current to the shunt resonator of the ladder filter.

Figure 5.16 shows the simulated frequency response of two adjacent narrow-band filters implemented using three SiBARs with sidewall AlN resonators. The resonators are designed to have slight frequency mismatch. This frequency mismatch is defining the bandwidth of the ladder filter.

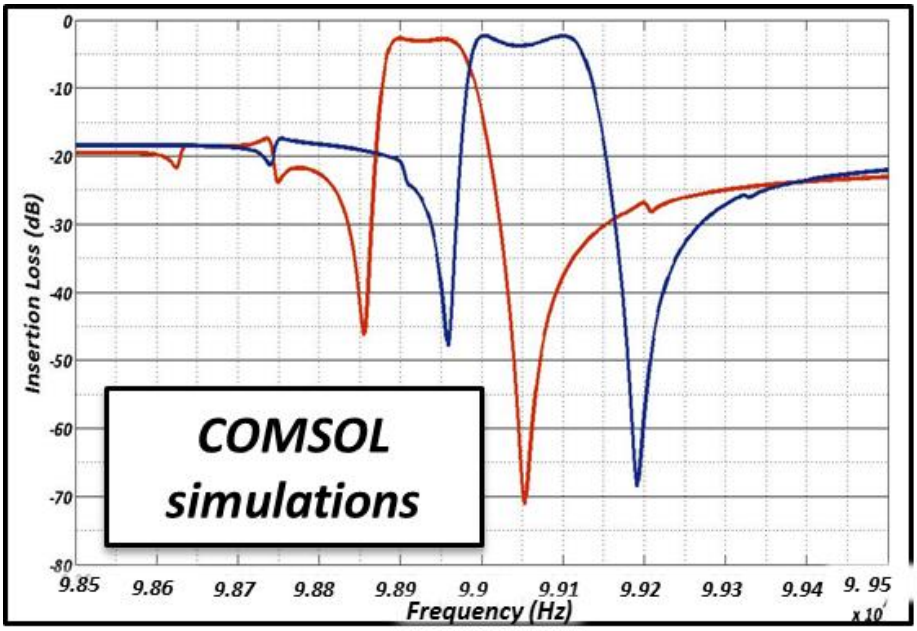

Figure 5.16: Simulated frequency response of two adjacent filters implemented from three resonators with slight frequency mismatch. A common resonator used for implementation of two filters results in substantial adjacency of the two filters.

Since the same resonator (with intermediate frequency among three) defines the pass-band transition of both filters, intrinsically adjacent band-pass channel-select filters can be implemented using this configuration.

Figure 5.17 shows the measure frequency response of the filters implemented based on simulations (Figure 5.16). The non-symmetric frequency response of the filters is a result of improper ratio of the transduction area which results in undesired ratio between shunt capacitors in each resonator. This can be solved by proper control and design of the length of SiBARs used for implementation of the filter.

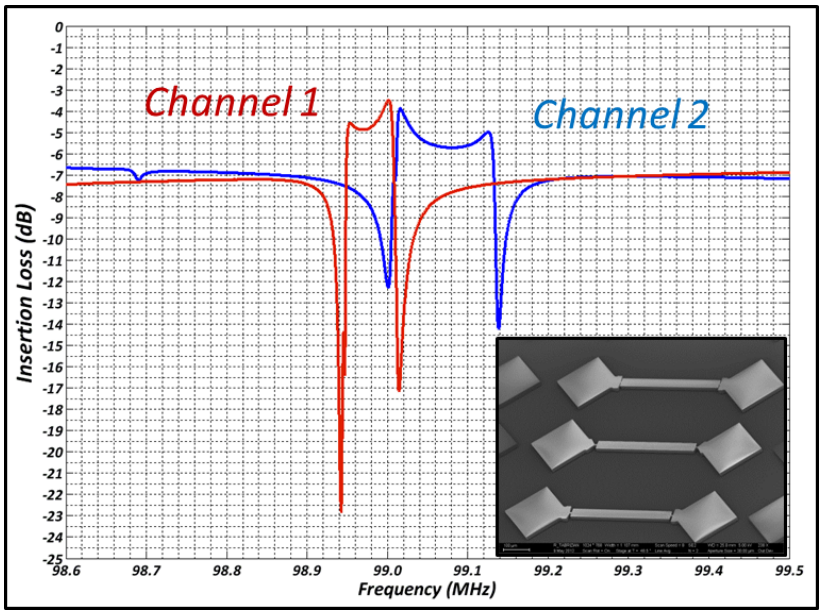

Figure 5.17: Measured frequency response of the adjacent filters implemented based on COMSOL simulations.

6 CONCLUSION AND FUTURE DIRECTION

In this dissertation novel acoustic platforms as well as electromechanical integrated transducer technologies have been introduced for implementation of high performance silicon-based MEMS resonators for frequency reference, signal processing and sensing applications. These technologies have been used to realize temperature insensitive resonators for highly-stable MEMS oscillators, multi-port acoustically-engineered resonators for accurate temperature sensing and low motional resistance resonators for narrowband versatile filtering. Our contribution in this thesis can be summarized as follows:

6.1 TEMPERATURE-COMPENSATED SILOX ACOUSTIC PLATFORMS

In this work, opposite trends of elastic coefficient temperature dependency in silicon and silicon dioxide has been used to implement composite homogenous SilOx platforms with temperature-compensated elastic moduli. These platforms have been implemented by embedding a uniformly distributed matrix of SiO_2 pillars inside the thick silicon body of the resonator. Simultaneous temperature compensation of independent elastic coefficients facilitates temperature desensitization of linearly independent shear and extensional modes in a single structure. Besides forty times improvement in temperature-induced drift in resonance frequency, resonators implemented in SilOx platforms shows an improvement in temperature stability of their quality factor (Q). These resonators are well suited for implementation temperature compensated and/or oven controlled MEMS oscillators.

6.2 ACOUSTICALLY-ENGINEERED SILICON RESONATORS

In this work, a new formulation of different resonance modes in MEMS resonators has been presented based on interpretation of micro-structure as an acoustic waveguide with finite dimensions. Such formulation provides design of novel resonators operating in synthetic modes with reduced temperature coefficient of frequency (TCF), spurious suppression and energy localization far from substrate. Low TCF shear lamb waves have been excited for the first time in silicon using think piezoelectric film transducers through acoustic coupling of waveguides supporting different

6.3 SIDEWALL ALN SIGNAL TRANSDUCTION

In this section, a new piezoelectric transduction scheme is presented which facilitates for the first time, using high efficiency longitudinal piezoelectric effect to excite in-plane modes. This realizes a powerful MEMS resonator platform which has both of the most important enabling processing features of micromachining which are Bosch-DRIE process and piezoelectric thin-films. Using this technique, low motional resistance resonators with frequencies spread over HF and UHF regimes can be implemented in a single batch. These devices are electrically coupled together to form narrowband filters with tunable frequency and bandwidth and low insertion loss.

6.4 FUTURE DIRECTION

All different sections of this dissertation can be considered as initial step in development of a universal MEMS platform for implementation of ultra-high-performance resonators. The robust theoretical formulation of dispersion and temperature characteristic of silicon-based acoustic platforms provided in chapters 3 and 4 can provide powerful design tools/approaches for realization of high-performance resonators

with flexible/programmable characteristics. These devices can be considered as building blocks of complex acoustic/electric systems, thus playing a similar role that CMOS transistors played in integrated circuits/systems. The future work in the direction of this dissertation includes design and implementation of resonators with frequencies in GHz range for signal processing applications. This can be challenging due to destructive distortion of the in-plane extensional resonance modes as width and thickness of the micro-structure becomes comparable, thus resulting in coupling of in-plane and out-of-plane propagating Lamb waves. Another aspect of future work can focus on implementation and integration of MEMS switches in the same platform, thus realizing dynamic coupling of different resonators to form filters with desired bandwidth and frequency. This facilitates implementation of a truly reconfigurable channel-select filter array over an extended frequency spectrum which can ultimately serve as the hardware for a software programmable radio.

REFERENCES

[1] R. T. Howe, "Resonant Microsensors," ed, 1987, pp. 2-5.

[2] K. W. Lakin, J, "Acoustic bulk wave composite resonators," *Applied Physics Letters,* vol. 38, pp. 125-127, 1981.

[3] M. A. Dubois, "Thin film bulk acoustic wave resonators: a technology review," *MEMSWAVE,* vol. 3, pp. 2-4, 2003.

[4] F. Ayazi, "MEMS for integrated timing and spectral processing," in *Custom Integrated Circuits Conference*, 2009, pp. 65-72.

[5] A. K. Samarao, G. Casinovi, and F. Ayazi, "Passive TCF Compensation in High Q Silicon Micromechanical Resonators," in *IEEE International Conference on Micro Electro Mechanical Systems (MEMS)*, 2010, pp. 116-119.

[6] W. Pan and F. Ayazi, "Thin-film piezoelectric-on-substrate resonators with Q enhancement and TCF reduction," in *Proc. IEEE MEMS*, 2010, pp. 727-730.

[7] A. K. Samarao and F. Ayazi, "Temperature Compensation of Silicon Resonators via Degenerate Doping," *Electron Devices, IEEE Transactions on,* vol. 59, pp. 87-93, 2012.

[8] A. Hajjam, A. Rahafrooz, and S. Pourkamali, "Sub-100 ppm/C temperature stability in thermally actuated high frequency silicon resonators via degenerate phosphorous doping and bias current optimization," in *IEDM*, 2010, pp. 170-173.

[9] M. Shahmohammadi, B. P. Harrington, J. Gonzales, and R. Abdolvand, "Temperature-compensated extensional-mode MEMS resonators on highly N-type doped silicon substrates," in *Hilton Head*, 2012, pp. 371-374.

[10] A. K. Samarao and F. Ayazi, "Temperature Compensation of Silicon Micromechanical Resonators via Degenerate Doping," in *IEEE International Electron Devices Meeting*, 2009, pp. 789-792.

[11] A. K. Samarao and F. Ayazi, "Intrinsic temperature compensation of highly resistive high-Q silicon microresonatros via charge depletion," in *International frequency control symposium*, 2010, pp. 334-339.

[12] R. Melamud, S. A. Chandorkar, B. Kim, H. K. Lee, J. Salvia, G. Bahl, M. Hopcroft, and T. Kenny, "Temperautre insensitive composite micromechanical resonators," *Journal of Microelectromechanical Systems,* vol. 18, pp. 1409-1419, 2009.

[13] R. Abdolvand, G. K. Ho, J. Butler, and F. Ayazi, "ZnO-on-nanocrystalline-diamond lateral bulk acoustic resonators," in *IEEE MEMS*, 2007, pp. 795-798.

[14] D. Grogg, H. C. Tekin, N. D. Ciressan-Badila, D. Tsamados, M. Mazza, and A. M. Ionescu, "Bulk lateral MEM resonator on thin SOI with high Q-factor," *IEEE Journal of Microelectromechanical Systems*, pp. 466-479, 2009.

[15] Z. W. V. A. Takhar, A. Peczalski, M. Rais-Zadeh, "Piezoelectrically transduced temperature-compensated flexural-mode silicon resonators," *IEEE Journal of Microelectromechanical Systems*, vol. 22, pp. 815-823, 2013.

[16] S. Pourkamali, A. Hashimura, R. Abdolvand, G. K. Ho, A. Erbil, and F. Ayazi, "High-Q single crystal silicon HARPSS capacitive beam resonators with sub-micron transduction gaps," *IEEE Journal of Microelectromechanical Systems*, vol. 12, pp. 487-496, 2003.

[17] G. K. Ho, J. K. C. Perng, and F. Ayazi, "Micromechanical IBARs: Modeling and process compensation," *IEEE Journal of Microelectromechanical Systems*, vol. 19, pp. 516-525, 2010.

[18] K. Sundaresan, G. K. Ho, S. Pourkamali, and F. Ayazi, "Electronically temperature-compensated silicon bulk acoustic resonator reference oscillators," *IEEE Journal of Solid-State Circuits*, vol. 42, pp. 1425-1434, 2007.

[19] D. E. Serrano, R. Tabrizian, and F. Ayazi, "Electrostatically tunable piezoelectric-on-silicon micromechanical resonator for real time clock," *IEEE Trans. Ultrason. Ferroelect. Freq. Control*, vol. 59, pp. 358-365, 2012.

[20] A. Tazzoli, M. Rinaldi, and G. Piazza, "Ovenized high frequency oscillators based on aluminum nitride contour mode resonators," in *IEDM*, 2011, pp. 481-484.

[21] K. Sundaresan, G. K. Ho, S. Pourkamali, and F. Ayazi, "A low noise 100MHz silicon BAW reference oscillator," in *Custom integrated circuits conferenece*, 2006, pp. 841-844.

[22] R. Tabrizian and F. Ayazi, "Reconfigurable SiBAR filters with sidewall AlN signal transduction," in *Hilton Head*, 2012, pp. 98-99.

[23] M. Shahmohammadi, D. Dikbas, B. P. Harrington, and R. Abdolvand, "Passive tuning in lateral-mode thin-film piezoelectric oscillators," in *IFCS*, 2011, pp. 1-5.

[24] R. Tabrizian and F. Ayazi, "Tunable silicon bulk acoustic resonators with multi-face AlN transduction," in *IFCS*, 2011, pp. 749-752.

[25] J. C. Salvia, R. Melamud, S. A. Chandorkar, S. F. Lord, and T. Kenny, "Real-time temperature compensation of MEMS oscillators using an integrated micro-oven and a phase lock loop," *IEEE Journal of Microelectromechanical Systems*, vol. 19, pp. 192-201, 2010.

[26] R. Tabrizian, M. Pardo, and F. Ayazi, "A 27 MHz temperature compensated MEMS oscillators with sub-ppm instability," in *IEEE MEMS*, 2012, pp. 23-26.

[27] H. M. Lavasani, W. Pan, B. P. Harrington, R. Abdolvand, and F. Ayazi, "Electronic temperature compensation of lateral bulk acoustic resonator reference oscillators using enhanced series tuning technique," *IEEE Journal of Solid-State Circuits*, vol. 47, pp. 1381-1393, 2012.

[28] F. Ayazi and K. Najafi, "High Aspect-Ratio Combined Poly and Single-Crystal Silicon (HARPSS) MEMS Technology," *IEEE Journal of Microelectromechanical Systems,* vol. 10, pp. 169-179, 2000.

[29] M. S. R. Ruby, F. Bi, D. Lee, L. Callaghan, R. Parker, S. Ortiz "Positioning FBAR technology in the frequency and timing domain," *IEEE Transactions on Ultrasonics, Ferroelectrics and Frequency Control,* vol. 59, pp. 334-345, 2012.

[30] K. M. Lakin, "Thin film resonators and filters," in *IEEE Ultrasonics Symposium*, 1999, pp. 895-906.

[31] R. Tabrizian, M. Rais-Zadeh, and F. Ayazi, "Effect of phonon interactions on limitting the fQ product of micromechanical resonators," in *IEEE Internation conference on solid-state sensors, actuators and microsystems (Transducers)*, 2009, pp. 2131-2134.

[32] F. Ayazi, R. Tabrizian, and L. Sorenson, "Compensation, tuning and trimming of MEMS resonators," in *International Frequency Control Symposium*, 2012, pp. 1-7.

[33] A. Ballato and J. R. Vig, "Static and dynamic frequency-temperature behavior of singly and doubly rotated, oven-controlled quartz resonators," in *IFCS*, 1978, pp. 180-188.

[34] G. Bahl and T. Kenny, "Observation of fixed and mobile charge in composite MEMS resonators," in *Hilton Head*, 2008, pp. 102-105.

[35] C. Bourgeois, E. Steinsland, N. Blanc, and N. F. de Rooij, "Design of resonators for the determination of the temperature coefficients of elastic constants of monocrystalline silicon," in *Frequency Control Symposium, 1997., Proceedings of the 1997 IEEE International*, 1997, pp. 791-799.

[36] J. R. Vig and T. R. Meeker, "The aging of bulk acoustic wave resonators, filters and oscillators," in *Frequency Control Symposium*, 1991.

[37] J. A. Kusters and J. R. Vig, "Hysteresis in quartz resonators-- A review," *IEEE Trans. Ultrason. Ferroelect. Freq. Control,* vol. 38, pp. 281-290, 1991.

[38] H. M. a. P. A. Jr., "Measurement of third-order moduli of silicon and germanium," *Journal of Applied Physics,* vol. 35, pp. 3312-3319, 1964.

[39] E. Bogardus, "Third-order elastic constants of Ge, MgO, and fused SiO2," *Applied Physics Letters,* vol. 36, pp. 2504-2513, 1965.

[40] J. F. Rosenbaum, *Bulk acoustic wave theory and devices* vol. 147: Boston: Artech House, 1988.

[41] R. Tabrizian, M. Hojjat Shamami, and F. Ayazi, "High-Frequency AlN-on-Silicon Resonant Square Gyroscopes," *IEEE Journal of Microelectromechanical Systems,* 2013.

[42] G. G. M. Fattinger, S. ; Kaitila, J. ; Aigner, R, "Optimization of Acoustic Dispersion for High Performance Thin Film BAW Resonators," presented at the IEEE Ultrasonic Symposium, 2005.